Graz University of Technology

Investigation of Simple Polymeric Systems by Computer Methods

Stefan Kontur

Dissertation submitted to the

Faculty of Technical Chemistry, Chemical and Process Engineering, Biotechnology

Graz University of Technology

In partial fulfillment of the requirements
for the degree of

Doctor technicae

October 2011

Abstract

Two aspects of polymer chemistry have been studied by means of computational methods. Structure and properties of micelles formed of symmetric A–B block copolymers in a selective solvent have been obtained from static Monte Carlo simulations on a simple cubic lattice employing the Pruned–Enriched Rosenbluth Method (PERM). This approach allowed to successfully sample micelles of up to 26 chains with a maximum total length of 100 effective monomers. A few simpler systems—semi-dilute solutions and polymer brushes on planar and curved surfaces—were also studied in a similar manner and allowed to validate the method. The results for micelles compare generally well to the Daoud–Cotton model and experimental data, while the expected dependence of association numbers on chain lengths could not be found.

Ground state properties and neutral electronic excitations of a group of photoinitiators—benzophenone, 1,5-diphenylpenta-1,4-diyn-3-one (DPD) and its bis(4-methoxy-), bis(4-thiomethyl-) and bis(4-(dimethylamino)) derivatives were studied by TDDFT using LDA, GGA and hybrid functionals. Additionally GW-quasiparticle states have been computed and the Bethe–Salpeter equation (BSE) was solved for the first two compounds. The results are in good qualitative agreement with experimental data. The nature of transitions of the important absorbance bands could be determined and processes that lead to photoinitiator activity clarfied. Exact exchange admixture to functionals appears to be necessary to describe the $\pi \rightarrow \pi^*$ transitions, while the hybrid functional B3LYP seems to introduce spurious shifts in the $n_O \rightarrow \pi^*$ excitation energies. Although GW yields very accurate ionization potentials, the solution of BSE ontop of GW did not improve much on TDLDA, while being computationally expensive. Nevertheless it is seen as a promising method.

Zusammenfassung

Zwei Aspekte der Polymerchemie wurden durch Computermethoden untersucht. Struktur und Eigenschaften von symmetrischen A–B Blockcopolymer-Mizellen in selektiven Lösungsmitteln wurden aus Simulationen erhalten, die auf der Pruned-Enriched-Rosenbluth-Methode (PERM) basieren und ein einfach kubisches Gitter verwenden. Mittels dieser Methode konnten Mizellen aus bis zu 26 Ketten mit einer maximalen Länge von 100 Monomeren erfolgreich erfasst werden. Einige einfachere Systeme – Lösungen mittlerer Konzentration, Polymerbürsten auf flachen und gekrümmten Oberflächen – wurden in ähnlicher Weise untersucht und erlauben eine Validierung der Methode. Die Ergebnisse für Mizellen entsprechen grundsätzlich dem Daoud-Cotton-Modell und experimentellen Daten, wenn auch die erwartete Abhängigkeit der Assoziationszahlen von der Kettenlänge nicht gefunden werden konnte.

Eigenschaften des elektronischen Grundzustandes und neutrale Anregungen einer Gruppe von Photoinitiatoren – Benzophenon, 1,5-Diphenylpenta-1,4-diin-3-on und seine Bis(4-methoxy)-, Bis(4-thiomethyl)- und Bis(4-(dimethylamino))-Derivate – wurden mittels TDDFT untersucht, wobei LDA, GGA und Hybridfunktionale verwendet wurden. Zusätzlich wurden GW-Quasipartikelzustände berechnet und die Bethe-Salpeter-Gleichung (BSE) für die ersten beiden Verbindungen gelöst. Die Ergebnisse stimmen qualitativ gut mit experimentellen Daten zusammen. Die Herkunft wichtiger Absorptionsbanden konnte bestimmt und Prozesse, die eine Photoinitiatoraktivität bewirken, geklärt werden. Es scheint notwendig zu sein, Funktionale mit exaktem Austauschanteil zu verwenden, um die $\pi \rightarrow \pi^*$-Übergänge zu beschreiben, gleichzeitig scheint das B3LYP-Funktional die Anregungsenergien von $n_O \rightarrow \pi^*$-Übergängen fälschlich zu erhöhen. Wenn auch die GW-Methode sehr genaue Ionisierungspotentiale ergibt, brachte die Lösung der BSE auf Basis von GW keine große Verbesserung im Vergleich zu TDLDA, bei gleichzeitigem hohen Rechenaufwand. Nichtsdestotrotz scheint sie eine vielversprechende Methode zu sein.

Contents

Chapter 1

Introduction and Motivation

The chemistry and technology of macromolecular compounds has been investigated in many aspects in the past 80 years and plays a major role in pure and applied chemistry. Polymer chemistry is from a point of view, like chemistry in general, an interdisciplinary matter ranging from quantum physics to biological activities of highly complex compounds, and from fundamental research to industrial applications. The experimentalist who is nowadays able to synthetize macromolecules with highly determined properties designed for sophisticated applications, may frequently encounter situations where measured data or intended chemical reactions do not yield the expected behavior. Be it that a property of interest is not accessible by experimental methods, that it is obscured by a too large number of uncontrolled parameters of the experimental setup, or that data deviate from or completely contradict expectations. These cases may illustrate the necessity of theoretical and computational methods to go hand in hand with work on the laboratory bench in successfully exploring the fields of research.

In this work two different approaches are made to bridge between theory and experiment. In Chapter 2 Monte Carlo simulations on a variety of polymeric systems are presented. The main objective of this study is a deeper understanding of the formation of block copolymer micelles in a selective solvent. This is an active field of experimental work in the group. Due to elaborated polymerization techniques, namely Ring-Opening Metathesis Polymerization (ROMP) of a large class of substances, it has become possible to finetune block lengths and monomer properties. And this ability raised questions about how chemical and macromolecular parameters influence micellar structures and sizes. It should be stressed here that simulations are not a theoretical method as such. Rather they can be viewed as experiments on a computer using a simplfied model for the system of interest. Like experiments, simulations produce not the same result with every measurement, but a statistical distribution of values. The simplified model must of course possess all features which are necessary to describe the desired properties. But it allows also to break the complex experimental situation down to a few parameters and study how they affect the behavior of the system. In that way simulations stand between experiments and theory and

refer to both of them.

In Chapter 3 an approach of somewhat different spirit is followed. The objects of the study are organic photoinitiator compounds which are used for crossliniking and photocuring processes. Hence an actor in the polymerization reaction is studied rather than the product. This is done by applying theoretical methods to the molecules of interest and compute properties in the respective approximation. As the electronic structure is to be calculated, all applied methods are based on quantum mechanics. These methods offer the possibility to learn more about the details of electronic transitions, the orbitals involved and their effect on the whole molecule.

Some of the methods and models in use here may seem odd at a first glance to be applied to chemical problems. As outlined in detail later, the simulation model for polymer chains greatly simplifies the macromolecules. This simplification goes that far, that their chemical structure is omitted altogether! At the other hand, electronic structure methods that were used here treat the organic molecules as if they were a homogeneous electron gas, which is actually an approximation for a solid metal. But it will be seen in the results sections that nevertheless these methodological concepts proof to be valuable tools in exploring the properties of the respective chemical system and the simplifications are valid to a large extent. Be it because the properties of a polymer chain do indeed depend only on its length and the monomer interaction which can in good approximation be expressed as an effective local one, be it because the electron density in the organic molecules does indeed vary slowly enough that the methods are applicable, in particular with some additional modifications.

It is hoped by the author that this work may shed some light on the fundamentals of the two problems briefly sketched already and be a help to the experimentalist working on their practical realizations.

The work is organized as follows: Chapter 2 deals with the Monte Carlo simulations of polymeric systems, Chapter 3 is dedicated to the electronic structure and excitations of the photoinitiators. Every chapter starts with some background information on the methods and concepts in use. This methodological introduction is by no means thorough or complete, rather it is intended to name some important facts as a foundation and support for the interpretations of the results. It is hence not suitable as an introduction of the concepts to the novice. The interested reader finds references to text books and reviews she may follow. After the background sections, the results of the work are presented and shortly discussed—these sections are the main part of the work. The various systems studied in every chapter are presented successively in a number of subsections. Every chapter ends with a conclusio drawn from the whole of results, suggestions for further work and the bibliography. Chaper 2 additionally lists pseudocodes to explain in greater detail the implementation of the concepts.

Chapter 2

Monte Carlo Simulations of Simple Polymeric Systems

2.1 Background

2.1.1 A Model for Polymer Chains

General Remarks

This work deals with the statistics of long, flexible polymer chains. A vast variety of polymeric compounds falls into this group, a few examples are given in Figure 2.1.

There are several levels of abstraction applicable to modeling such systems. The principal lines to decide which description is best to use follow the questions one wishes to answer by the results of the simulations and computational efficiency. Several levels starting from an advanced physical theory and ending at very simple models can be roughly divided into three levels

- an *ab initio* description based on quantum theories, such as Density Functional Theory (DFT) or the Hartree-Fock approximation (HF) and beyond

- force fields, which describe atoms, bonds, bond angles and other features of a molecule classically as point masses connected by springs with according potentials for the relevant internal coordinates

- coarse grained models, that are further abstracted from the chemical structure

This last point deserves some more detailed attendance as such an abstract model is used in this work. Apart from *ab initio* descriptions of, say a molecule as a quantum mechanical object, all models rely on a classical treatment of the system and disregard all quantum effects. This constitutes already a quite severe simplification but still produces reasonable results for equilibrium geometries and is suitable for systems containing a large number of atoms. From this point one can go further and group atoms that build a more or less rigid structure and subsume all forces into effective interactions. The case of a polymer chain allows one to coarse grain all parts of one or several chemical monomers together and
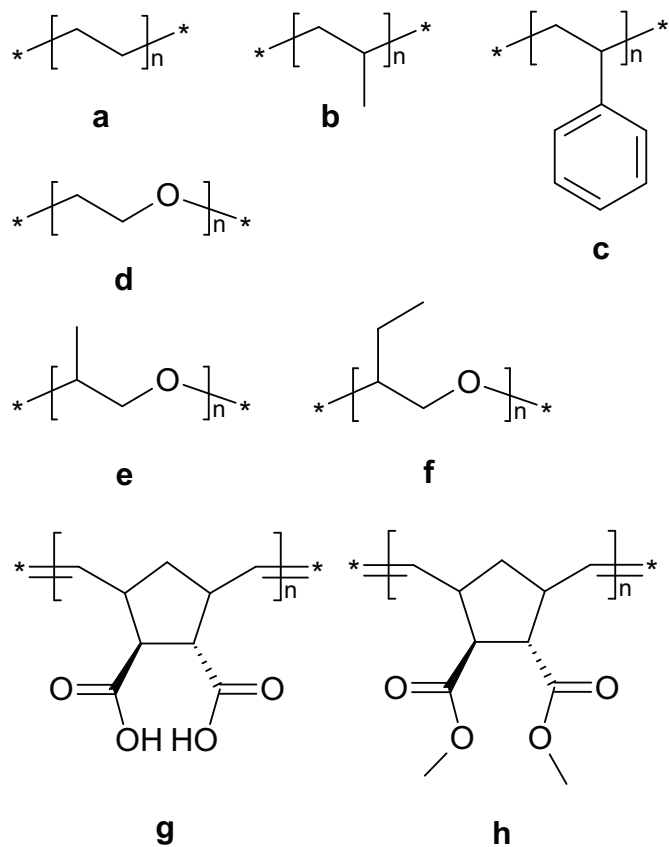
Figure 2.1: A few examples for flexible polymer chains: the common compounds polyethylene (a), polypropylene (b) and polystyrene (c), building blocks for pluronics polyoxyethylene (d), polyoxypropylene (e) and polyoxybutylene (f), building blocks for copolymer micelles studied in the group at ICTM *endo,exo*[2.2.1]bicyclo-2-ene-5,6-dicarboxylic acid (g) and its dimethylester (h).

substitute it by a single structureless *theoretical* monomer exhibiting an effective interaction ϵ [1, 2].

Another point of view starts from the properties of a polymer chain and strives to track it back to solely the chain length and interaction parameters of the theoretical monomers. The aim of this approach is to simplify the system of interest as much as possible and to generalize the observations to a wide range of compounds. In the limit of very long chains their properties become independent of the local structure and all models yield the same results. More about *scaling theories* can be found below and in Section 2.2.

The correspondence between a particular chemical structure and the abstracted model is determined by interaction characteristics of the theoretical monomer which can be traced back to the properties of the functional groups building the chemical monomers and experimental bulk features such as densities or radii of folded chains in solution, see page 7.

The implementation of such a model bears the important consequence that not only interactions between monomers can be included in the features of the monomers, but also interactions with the solvent. The explicit description of the solvent environment becomes completely unnecessary in this case, as it is implicitly included in the interaction characteristics of the monomers. This simplification causes a great increase in computational efficiency, as a large number of degrees of freedom needed for a layer of solvent molecules around the solute is omitted. It becomes hence tractable to run a simulation of rather large solute objects in a dilute solution, what would be completely unreachable otherwise.

Another simplification that seems a bit artificial at a first glance but does reduce the computer work significantly, is the discretization of the monomer coordinates. All objects in the system are only allowed to occupy sites on a lattice and no position in between. Speaking in computer language, integer coordinates are used rather than real ones. The simplest case is the hypercubic lattice, i.e. the square lattice in two-dimensional space and the cubic lattice in three dimensions, although other possibilities are sometimes advantageous, e.g. the triangular or the face centered cubic lattice.

Characteristics of Polymer Chains on the Lattice

To sample the conformations of a polymer chain a Random Walk (RW) [5, 6] would constitute the simplest possible sampling scheme. Such a chain is constructed stepwise by adding monomers at one of the nearest-neighbor positions of the recent one. A site on the lattice may be visited several times during the growth. Let the number of walks connecting the origin $\mathbf{0}$ and a point $\mathbf{r}$ in N steps be $\mathcal{N}_N(\mathbf{r})$. The total number of walks of N steps (or polymer conformations of N monomers), i.e. the partition sum Z_N, is then

$$\sum_{\mathbf{r}} \mathcal{N}_N(\mathbf{r}) = Z_N = z^N = z^N N^{\gamma-1} \tag{2.1}$$

with z neighbors of each site of the lattice and the exponent $\gamma = 1$. γ is a *universal exponent* (like ν below) and depends for a give type of chain only on the dimensionality d.

The end-to-end vector $\mathbf{r}$ is the sum of all step vectors $\sum_{n=1}^{N} \mathbf{a}_n$ making up the walk. Each step vector has length a (which is 1 lattice unit throughout

this work) and z possible directions. As different step vectors have *independent* orientations, scalar products $\mathbf{a}_n \cdot \mathbf{a}_m$ average to 0 if $n \neq m$ and the mean square end-to-end distance[1] $\langle R_{ee}^2 \rangle = \langle \mathbf{r}^2 \rangle$ becomes

$$\langle \mathbf{r}^2 \rangle = \sum_{n,m} \langle \mathbf{a}_n \cdot \mathbf{a}_m \rangle = \sum_n \langle \mathbf{a}_n^2 \rangle = a^2 N = a^2 N^{2\nu} \tag{2.2}$$

with the *universal exponent* $\nu = 1/2$. ν lies generally in the interval $1/2 \leq \nu \leq 1$ [7], where $\nu = 1/2$ corresponds to a chain of independent links, as for the RW, and $\nu = 1$ to a rigid chain. ν, like γ, depends for a given chain type only on the dimensionality d.

The RW neglects the finite volume of a polymer chain (the excluded volume) and is hence not very useful to study polymers[2]. More useful, e.g. for the study of polymer melts, is a modification of the RW that disallows double backing steps. The exponents for this walk stay the same as for the original RW ($\gamma = 1, \nu = 1/2$), but prefactors occur and z has to be replaced by $z_{\mathrm{eff}} = z - 1$.

The constraint of non-overlapping monomers excludes all configurations which cross themselves. This is known as the Self-Avoiding Walk (SAW) [5, 6, 8], which can be constructed by choosing one of the $2d - 1$ positions (positive and negative direction in every dimension d, double backing on itself is excluded by definition) and deleting a chain when the position for the next monomer to be added is already occupied.

The number of chain configurations for N (athermal) monomers is now

$$\mathcal{N}_N = Z_N = \tilde{z}^N N^{\gamma - 1} \tag{2.3}$$

with $\tilde{z}$ being an effective coordination number, somewhat smaller than the lattice's coordination number z. γ is roughly estimated to be $7/6$ for $d = 3$. The exponent ν for the scaling of the end-to-end distance R_{ee} changes also for the SAW and is estimated to $\nu_3 = 3/5$ for $d = 3$ and no thermal interactions[3]. Note the swelling of the chain with respect to the RW, caused by the excluded volume.

Another important observable studied by theory, simulations and experiments such as Small Angle Sight Scattering (SAXS) is the radius of gyration R_g [7, 9, 10]. It is obtained for a chain of N monomers from

$$\langle R_g^2(N) \rangle = \frac{1}{N} \left\langle \sum_{k=1}^{N} (\mathbf{r}_k - \mathbf{r}_{\mathrm{cm}})^2 \right\rangle = \frac{1}{N^2} \left\langle \sum_{i=2}^{N} \sum_{j=1}^{i} (\mathbf{r}_i - \mathbf{r}_j)^2 \right\rangle \tag{2.4}$$

where $\mathbf{r}_k$ is the position vector of the kth monomer and $\mathbf{r}_{\mathrm{cm}}$ is the center-of-mass of the whole chain. The second expression was used in this work, because the two sums can be combined with the process of growing the chain. The radius of gyration scales also with the exponent ν

$$\langle R_g^2(N) \rangle = A_1 a^2 N^{2\nu} \tag{2.5}$$

---

[1]This quantity is also referred to as Flory's radius R_F.

[2]But the mean square end-to-end distance also corresponds to the path a particle moves driven by thermal diffusion. The diffusion time is then associated with the number of steps taken during a simulation time. In the limit of arbitrary short step lengths the RW converges to Brownian motion.

[3]Interestingly $\nu_4 = 1/2$, i.e. the SAW behaves like a RW, or *ideally*, in four dimensions.

with the amplitude A_1 depending on the model. The ratio of the end-to-end distance and the radius of gyration is for the SAW [7]

$$\lim_{N \to \infty} \frac{6 \langle R_g^2(N) \rangle}{\langle R_{\text{ee}}^2(N) \rangle} = \aleph \tag{2.6}$$

The universal constant $\aleph$ is in one dimension $\aleph_1 = 1/2$ and for $d = 3$ one estimates $\aleph_3$ to assume a value a bit smaller than 1 [7].

An alternative radius that can be computed from the walks is the hydrodynamic radius R_H [7], which is related to experiments such a Dynamic Light Scattering (DLS) [11]. It can be computed using

$$\left\langle \frac{1}{R_H} \right\rangle = \frac{1}{N^2} \left\langle \sum_{i=2}^{N} \sum_{j=1}^{i} \frac{1}{|\mathbf{r}_i - \mathbf{r}_j|} \right\rangle \tag{2.7}$$

Mapping onto other Models and Real Chains

Following Geroff et al. [1, 3] in the limit long chains ($N \to \infty$) and dilute solutions ($\phi \to 0$) chains are self-similar on length scales large compared to their microscopic ones (i.e. the monomer bond length or the lattice unit length a in the present case). The only relevant length scale for intramolecular distances is the radius of gyration measured in units of the microspcopic length scale. Chain lengths have to be mapped onto one another. In the limit of dilute solutions one puts for the radius of gyration from simulations on the simple cubic lattice

$$\langle R_g^2 \rangle_{\text{SC}} / \langle l^2 \rangle_{\text{SC}} = C_{\text{SC}} N^{2\nu} \tag{2.8}$$

with $l = a$ and N the chain length in effective model monomers, and e.g. for an experimental R_g would sets

$$\langle R_g^2 \rangle_{\text{exp}} / \langle l^2 \rangle_{\text{exp}} = C_{\text{exp}} \tilde{N}^{2\nu} \tag{2.9}$$

where l is the monomer bond length and $\tilde{N}$ the degree of polymerization of the real chain. Then a conversion factor α mapping the chain lengths onto one another by $N = \alpha \tilde{N}$ must be such, that the amplitudes in both cases become equal, $C_{\text{exp}} = C_{\text{SC}} \alpha^{2\nu}$.

Two examples: Polymer **1** being polystyrene in a good solvent (carbon disulfide), the R_g of a sample of $M_w = 114000$ g mol^{-1} was measured by Small Angle X-ray Scattering (SAXS) as 137 Å [32]. The degree of polymerization is then ≈ 1095 and the monomer bond length should be taken simply as two $C[sp^3]$–$C[sp^3]$ single bonds of roughly 1.54 Å. Polymer **2** being a ROMP polymerized $endo,exo$[2.2.1]bicyclo-2-ene-5,6-dicarboxylic acid in good solvent (ethanole), the R_g was measured by SAXS to be 8.1 nm for a degree of polymerization of about 200 [75]. The monomer bond length can be estimated by optimizing the geometry of a tetramer by means of the semiempirical quantum chemistry method PM3 to be roughly 5.3 Å. One gets then converting all lengths to Å and disregarding all statistical or experimental errors

	SAW (1)	**1**	SAW (2)	**2**
N or $\tilde{N}$	1095	1095	200	200
l	1	3.08	1	5.3
$\langle R_g \rangle$ or $\langle R_g^2 \rangle^{1/2}$	26.83	137	9.75	81
α		2.36		2.15

In other words 100 monomers in the sc lattice model correspond roughly to 42 monomer units in polystyrene or 47 monomer units in the lyophilic polymer of [75].

2.1.2 Methodological Concepts

The algorithm in use for the present simulations is the Pruned–Enriched Rosenbluth Method (PERM) [4]. It is based on the SAW, which is realized by growing a polymer chain stepwise by adding new monomers on a randomly chosen neighboring site to the chain head (excluding the last-but-one monomer position $\mathbf{x}_{N-1}$). Recall from the preceding section that the construction procedure has to be aborted when the chosen site is already occupied by another monomer, i.e. the chain tries to cross itself. Hence this approach deletes many chains (*attrition*) and it is difficult to get good statistics of long chain configurations. The number of surviving chains C_n after n steps is

$$C_n = C_0 e^{-\lambda n} \tag{2.10}$$

with λ being the attrition constant and C_0 a constant approximately equal to the initial number of samples.

To overcome this attrition problem an approach was developed by Rosenbluth and Rosenbluth [14][4]. Within this method positions that are already occupied are excluded from the choice for the next monomer. As in this case some configurations are chosen more often than in a true SAW, i.e. in cases where there are less than $2d - 1$ empty positions, weights have to be introduced to correct for this difference in counting. These Rosenbluth weights are

$$W_N \propto \prod_{n=1}^{N} w_n \tag{2.11}$$

with

$$w_n = \frac{k_n}{2d - 1} \tag{2.12}$$

for a chain consisting of N monomers and k_n empty positons to choose for the nth monomer. Observe that $W_1 = W_2 = 1$ and a d-dimensional hypercubic lattice is assumed. If these weights are multiplied by the maximum total number of configurations, which are allowed to cross themselves but not to double back (Random Walk), $2d(2d - 1)^{N-2}$ (for $N \geq 2$), the true number of possible configurations of N monomers is obtained. This number is nothing else than the partition sum Z_N, which is in turn related to the free energy F of the system

$$F_N = -k_B T \ln Z_N \tag{2.13}$$

The Rosenbluth weights of different configurations may vary largely. As a consequence the ensemble is dominated by a few configurations with relatively high weights and statistics are poor. To deal with this difficulty the method of enriching a sample was adapted by Grassberger [4]. Enrichment was originally meant to adjust the sample size of an SAW to counterbalance attrition [15] and

---

[4]First calculations of this kind were carried out in the 1950's on the "electronic high speed computer" MANIAC I at Los Alamos, USA.

amounts to copy a configuration (i.e. the sample of chains, not the actual chain on the lattice) if necessary. This can be implemented as depth-first algorithm, by building the chains recursively and copy the configuration at a point of the growth, completing the chain and returning to the clone point.

In this context enrichment along with deletion of configurations is used to adjust the Rosenbluth weights. If the weight of a configuration at step n exceeds some upper threshold $W_n^>$ then the configuration is doubled and its weight divided by 2. On the other hand, if its weight falls below some lower threshold $W_n^<$ it is deleted with probability $1/2$ and the weight of the surviving configurations is doubled. This procedure assures that the correct statistics are still obtained, with the difference that the dominance of a few configurations with a very large weight is avoided. Other choices for copying and adjusting the weights are possible and may be advantageous.

If thermal interactions between monomers are present, the favoring of a site due to the proximity of neighbors can be brought in by Boltzmann factors—while still choosing one out of the neighboring empty site completely random (a procedure which shall be called *"simple sampling"*). As these Boltzmann factors correspond directly to the number (population) of configurations preferring this site, they can be included in the Rosenbluth weights. Starting from Equation 2.12 and including the total number of configurations, they take then the following form

$$w_n = k_n e^{-E_i/k_B T} \tag{2.14}$$

with $E_i = \sum_{\delta_i} \epsilon_{\delta_i}$ being the sum of all thermal monomer interactions ϵ between next-neighbors δ_i and the new monomer at the chosen site i (see also Section 2.1.1). Alternatively, the Boltzmann factors can be included in the probability to choose a particular site, i.e. the site for the new monomer is *not* chosen uniformly amongst the empty sites, but according to the resulting thermal interaction. This method shall be referred to as *"importance sampling"* here. The probability to choose a site i at step n amongst k_n free sites becomes in this case

$$p_i = \frac{e^{-E_i/k_B T}}{\sum_{j=1}^{k_n} e^{-E_j/k_B T}} \tag{2.15}$$

Also combined choices for including the Boltzmann factors between the weights w_n and probabilities $p_i^{k_n}$ are possible. In any case

$$p_i^{k_n} w_n = e^{-E_i/k_B T} \tag{2.16}$$

has to be fulfilled. The $\propto$ sign in Equation 2.11 means that constants can be put in front of the right-hand side. In case these are just powers of N, i.e. $W_N = z^N \prod_{N=1}^n w_n$, the expectation value of $\sum_N W_N$ corresponds to the grand canonical partition sum Z_N.

An empty site represents the solvent environment, but no restriction is applied concerning the placement of a monomer onto it. Note that the athermal SAW corresponds to a polymer chain in good solvent, where the monomers "feel" an ideal solvent in their environment that screens all other monomers. Monomers with thermal interactions tend to aggregate in such a way to minimize the internal energy and "feel" a poor, thermal solvent around. Having a Boltzmann factor for next neighbors i and j, which are not immediate consecutive monomers of one chain, $q_{ij} = e^{\epsilon_{ij}/k_B T}$ where $\epsilon_{ij} = 1/k_B$ one finds that the

critical temperature for the θ collapse is estimated to be $T_\theta = 3.717 \pm 0.003$ for this model [4]. At the θ-point the thermal SAW constructed with the algorithm recovers the properties of the RW, while still posessing an excluded volume.

Earlier work employing PERM and its modifications include studies of homopolymer [4, 16, 17, 28] and heteropolymer chains [18, 19], star [20] and bottle brush polymers [21] and confined polymers [22]. The cited sources use mostly some lattice implementation, although there are also cases of off-lattice applications [4, 18].

2.1.3   Random Number Generators

A good portion of the quality of the code relies on the type of random generator in use to produce very many floating point numbers uniformly distributed between 0 and 1. It should combine a maximum of uniformity in the distribution, a minimum of correlations between subsequent results and a minimum of computer power to produce them.

Generators usually employ some linear congruential algorithm of the type

$$i_{j+1} = (ai_j + c) \bmod m \tag{2.17}$$

with a proper choice for a, c and m, which produce a sequence of integer numbers i_j starting from a *non-zero* start value (*seed*) and are divided by m to yield floating point numbers between 0 and 1. One weakness of this method is that if k of its random numbers are used at a time to plot points in a k-dimensional space, correlations occur in a sense that these points are *not* distributed uniformly but lie on $(k-1)$-dimensional planes. The number of planes is *at most $m^{1/k}$*. This may have severe consequences for a simulation as the phase space is not anymore sampled completely and uniformly. Another issue is the period of the random number sequence, at most of length m, which is chosen close to the system's maximum integer (e.g. $2^{31} - 1$ on a 32-bit machine). In this work a large number of calls is necessary, so periods of this range are to be avoided. A solution to this challenge (L'Ecuyer [23]) is the combination of two such linear congruential generators with different periods. Then the two sequences are usually subtracted and $m - 1$ of either of them is added, if the result is smaller than 0 (m being the modulus of either of the generators).

The implementation of a linear congruential generator follows Schrage [26, 27] and is based on an approximate factorization of m in the form of $m = aq + r$ with $q = \text{integer}(m/a)$ and $r = m \bmod a$. If $r < q$ and $0 < z < m - 1$ it can be shown that

$$az \bmod m = \begin{cases} a(z \bmod q) - r \cdot \text{integer}(z/q) & \text{if } \geq 0 \\ a(z \bmod q) - r \cdot \text{integer}(z/q) + m & \text{otherwise} \end{cases} \tag{2.18}$$

and that all terms are in the range $0, \ldots, m - 1$ and hence produce no over- or underflow.

Additonally a *shuffle* step [26] can be used to remove low-order serial correlations. The values i_j are then not output directly at the jth call, but stored in an array and output at some randomized later call.

The random number generator used in this work was the **ran2**-Routine from [26], which corresponds to the above (see also pseudocode in Section 2.4). Additionally a few runs were carried out employing Ranlux (in the levels 3 and 4)
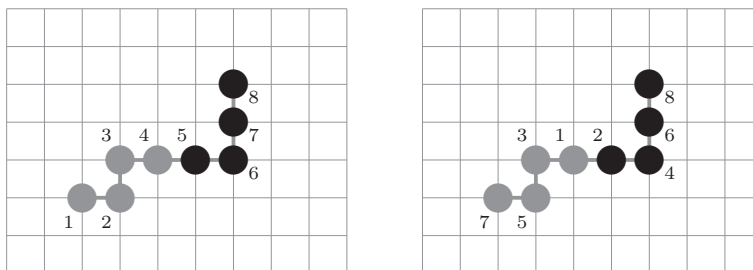
Figure 2.2: Two possible ways of growing an A–B block copolymer—sequentially (left) or simultaneously (right). The numbers represent the order for adding monomers, A and B type monomers are depicted as gray and black discs.

[24, 25], which is known as a high-quality generator. As `ran2` gave comparable results to Ranlux, it was chosen for the reasons of good performance and its long period (the number of calls can reach the order of 10^{11} in a single run).

2.1.4 Constructing a Micelle

The description of the algorithm so far has been dealing with one homopolymer chain only. A proper growth order has yet to be developed in order not to introduce artificial biases for the case of A–B block copolymer micelles. Two monomer types were introduced by their interaction features. While corona monomers are simple SAW chains, core monomers exhibit additionally thermal interactions to nearest neighbors.

To ensure equal growth conditions for the two branches of a copolymer chain, it is necessary to grow the A and B branches simultaneously beginning from the connection monomer, rather than sequentially beginning from one end of the chain, as shown in Figure 2.2. This procedure results in the logarithm of the partition sum $\ln Z_N$ being a linear function of N, contrary to the sequential case, where $\ln Z_N$ deviates from the linear behavior, see Figure 2.3. In extension to the micelle case, this consequently means that

- the whole micelle has to be grown simultaneously, adding the first A type monomer to each chain, then the first B type monomer, then the second A type one and so on, and

- the starting points for all unimers have to be assumed to lie in a spherical shell around the center of mass of the whole aggregate, this spherical shell is also the place where the micellar core region and the corona intersect.

The *Starting Point Sphere*

Starting points, i.e. the most central A type monomers of each chain, were placed randomly on the surface of a sphere centered at the origin of the lattice. They were obrtained by computing a random vector, scaling its length to an assumed spherical radius (given as an input to the runs) and displacing the obtained point to the next lattice point. By virtue of this rounding step a slight broadening of the radial distribution of the starting points was already
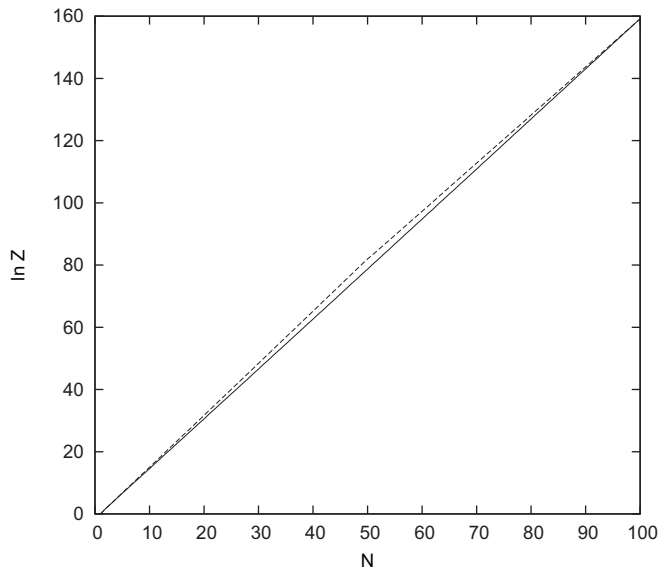
Figure 2.3: Logarithm of the partition sum $\ln Z_N$ vs. chain length N for sequentially (dashed) and simultaneously grown chains (full line).

obtained. It was assumed that this radial distribution was still too narrow, so an additional broadening step prior to the rounding to distinct lattice sites was applied. This broadening was achieved by altering the radius of a starting point by adding a random number around 0 - either uniformly distributed or Gaussian. Where Gaussian distributed random numbers were obtained using the Box–Muller method [6].

The optimal radius for the starting point sphere was then determined by comparing the estimates for the partition sums for different given radii.

Biased Chain Growth

Applying the method as described so far did not yield a large number of successfully constructed micelles necessary for good statistics (i.e. a large number of independent configurations resulting in relatively small errors), but many "savage" aggregates with a poor monomer separation, low density in the core and an accordingly low weight in the ensemble.

The trick that was applied successfully to circumvent this problem was to bias the chain growth. This was done by altering the probabilities of the imortance sampling PERM method in the following way: Taking n as the number of the new monomer to put, counted for a corona or core block in the order of the chain growth (i.e. $n = 1$ for the central monomers, which are connected to the other block). Then the probability to choose the site was multiplied by b (in addition to the weights according to thermal interactions), with

$$b = \frac{2(n-1) + 3}{2(n-1) + 1} \tag{2.19}$$

for new core monomer sites at smaller radii and corona monomer sites at larger

12

radii than the old position, thus e.g. the smaller radii sites were favored by $b = 3$, $\frac{5}{3}$, $\frac{7}{5}$,... for the first, second, third,... core monomers. The probabilities to choose positions at larger radii for core monomers and smaller radii for corona monomers were multiplied by b^{-1}. Additionally, the probablility for the potential positions of the new A-type monomers in the core was multiplied by the number of empty sites in vicinity to the new position—in order to reduce the number of dead ends. This was carried out only at radii smaller than the given starting point sphere (without any broadening) and an additional low(er) density phase of an assumed thickness of 1.5 lattice units. The resulting new chain weights had then to be corrected at the end of the step by diving by the corresponding factors for the site chosen in order to obtain the correct result.

This procedure yielded the desired large numbers of independent configurations with high weights even for the bigger aggregates.

2.1.5 Computing Radial Distributions

Computing radially varying properties, such as probability distributions or density profiles require special care as the lattice may introduce a spurious structure to them. In the case of micelles, where the reference point is the center-of-mass of the configuration (assuming $m_A = m_B$), the lattice degeneracy is avereaged out to a large extent by summing over a large number of configurations. But when some fixed origin is taken as the reference point, around which the system is constructed, as in the cases of chains tethered to a sphere or starting points the degeneracy becomes disturbing and the obtained profiles have to be corrected for it. The correction is done by relating the monomers found in a bin to the total number of lattice sites in the same bin. In that way the correct values are obtained. Note that there is still a spurious structure in the radial functions stemming from the discretized coordinates. Figure 2.4 shows the case of radial bins of width 0.5 lattice units. There is a considerable even–odd pattern in the total number of sites per bin, which correspond to the volume in the model. The inset shows the relation to the geometric volume of the spherical shells with same radii.
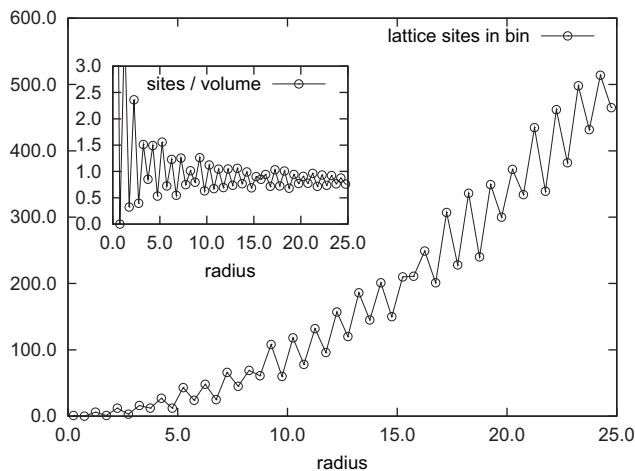
Figure 2.4: Lattice sites of a simple cubic lattice in bins of 0.5 lattice units. The inserted graph shows the number of sites per volume which was used for corrections.

2.2 Results

At the beginning of this section results for some simple systems are presented. These systems have been studied already by others and data are found in literature. Hence the following five subsections, namely the studies of single chains, semi-dilute solutions, polymer brushes and polymers grafted onto a spherical surface, allow to test the validity of the approach and show strengths and weaknesses of the method. Results for symmetric A–B block copolymer micelles—the main subject of this work—are finally presented in the last subsection.

2.2.1 Single Chain

Computations for the simplest case of a single, linear homopolymer chain are the first step in this work and in a sense the foundation of the other, more complex systems. Rather precise data from a broad variety of methods and features of the model exist for the SAW.

Single chains with $N_{\max} = 5000$ monomers were grown in a cubic box of $L = 600$ with periodic boundary conditions. The box size was checked for finite size effects by test runs in a larger box (with size 700). Averages and error estimations stem from an ensemble of 20 runs with $5 \cdot 10^5$ Monte Carlo steps each.

As PERM yields estimates of the partition sum Z_N (or the number of possible configurations $\mathcal{N}_N$ for a chain of N monomers) as its basic quantity, one is able to obtain the universal scaling exponent γ. In practice, the scaling relation 2.3 is reached only at very long chain lengths and the assymptotic approximation of the data is quite slow. Additionally, data exhibit an odd-even pattern if plotted against N due to the structure of the cubic lattice. For these reasons special care has to be taken in extracting the exponent γ [6, 28, 20]: Using triple ratios $Z_{aN}^x Z_{bN}^y / Z_N$ instead of Z_N and introducing a correction term to scaling of the form $\gamma_{\text{eff}}(N) = \gamma + \text{const} N^{-\Delta}$. A value of $\Delta \approx 0.5$ is usually found for
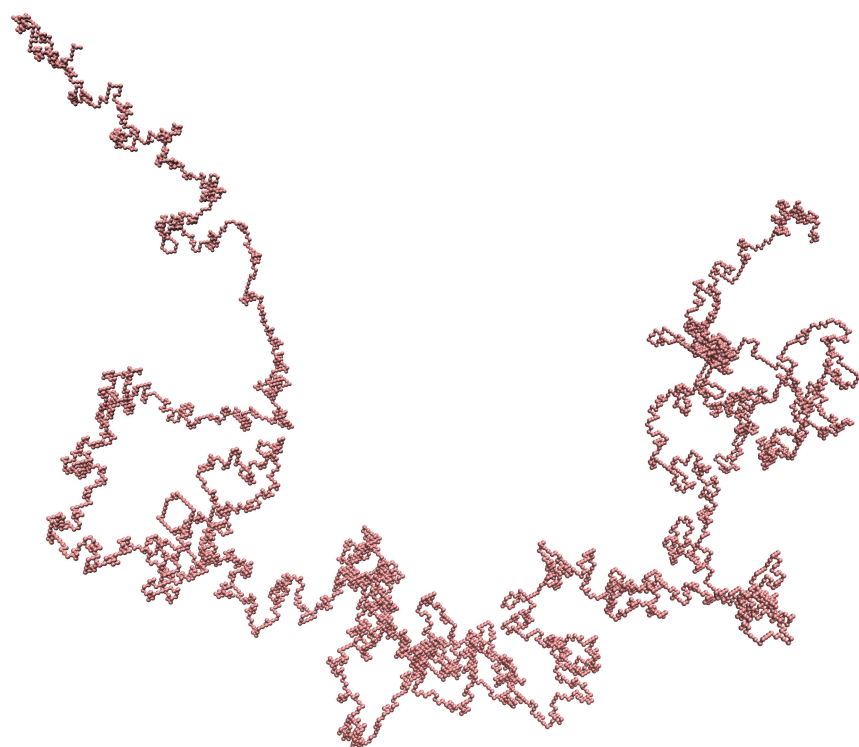
Figure 2.5: Snap shot of a single SAW chain of 5000 monomers on the simple cubic lattice. This and all later snap shots pictures were produced using VMD [31].
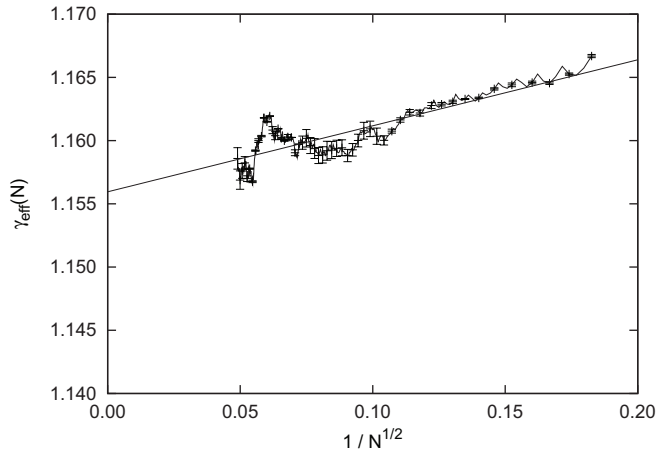
Figure 2.6: Plot of $\gamma_{\text{eff}}(N)$ against $N^{-1/2}$ with only a limited number of error bars shown for better clarity. The linear fit is $1.1560 + 0.0522N^{-1/2}$.

the SAW (for a discussion on Δ see [29]).

Figure 2.6 shows a plot of γ_{eff} which was obtained from

$$\gamma_{\text{eff}}(N) = 1 + \frac{23\ln Z_N - 22\ln Z_{N/2} - \ln Z_{12N}}{\ln(2^{22}/12)} \tag{2.20}$$

with a, b, x and y chosen such that errors are minimized and $\tilde{z}$ and the normalization factors for the different terms cancel. The data show less statistical quality for larger N, hence the asymmteric choice of a and b. The result is

$$\gamma \approx 1.156 \pm 0.001 \tag{2.21}$$

where the error estimate stems from both, the errors inherent to the data for $\ln Z$ and the linear fit. A value that is in line with other work [28, 20, 29]. The value for Δ was estimated to the usual value of 0.5, which gave the most linear behavior of the data.

Inserting the value for γ into Equation 2.3 and extrapolating to the limit $N \to \infty$, one obtains an estimate for the effective coordination number (or the inverse critical fugacity) for the simple cubic lattice of

$$\tilde{z} \approx 4.684 \pm 0.004 \tag{2.22}$$

where the error stems mainly from the uncertainty of γ. Hence the result of Hegger [30] for the same system and method is reproduced.

Geometric observables that were obtained are ensemble averages of the (squared) radius of gyration $\langle R_g^2 \rangle$ and end-to-end distance $\langle R_{\text{ee}}^2 \rangle$. Again to yield the exponent ν according to Equation 2.2 a careful analysis of the data is necessary [6], using a ratio method and a correction to scaling $\nu_{\text{eff}}(N) = \nu + \text{const} N^{-\Delta}$ similar to the corrections for γ.

The ratio formula

$$\nu_{\text{eff}}(N) = \frac{\ln\langle R_g^2(8N)\rangle - \ln\langle R_g^2(N)\rangle}{\ln 16} \tag{2.23}$$
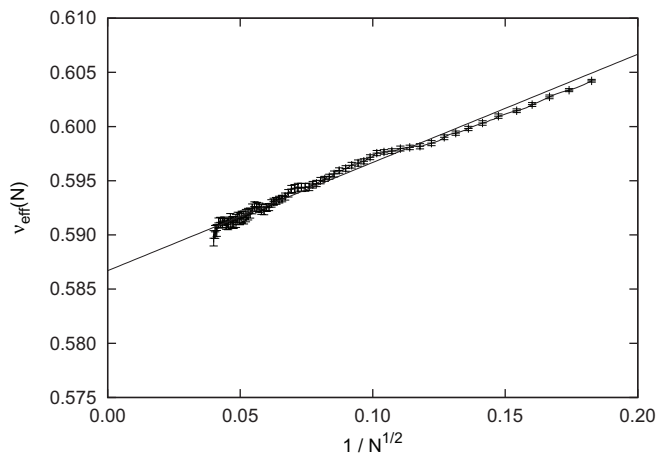
Figure 2.7: Plot of $\nu_{\text{eff}}(N)$ against $N^{-1/2}$ with only a limited number of error bars shown for better clarity. The linear fit is $0.5867 + 0.09985 N^{-1/2}$.

gave smallest errors. Values for $\nu_{\text{eff}}(N)$ were then plotted against $N^{-1/2}$ which gave again a close-to-linear behavior, see Figure 2.7. The result is

$$\nu \approx 0.587 \pm 0.001 \tag{2.24}$$

where the error estimate stems again from both, $\langle R_g^2 \rangle$ and the linear fit. This value is once again in line with other work [28, 20, 29]. $\langle R_g^2 \rangle$ was used instead of $\langle R_{\text{ee}}^2 \rangle$ because it gave smaller errors.

2.2.2 Semi-Dilute Solutions

The osmotic pressure Π of a polymer solution is related to the change in free energy F upon change of the solution's volume (i.e. by adding solvent) while keeping the number of chains fixed

$$\Pi = \left. \frac{\partial F}{\partial V} \right|_{\text{number of chains}} \tag{2.25}$$

In the dilute regime, when the chains do not overlap, it obeys van't Hoff's law[5] $\Pi/T \sim c/N$. At increasing concentrations there exists an overlap concentration (or region) c^* at about the local concentration inside a single coil in a good solvent [5][6]

$$c^* \approx N/R_F^3 = a^{-3} N^{1-3\nu} \approx a^{-3} N^{-4/5} \tag{2.26}$$

or, in terms of the polymer fraction ϕ (i.e. the fraction of lattice sites occupied by monomers, with $\phi = a^3 c$), one obtains $\phi^* \approx N^{-4/5}$. Note that c^* (or ϕ^*) is

---

[5] An improved approximation yields the virial expansion $\Pi/T = c/N + A_2 c^2 + \dots$.

[6] While for experimentalists the form $c^* \approx \frac{3M}{4\pi N_A R_g^3}$ involving the polymer's molar mass M, its radius of gyration R_g and Avogadro's number N_A may be more useful [33]. See also footnote on page 23.

17
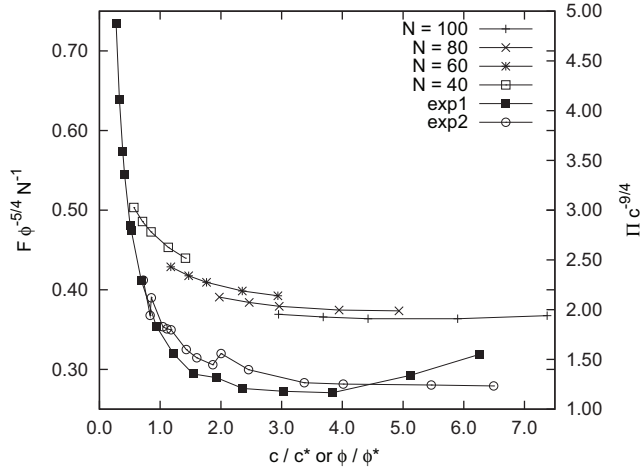
Figure 2.8: Plot of $F\phi^{-5/4}N^{-1}$ against ϕ/ϕ^* for chains of length 40, 60, 80 and 100 monomers. Experimental data in the form of $\Pi c^{-9/4}$ against c/c^* from [36] are also given (*exp1* refers to poly(α-methylstyrene) in toluene of $\bar{M}_n \approx 7 \cdot 10^4$ g/mol, *exp2* to a sample with $\bar{M}_n \approx 2 \cdot 10^5$ g/mol).

small for long chains. For $c \gg c^*$, i.e. semi-dilute solutions in good solvents, the osmotic pressure follows des Cloizeaux's rule [5, 7, 32, 33]

$$\frac{\Pi}{T} \sim c^{\nu d/(\nu d-1)} \approx c^{9/4} \sim \phi^{9/4} \qquad (2.27)$$

Consequently, the free energy per chain in the solution must scale as $F \sim \phi^{5/4}$.

PERM runs were carried out in a box of $L = 30$ with periodic boundary conditions in all directions. Starting monomers for each chain were distributed randomly in the box and chains grown simultaneously (as described in Section 2.4). The system was checked for finite size effects by test runs in a larger box (with $L = 40$).

Figure 2.8 depicts results from for chains of length 40, 60, 80 and 100 monomers. Where the free energy per chain F was obtained as the difference between the logarithm of the partition sum of a single chain and the value for one chain of the same length in the semi-dilute solution $F_N = \ln Z_N^{1,\text{single}} - \ln Z_N^{1,\phi}$. The function $F\phi^{-5/4}N^{-1}$ should assume a constant value in case scaling law 2.27 is fulfilled. This is in fact seen for polymer fractions well above the overlap value $\phi/\phi^* \gg 1$.

Experimental data for poly(α-methylstyrene) in toluene are plotted for comparison. Here the measured osmotic pressures Π over $c^{9/4}$ show a similar behavior for concentrations $c/c^* \gg 1$. The increase in F or Π at higher concentrations may be the onset of the ideal behavior found for melts or mixtures with polymer fractions $\phi \to 1$.

At a concentration in the semi-dilute regime $\phi \gg \phi^*$, the scaling law for the end-to-end distance $R_{\text{ee}}(\phi)$ is for the athermal SAW [5, 32]

$$R_{\text{ee}}^2(\phi) \sim N\phi^{(1-2\nu)/(\nu d-1)} \sim R_{\text{ee}}^2(0) \left(\frac{\phi}{\phi^*}\right)^{(1-2\nu)/(\nu d-1)} \qquad (2.28)$$

18
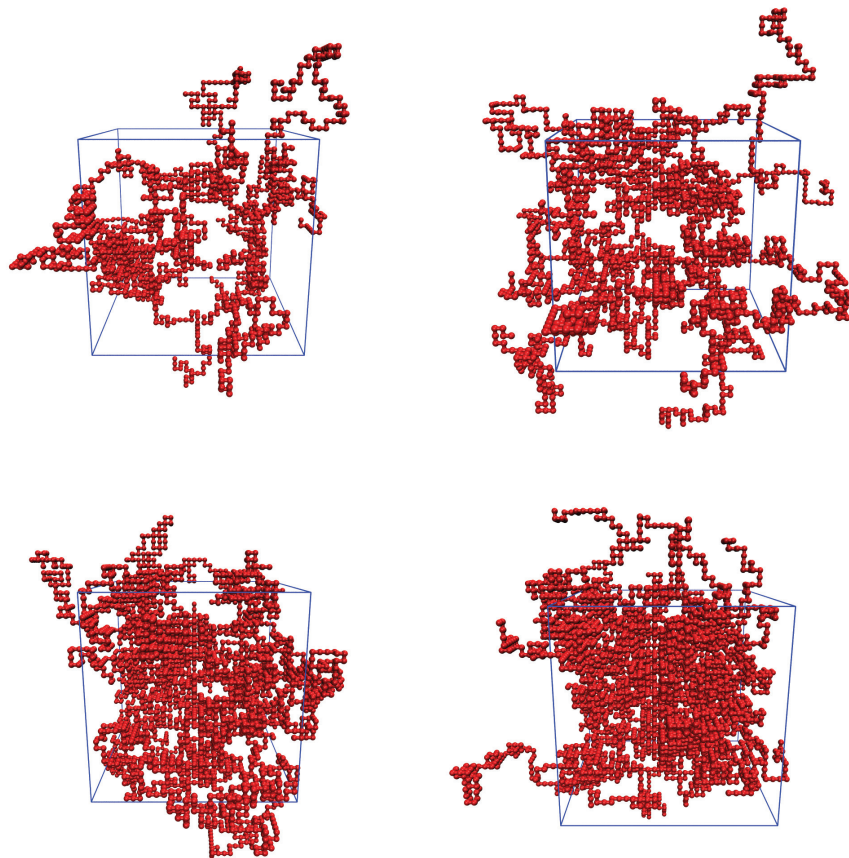
Figure 2.9: Snapshots of chains of 100 monomers in semi-dilute solution. The box of $L = 30$ contains from top left to bottom right 20, 30, 40 and 50 chains, corresponding to $\phi = 0.074 \ldots 0.185$.
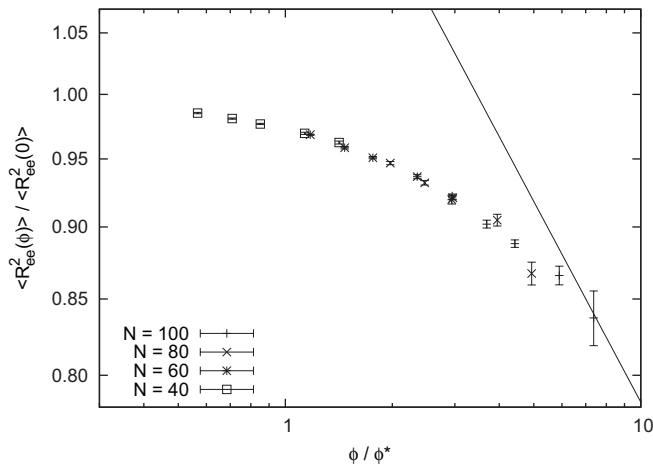
Figure 2.10: Double logarithmic plot of $\langle R_{ee}^2(\phi)\rangle/\langle R_{ee}^2(0)\rangle$ against ϕ/ϕ^* for chains of length 40, 60, 80 and 100 monomers. The expected scaling behavior for $\phi/\phi^* \gg 1$ is marked by the full line.

where $R_{ee}^2(0)$ is the radius of a chain at zero concentration (i.e. for the single chain). Taking $\nu \approx 0.588$ one obtains $R_{ee}^2(\phi)/R_{ee}^2(0) \sim (\phi/\phi^*)^{-0.23}$. The radius of gyration $R_g(\phi)$ is expected to behave essentially proportional to $R_{ee}(\phi)$ [32]. This scaling law was confirmed by neutron scattering experiments [32] and simulations [34, 35].

As can be seen from Figure 2.10 the expected scaling behavior of $\langle R_{ee}^2(\phi)\rangle$ is not fully reached within the data range of this work (slope marked by the full line in Figure 2.10). This deviation is likely due to the fact that the linear scaling with N is not reached for chains of $N_{max} = 100$ and strong corrections to scaling are present for SAWs, what was already noted by Pelissetto [35].

2.2.3   A Single Chain Grafted onto a Planar Inert Surface

Before looking at polymer brushes I want to present the case of a single chain tethered to a surface. This surface was inert, i.e. there were no thermal interactions with the chains, but the lattice sites occupied by the surface were not accessible for monomers. The simulation box had size $L_x = L_y = 500$, $L_z = 1001$ and periodic boundary conditions in lateral directions x and y. The lateral box dimension was checked not to introduce any finite size effects. The inert surface was realized by occupying the plane $(x, y, 1)$ with (athermal) monomers. Chains with up to $N_{max} = 1000$ monomers were constructed while the starting monomer was always in the plane $z = 2$. An ensemble of 10 runs of 10^6 Monte Carlo steps was used for an estimation of means and statistical errors.

As the chains are constructed on the same simple cubic lattice like the free chains before, the critical fugancity stays $\tilde{z} \approx 4.684$, but one finds another exponent $\gamma_s(1)$ from the partition sums [37] due to the effect of the wall.
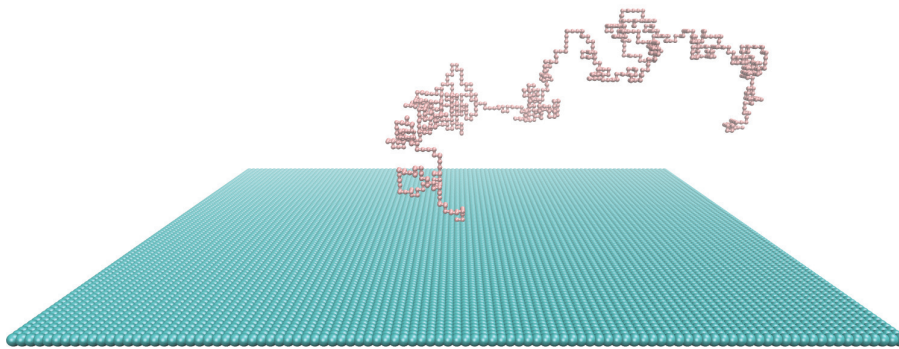
Figure 2.11: Snap shot of a single SAW chain of 1000 monomers grafted on a planar surface. Only a part of the surface is shown for clearity.
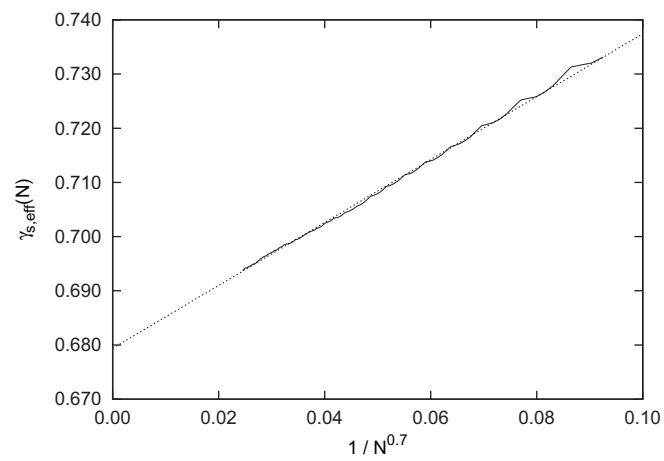
Figure 2.12: Plot of $\gamma_{s,\mathrm{eff}}(N)$ against $1/N^{0.7}$ (red line) and linear fit. The error bars are within line width.
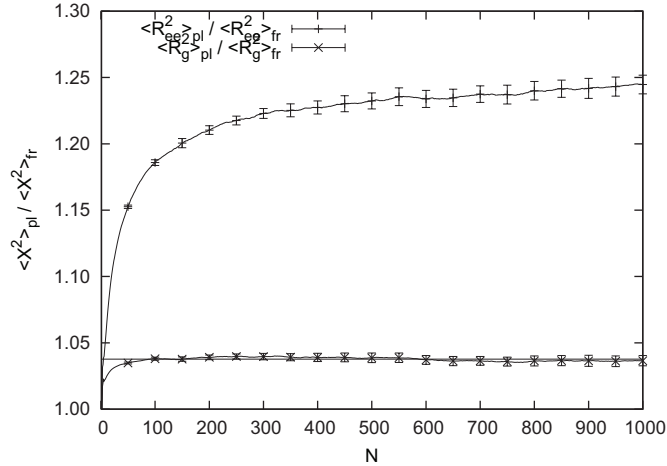
Figure 2.13: Plot of the fraction $\langle X^2 \rangle_{\text{pl}} / \langle X^2 \rangle_{\text{fr}}$ for the mean-squared end-to-end distance $\langle R_{\text{ee}}^2 \rangle$ and radius of gyration $\langle R_{\text{g}}^2 \rangle$ for free (fr) and tethered chains (pl). Only a limited number of error bars is shown for better clearity.

Similar to the free chain case above, γ_s was obtained from the ratio formula

$$\gamma_{s,\text{eff}}(N) = 1 + \frac{7 \ln Z_N - 6 \ln Z_{N/3} - \ln Z_{5N}}{\ln(3^6/5)} \tag{2.29}$$

and plotted against $N^{-0.7}$ what gave the closest-to-linear behavior, as shown in Figure 2.12. The result for γ_s is

$$\gamma_s \approx 0.6794 \pm 0.0004 \tag{2.30}$$

reproducing former PERM results for the simple cubic lattice of 0.6786 ± 0.0012 [37] and 0.679 ± 0.002 [30], and in excellent agreement with the field theoretic result 0.680 [38].

As shown in Figure 2.13 the mean-squared end-to-end distance $\langle R_{\text{ee}}^2 \rangle$ and radius of gyration $\langle R_{\text{g}}^2 \rangle$ seem to assume a constant elongation upon tethering the chain to a wall, which was reported previously [39]. The elongation of $\langle R_{\text{g}}^2 \rangle$ was roughly 1.038 ± 0.001, obtained as mean of chains with $100 \leq N \leq 1000$, while the elongation of $\langle R_{\text{ee}}^2 \rangle$ approaches a value of ≈ 1.25 but seems to be unconverged for the chain lengths studied.

2.2.4 Polymer Brushes

Polymer brushes consist of many chains end-tethered to a planar surface, see Figure 2.14. Like in the single chain case before this surface was inert and impenetrable. The system was constructed in a box with $L_x = L_y = 30$ and $L_z = 101$ and periodic boundary conditions in lateral directions x and y. Lattice sites lying in the plane $(x, y, 1)$ were filled with monomers resembling the inert surface. Then starting monomers were distributed randomly onto this surface (i.e. in the plane $(x, y, 2)$). In case two starting monomers were to be put at the same site then the distribution step was repeated. The box size was checked
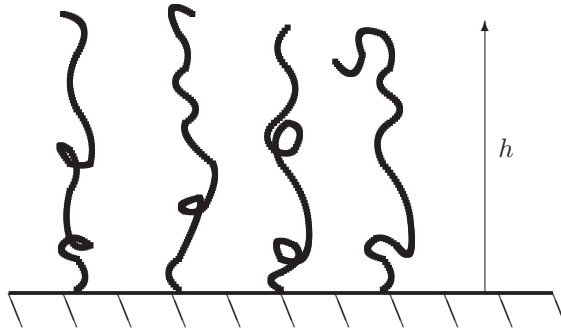
Figure 2.14: Scheme of a polymer brush with brush height h measured in a suitable way, see text for details.

for finite size effects by comparing with results from test runs using a lateral side length of 40. As in the case of semi-dilute solutions, chains were grown simultaneously.

The grafting density ϕ_a for this system is simply the number of chains f divided by the (x, y)-plane area $\phi_a = f/(L_x L_y)$. At very low grafting densities (*mushroom regime*) the distance between chains is large and interchain contacts do not play an important role, if any. Above an overlap grafting density ϕ_a^* which corresponds to the average distance between two chains D equals the Flory radius[7] R_F

$$D \approx R_F \approx N^{3/5} \tag{2.31}$$
$$\phi_a^* \sim D^{-2} \approx N^{-6/5} \tag{2.32}$$

chains become more and more stretched until the *strong stretching regime* is reached at high grafting densities, where the chains are predominantly stretched along the normal of the surface and the polymer fraction inside the brush becomes approximately constant [48].

The brush height h can be measured in terms of the first moment of the z-distribution of momomers $\langle z \rangle$ [41]. In the mushroom regime, when $\phi_a < \phi_a^*$, h is almost independent of ϕ_a. Above the overlap grafting density two regimes were observed. For intermediate densities $\phi_a^* < \phi_a < \phi_{a1}$ a scaling behavior of $h \sim N\phi_a^{1/3}$ was found, where for higher densities above another threshold ϕ_{a1} a scaling law of $h \sim N\phi_a^{1/2}$. This was found by both, MD simulations [41] and theoretical considerations [42]. As both thresholds ϕ_a^* and ϕ_{a1} depend on N, the intermediate regime may be very limited or completely absent. This is in particular true for shorter chains.

Figure 2.16 (a) shows $\langle z \rangle$ for a range of grafting densities ϕ_a, reduced by the overlap grafting density ϕ_a^* and different chain lengths. There is only a limited range of grafting densities accessible by the method, above which the data become quite uncertain and start to behave erroneously (brush height stays constant or even decreases). Apparently the lattice is too unflexible for

---

[7]Newer literature tends to replace R_F with R_g, the radius of gyration, which is smaller by a factor of $\sqrt{6}$. In any case, only a prefactor, not the scaling law is changed. See also footnote on page 17.
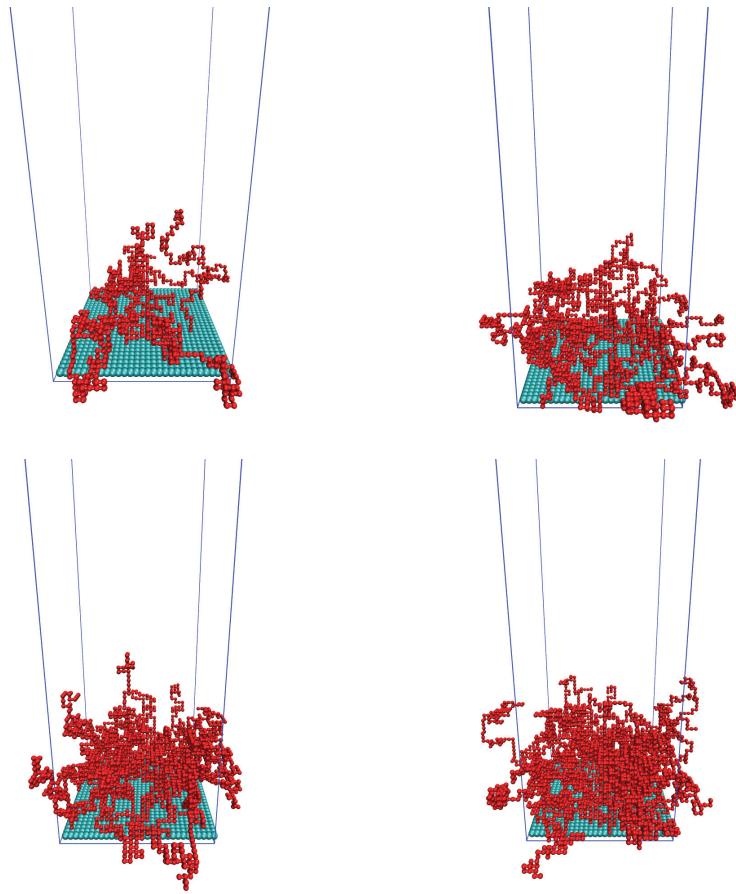
Figure 2.15: Snapshots of polymer brushes containing chains of $N = 100$ monomers. From top left to bottom right the box contains 10, 20, 30 and 40 chains, corresponding to a grafting density ϕ_a of 0.011, 0.022, 0.033 and 0.044.
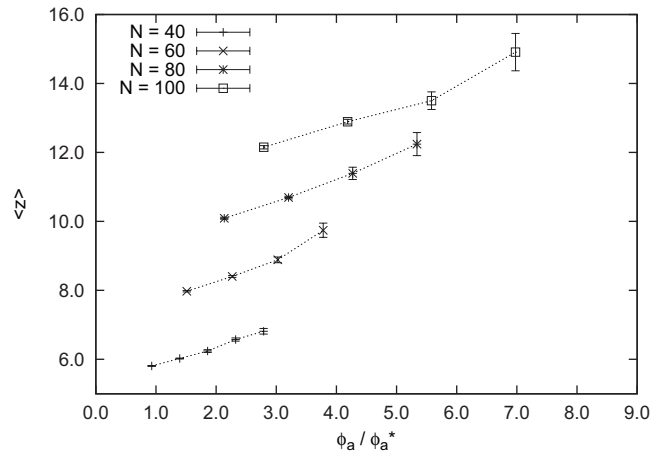
(a)
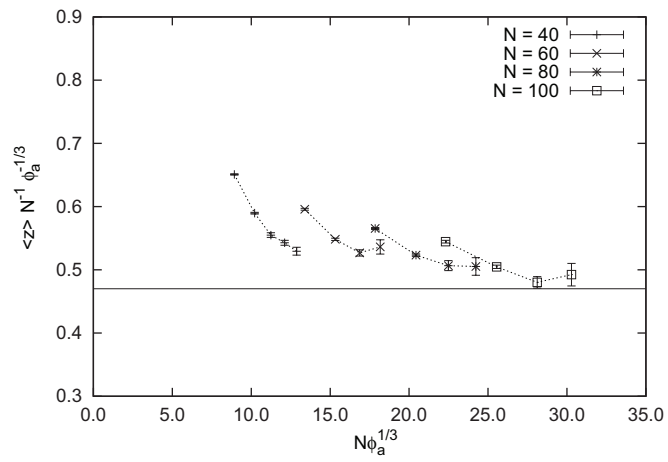
(b)

Figure 2.16: The brush height h, measured as $\langle z \rangle$ against ϕ_a/ϕ_a^* for different chain lenghts N (a) and scaled plot of $\langle z \rangle$ following [41] (b). Lines are guides for the eye only.

Figure 2.17: Plot of the monomer densities $\phi(z)$ for polymer brushes with grafting densities $\phi_a = 0.011 \ldots 0.044$. The lines are just guides to the eye.

growing chains at these high densities. A scaling plot of $\langle z \rangle$ following [41, 42] is depicted in Figure 2.16 (b). At higher grafting densities and for longer chains the scaling behavior seems to be reached (a constant value in the scaled plot is assumed), while the remarks made for graph (a) concerning the limited data range are still to note, what renders the determination of the scaling somewhat ambiguous. For the shorter chains the scaling $\langle z \rangle \sim N\phi_a^{1/3}$ is rather limited, if at all reached. This was observed for MD simulations [41] and experimentally for a polydimethylsiloxane–polystyrene block copolymer at the ethylbenzoate–air interface using neutron reflectivity measurements [43], where the apparent scaling was found to be almost linear[8].

To study in more detail the cross over of the different regimes, it would be desirable to run simulations in a broader range of grafting densities and in particular also with longer chains. But constructing dense systems by the algorithm would be hardly achieveable and sampling a very large number of degrees of freedom would render the results questionable.

Figure 2.17 shows monomer densities $\phi(z)$ along the z-axis for different grafting densities $\phi_a = 0.011 \ldots 0.044$. As obtained by others [44] the density exhibits a maximum close to the surface. The location of the maximum ξ should scale about as $\xi \sim \phi_a^{-1/2}$. A behavior that could not be obtained from the data, as it was not possible to determine the precise location of the maximum. Beyond the maximum the profiles can be approximated by a parabolic function [44, 45]

$$\phi(z) = A_0 - B_0 z^2 \qquad (2.33)$$

_____

[8]Note that the data of [43] do not allow a precise determination of the scaling exponent for ϕ_a and the data of Figure 2.16 (a) could also be interpreted as "almost linear" behavior.

Figure 2.18: Scaling plots of monomer densities $\phi(z)$, which are expected to collaps to a master curve. The solid line is the scaling law from [44].

where the constants A_0 and B_0 are

$$A_0 \quad = \quad \left(\frac{9\pi^2 \phi_a^2}{32w} \right)^{1/3} \tag{2.34}$$

$$B_0 \quad = \quad \frac{\pi^2}{8N^2 w} \tag{2.35}$$

involving the excluded-volume interaction w which equals $1/2$ for the SAW here.

If one scales the densities $\phi(z)$ by $\phi_a^{2/3}$ and perpendicular distances z by $N\phi_a^{1/3}$ all data should collaps to a master curve. The scaled plot along with the parabolic function 2.33 is depicted in Figure 2.18. There is a significant deviation from the proposed scaling. This observation is contrary to the work of Chakrabarti and Toral [44] who also used a simple cubic lattice, but a dynamic Monte Carlo scheme, and to the work of Lai and Binder [45] who used the bond fluctuation model, i.e. also a dynamic scheme. It appears therefore that a static MC algorithm, which grows chains on the simple cubic lattice in regimes of intermediate density does not reproduce their geometric characteristics very well, due to steric hindrance and limited flexibility of the chain.

If one looks specifically at the end monomers of the chains one finds profiles as depicted in Figure 2.19. The free ends are driven towards the outer surface of the brush, but have a non-zero density throughout the entire cross section.

For moderate grafting densities ϕ_a

$$\phi_e(z) = \frac{\pi^2}{4wN^3} z(h^2 - z^2)^{1/2}\theta(h - z) \tag{2.36}$$

was obtained [50, 44], where h is the brush height and w the above mentioned excluded-volume parameter. As before a scaled plot with $\phi_e(z)$ reduced by $\phi_a^{2/3}/N$ and z reduced by $N\phi_a^{1/3}$ should yield a master curve to which all data collapse. This plot is shown in Figure 2.20 along with the scaling law 2.36. There are obvious deviations, in particular the finite density near the grafting
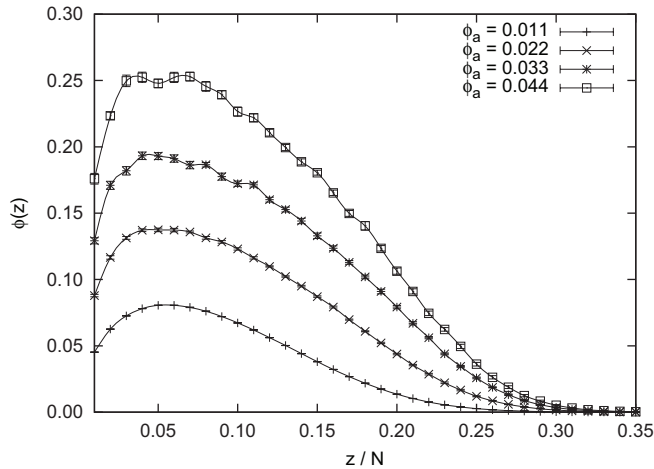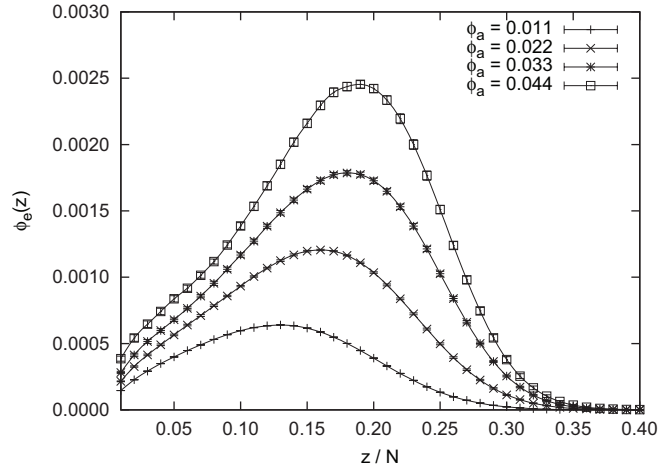
Figure 2.19: Plot of the end monomer densities $\phi_e(z)$ for polymer brushes with grafting densities $\phi_a = 0.011 \ldots 0.044$. The lines are just guides to the eye.
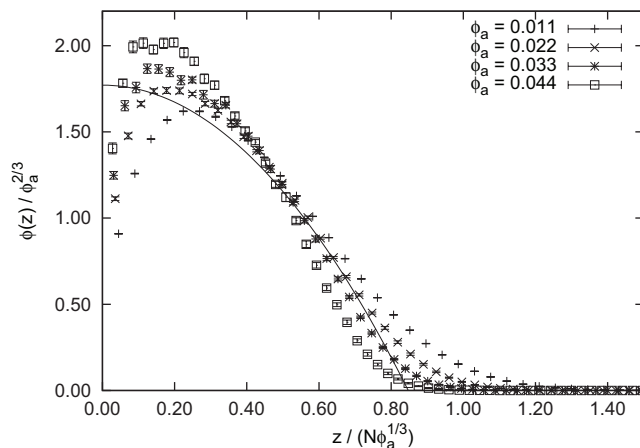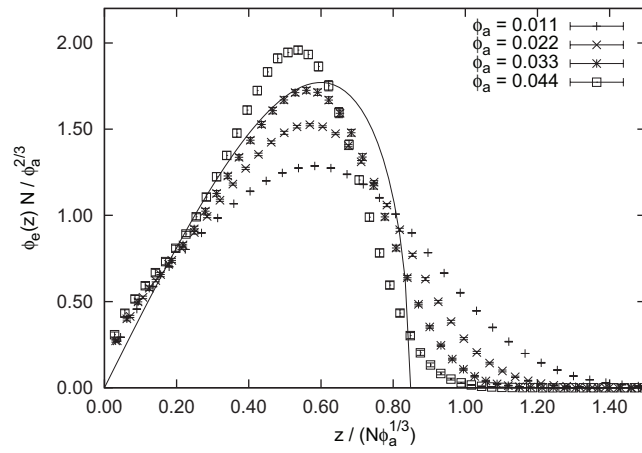

Figure 2.20: Scaling plots of end monomer densities $\phi_e(z)$, which are expected to collaps to a master curve. The solid line is the scaling law from [44].
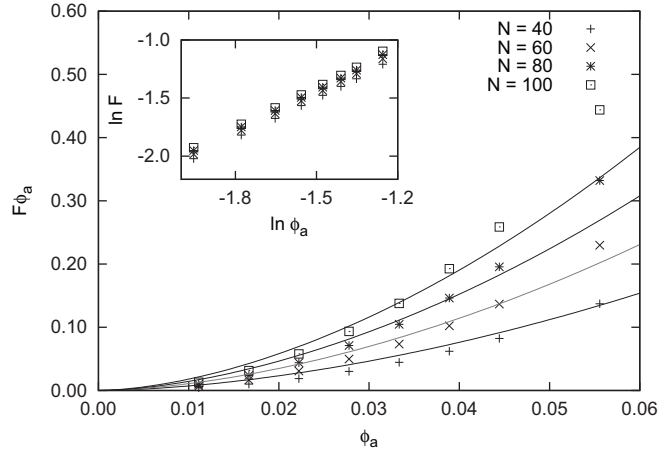
Figure 2.21: Scaling behavior of the free energy per chain F with grafting density ϕ_a for a polymer brush. The lines are a scaling law following [51], see text for details.

plane, which where also found in [44]. Deviations may further be assigned to the sc lattice and potentially the length of the chains which may not have reached the scaling limit. For both densitiy profiles, for whole chains and end monomers, a characteristic "foot" occurs at the right side with respect to the theory. This was found by refined theory and is associated with fluctuations of the free chain ends beyond the brush height h [46].

Related to the bulk osmotic pressure defined in Equation 2.25 one can define a surface osmotic pressure Π_a by

$$\Pi_a = \frac{\partial F}{\partial \phi_a^{-1}} \tag{2.37}$$

involving the surface grafting density ϕ_a and the free energy per chain F. The characteristics of the surface pressure remain under discussion. Above the over-lap grafting density ϕ_a^* scaling theory [47, 48, 49] predicts for a good solvent $\Pi_a \sim N\phi_a^{11/6}$, while SCF theory [50] yields $\Pi_a \sim N\phi_a^{5/3}$. A later work of Carignano and Szleifer [51] using a single-chain mean field approach, while obtaining the field of the other chains from Monte Carlo runs, states that there are constant crossovers between several regimes with respect to the grafting density and only apparent exponents for $N\phi_a^x$ are seen.

Figure 2.21 shows the free energy per chain F which was obained from the estimated of partition sums of a single chain on a planar surface $\langle Z_N^{1,\text{pl}} \rangle$ and the brush with f chains in the simulation box $\langle Z_N^{f,\text{pl}} \rangle$ by

$$F_N = \ln\langle Z_N^{1,\text{pl}} \rangle - \frac{1}{f}\ln\langle Z_N^{f,\text{pl}} \rangle \tag{2.38}$$

The main graph in Figure 2.21 shows a comparison with a scaling law following [51]. The following expansion for the surface osmotic pressure was obtained there

$$\Pi_a = \frac{1}{2}\int \langle \phi(z) \rangle^2 dz + \frac{1}{3}\int \langle \phi(z) \rangle^3 dz + \frac{1}{4}\int \langle \phi(z) \rangle^4 dz + \dots \tag{2.39}$$

29

It was shown that as long as the full expansion 2.39 is used, even the form of the profile $\phi(z)$ plays not a decisive role. In particular this was demonstrated for the parabolic profile[9], see Equation 2.33 above, in which case one obtains

$$\int_0^h \phi(z)^i dz \sim N\phi^{(2i-1)/3} \tag{2.40}$$

From Figure 2.21, where $F\phi_a$ is compared with an expansion up to $i = 10$ and using Equation 2.40, it can be seen that the apparent scaling exponent obtained from PERM is somewhat higher than the one predicted by Equation 2.39. The inset of Figure 2.21 depicts a double logarithmic plot of F against ϕ_a, which yields an apparent exponent of $x \approx 1.163 \pm 0.002$ by linear fit. This consequently means for the surface osmotic pressure that an apparent exponent of scaling ϕ_a^x of $x \approx 2.163$ from this work compares to the value of 1.9 from [51] for the range of ϕ_a studied here. Where the latter figure is based on the originial approach of [51] using MC sampling and employing the rotational isomeric state (RIS) chain model. Another work of Carignao and Szleifer [53], which is based on the bond fluctuation model, yields a scaling exponent for the chemical potential slightly larger than 1, in better agreement with this work. A direct comparison of F vs. ϕ_a from this work with results from an earlier work of Carignano and Szleifer [52], based on pure Rosenbluth sampling of chains on the simple cubic lattice shows the expected close agreement. The above described deviations stem from the chain model used in the different sources. A more recent work of Ohno et al. [54] uses an enrichment algorithm on the sc lattice and obtains for the scaling of the entropy with the (regular) spacing d between chains $-S \sim d^{-y}$ an exponent $y = 2.4 \pm 0.1$. Hence this corresponds to $x = 1.2 \pm 0.05$ for the scaling $F \sim \phi_a^x$, using $\phi_a \sim d^{-2}$, and a good agreement with the present results.

Experimentally the surface osmotic pressure can be measured as the change in surface tension of a liquid interface due to the presence of chains forming the brush as a function of surface coverage. Kent et al. [55] obtained data from neutron reflectivity measurements of a polydimethylsiloxane–polystyrene (PDMS–PS) copolymer at the ethylbenzoate–air interface, where the PS blocks form the brush. There is evidence for scaling exponents $> 5/3$, but the uncertainty of the data does not permit a precise comparison.

2.2.5 Chains Grafted onto a Small Sphere

I have studied systems of this type with respect to the case of block copolymer micelles below, for which they mark a step of simplification and the possibility to check the validity of the appoach. In the limit of small radii for the central sphere R_s to which the chains are tethered the statistics of the system approximate the characteristics of star polymers [56], which are a special class of branched polymers in which all chains are tethered to a point.

Star polymers with a larger number of arms cannot be realized on simple lattices with self-avoiding chains as the dense central region needs some modification. Approaches include allowing longer bonds [57], partially overlapping monomers [20] and use of a small inert sphere [56]. Increasing the radius of

---

[9]Observe that this yields again the former SCF result $\Pi_a \sim N\phi_a^{5/3}$ if the summation 2.39 is aborted after the first term.

Table 2.1: Comparison of γ_f for f chains attached to a small sphere with $R_s = 5.0$ and comparison to MC results and theoretical values for star polymers.

| f | sphere $R_s = 5.0$ | star polymers | |
	this work	MC results	renormalization group
1	0.978(3)	1.1573(2)[a]	1.1575(60)[g]
2	0.920(6)	1.1573[a]	1.1575(60)[g]
4	0.685(8)	0.8355(19)[a]; 0.879(1)[b]; 0.88(3)[c]; 0.71, 0.91[d]	0.75[h]; 0.78[i] 0.83...0.86[j]
8	−0.348(14)	−0.748(3)[a]; −1.00[e]; −0.99, −0.30[d]	−1.50[h]; −0.45[i] −0.88...−0.36[j]
16	−4.77(6)	−6.640(10)[a]; −5.90[e]; −8.80, −5.71[d]	−12.0[h]; −4.54[i]
32	−22.1(3)	−29.0(20)[f]	−57.0[h]; −17.3[i]

[a]Hsu 2004 [20], PERM and Domb-Joyce model. [b]Batoulis 1989 [63], dimerization method on fcc lattice. [c] Wilkinson 1986 [64], Rosenbluth sampling on sc lattice. [d] Barrett 1987 [65], Rosenbluth sampling using (112) and (113) steps on sc lattice. [e] Shida 2000 [66], enrichment algorithm, sc lattice. [f] Ohno 2002 [67], enrichment algorithm, sc lattice. [g] Guida 1998 [68]. [h] Miyake 1983 [65]. [i] Ohno 1988 [63]. [j] von Ferber 2002 [69], various calculation models.

the central sphere above a critical radius R_s^* lets the scaling behavior approximate the case of a planar surface discussed above [49, 56]. The sphere can be considered as small, when [49]

$$R_s \ll R_s^* \sim N\sigma^{-1/3} \tag{2.41}$$

using the area per chain σ, which is obtained from the surface of the sphere with R_s and the number of chains f by $\sigma = 4\pi R_s^2/f$.

The systems as depicted in Figure 2.22 were constructed in the following manner: First all sites of the simple cubic lattice whose distances from some origin smaller than the requested R_s were occupied with inert surface monomers. Then starting monomers for the chains were randomly distributed in the shell around R_s. These starting positions were checked for the number of next neighbor–surface monomers and adjusted to have not less than 1 and not more than 4 of them, see pseudocode in Section 2.4 for details. The other steps of the algorithm were then similar to the ones for the other systems described so far. In computing radial density profiles, lattice degeneracy had be taken care of as descried on page 13.

The partition function of a star polymer of f arms with N monomers is given by a generalization of the expression for a linear chain, Equation 2.3,

$$Z_{N,f} \sim \tilde{z}^{fN} N^{\gamma_f - 1} \tag{2.42}$$

with the same value for $\tilde{z}$ as before. For each star family with f arms, there
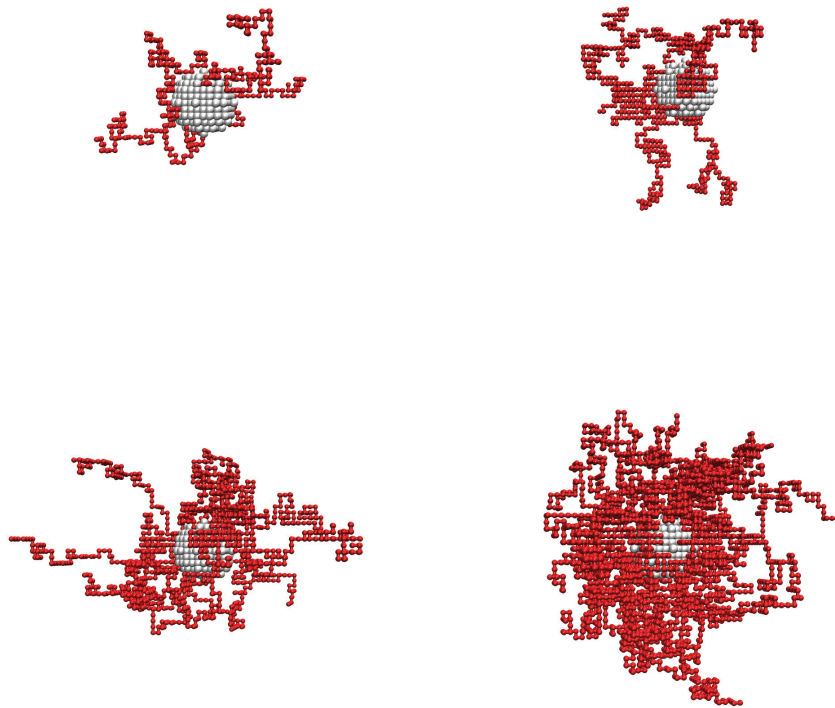
Figure 2.22: Snapshots of SAW chains of 100 monomers grafted onto a spherical surface of radius 5.0. From top left to bottom right the system ontains 4, 8, 16 and 32 chains, corresponding to $\sigma = 78.5$, 39.3, 19.6 and 9.82.
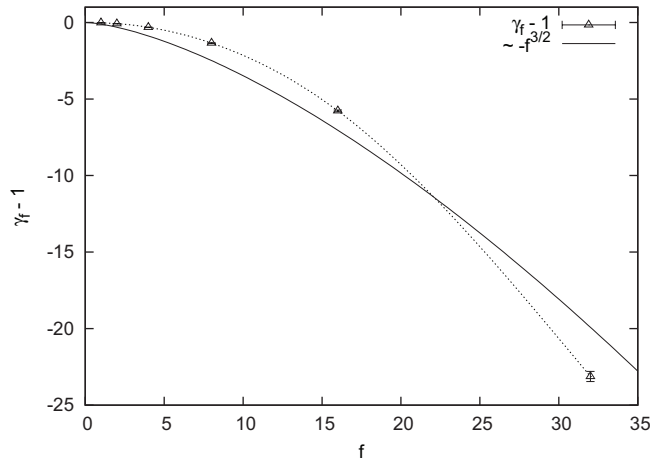
Figure 2.23: Comparison of measured values γ_f for $f = 1 \ldots 32$ with scaling law $\gamma_f - 1 \sim -f^{3/2}$. The dotted line is just a guide for the eye.

exists a different γ_f. Observe that $\gamma_1 = \gamma_2 = \gamma$, which are all linear chains [10].

Table 2.2.5 shows values for γ_f estimated from the present simulations, as well as other MC estimates and theoretical results obtained from renormalization group theory. The γ_f-values from this work exhibit some uncertainty as the chains $N_{\max} = 100$ only and were determined by extrapolating $\ln Z_{N,f} / \ln Z_{N-1,f} = fN \ln \tilde{z} + (\gamma_f - 1)ln[N/(N-1)]$ to $N \to \infty$. As the chains here are attached to a sphere and not to a point, the γ_f-values deviate from literature values. Thus γ_1 assumes an intermediate value between γ and γ_s for a planar wall. The effect of the sphere is less pronounced for large f. As can be seen from Table 2.2.5, there is considerable scattering within the literature values from different sources, even so for the same systems and similar methods. Concerning MC results the more recent data are by trend more precise and are assumed to have higher significance. Theoretical values with tags (h) and (i) are obtained from equations after Miyake and Freed [65] for the limit of few arms

$$\gamma_f = 1 + \frac{1}{8} \left[1 - \frac{(f-1)(f-2)}{2} \right] \tag{2.43}$$

and Ohno [63] for the limit of large f

$$\gamma_f = 1 + (\gamma - 1)f - \frac{1}{3}(\gamma - 1)^{1/2} \left[f(f-1) \right]^{3/4} \tag{2.44}$$

By the simple geometric argument that a chain of the star is confined in a cone (see below) γ_f is expected to scale with f as $\gamma_f - 1 \sim -f^{3/2}$ [70, 67]. This prediction is not very well supported by the exponents from the MC simulations, as is demonstrated in Figure 2.23, and was found also for star polymers before [20].

This observation is coupled with the scaling of the free energy per chain in the form of $\ln Z_{N,1} - 1/f \ln Z_{N,f}$, which is shown in Figure 2.24. The function

---

[10]This is only valid for homopolymer stars, contrary to the block copolymer case described earlier.
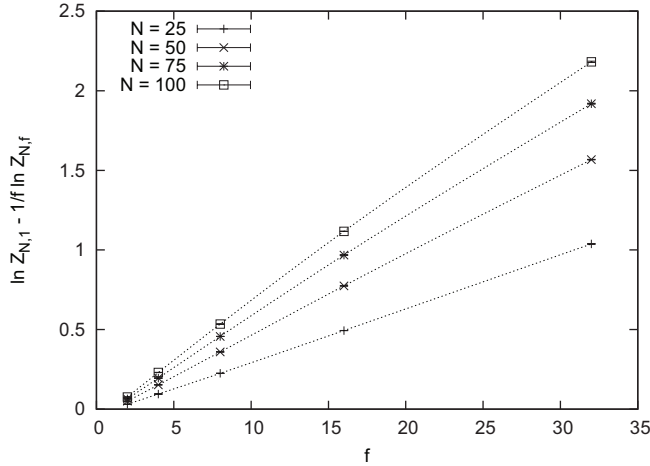
Figure 2.24: Free energy change per chain due to the interaction with the other chains, when grafted to a sphere of $R_s = 5.0$. Lines are guides for the eye only.

exhibits a close-to-linear behavior (the actual exponent increases monotonically, but is always ≈ 1 in the f-range studied), which would suggest a scaling like $\gamma_f - 1 \sim -f^2$, rather than $-f^{3/2}$. Higher exponents are also suggested by MC results of Batoulis [63], Hsu [20] and the above formula of Miyake/Freed.

Daoud and Cotton [58] and Zhulina [49] developed a scaling approach to predict the properties of a star involving the picture of blobs [5], a local region of size $\xi(r)$ in which a branch exhibits the behavior of a single free chain. $\xi(r)$ is a function of the radius r and the number of arms f. In the outer, swollen region the star looks like a semi-dilute solution of a chain of blobs. With $\xi(r) \sim r f^{-1/2}$ and the number of monomers in a blob $n(r) = \xi(r)^{1/\nu}$ one obtains [58, 59]

$$\phi(r) = \frac{n(r)}{\xi(r)^3} \sim f^{(3\nu-1)/2\nu} r^{(1-3\nu)/\nu} \approx f^{0.65} r^{-1.30} \tag{2.45}$$

where a lattice unit of $a = 1$ is assumed and $\nu \approx 0.588$ is used. The profiles $\phi(r)$, scaled by $f^{-0.65}$, are shown in a double logarithmic plot in Figure 2.25. The expected scaling with r is found, compare with the straight line with slope -1.30, in a increasing region of r the more chains are present.

For the mean-squared radius of gyration $\langle R_g^2 \rangle$ and center-to-end distance $\langle R_{ce}^2 \rangle$ Daoud and Cotton [58, 59] state

$$\langle R_{ce}^2 \rangle \sim \langle R_g^2 \rangle \sim N^{2\nu} f^{1-\nu} \approx N^{1.18} f^{0.41} \tag{2.46}$$

$\langle R_g^2 \rangle$ was measured from the monomer positions of the whole system of chains, but disregarding the sphere monomers. $\langle R_{ce}^2 \rangle$ was measured as the distance between the starting monomers on the spherical surface and the end monomers. When the data are scaled by the mean-squared radius of gyration of a single free chain $\langle R_{g1}^2 \rangle$ of the same length as one arm of the star, different chain models and experimental data become comparable.

The mean-squared radii of gyration $\langle R_g^2 \rangle$ and center-to-end (i.e. from the grafting point to the free end monomer) distances $\langle R_{ce}^2 \rangle$, scaled by the radius

34
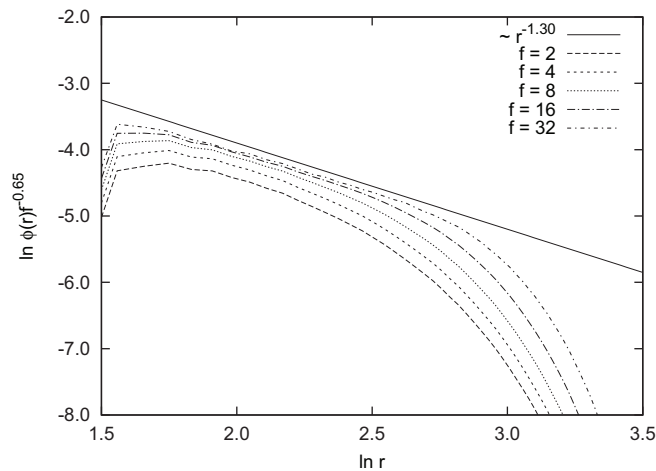
Figure 2.25: Double logarithmic plot of the monomer density profile $\phi(r)$, scaled by $f^{-0.65}$ for f chains end-grafted to a sphere of radius $R_s = 5.0$. The expected scaling with r is represented by the straight line with slope -1.30.
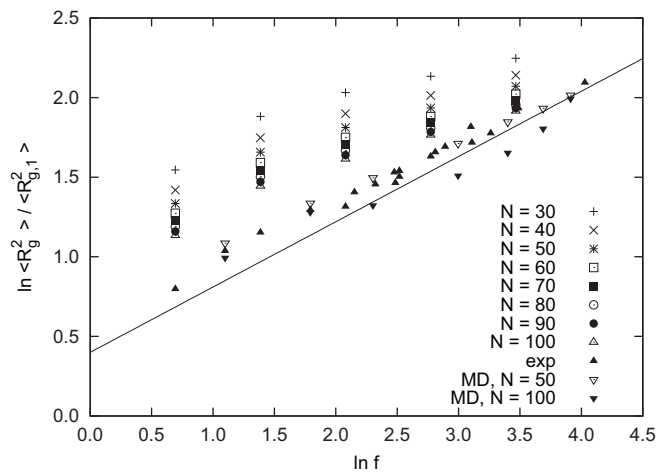
Figure 2.26: Double logarithmic plot of radii of gyration $\langle R_g^2 \rangle$ of f chains attached to a sphere of $R_s = 5.0$, scaled by $\langle R_{g1}^2 \rangle$ of a single chain of same length as one arm. Results from this work along with light scattering data for polyisoprene and polystyrene [60] (exp) and off-lattice MD simulations [59]. The expected scaling with f is represented by the straight line with slope 0.41.
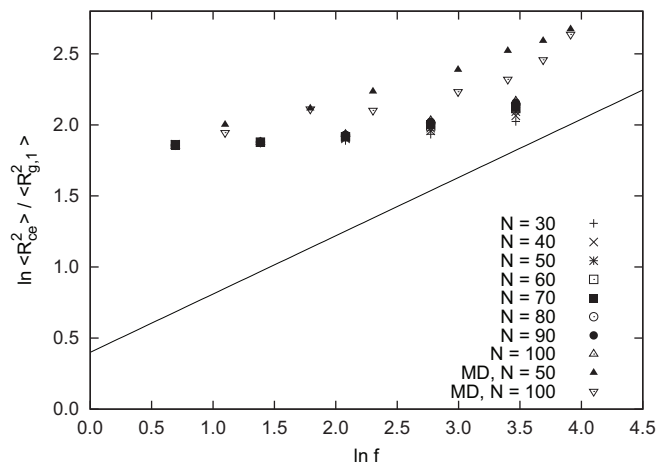
Figure 2.27: Double logarithmic plot of distances between grafting point and free end monomer $\langle R_{ce}^2 \rangle$ of f chains attached to a sphere of $R_s = 5.0$, scaled by radius of gyration $\langle R_{g1}^2 \rangle$ of a single chain of same length as one arm. Results from this work along with data from off-lattice MD simulations [59]. The expected scaling with f is represented by the straight line with slope 0.41.

of gyration of a single chain of the same length as one arm are depicted in Figures 2.26 and 2.27. Along with results from this work experimental data from light scattering experiments for R_g of polyisoprene and poylstyrene stars [60] and simulation data from MD of off-lattice chains [59] are given. One can see deviations of the present data from the expected behavior, which are characteristic for the presence of the sphere to which the chains are tethered. Hence the values of $\langle R_g^2 \rangle$ are offset to larger radii, what stems from the disregard of the central sphere. The effect is fading out towards systems with more and longer chains, as the sphere becomes smaller relative to the length scale of the chains. A similar picture can be deduced from the data for $\langle R_{ce}^2 \rangle$. Compared with $\langle R_g^2 \rangle$, and speaking for the MD results, the scaling behavior sets in at larger numbers of arms for stars. For chains tethered to a sphere (this work), the assumption of scaling behavior is even more shifted to larger f, because the stretching due to the proximity of the other chains is reduced.

From the picture employed in the scaling model involving blobs, it was proposed on geometric arguments that the radial distribution function of end monomers $P(r)$ is expected to approach a Gaussian bell-shaped curve for $f \gg 1$ [59, 61, 62]. As can be seen from Figure 2.28, the measured probability distribution of end monomers does indeed exhibit Gaussian shape. The dotted lines are Gaussians with the same mean and standard deviation as the raw data. As expected and observed with MD simulations [59], deviations from Gaussian shape increase with smaller numbers of chains (arms), in particular the probability of finding a free end close to the grafting point is overestimated by the Gaussian. Observe that the apparent exclusion zone at $r \lesssim 4.5$ stems from the central sphere. Due to the properties of the cubic lattice the effective radius determining the zone of exclusion for chains is somwhat smaller than 5.0.
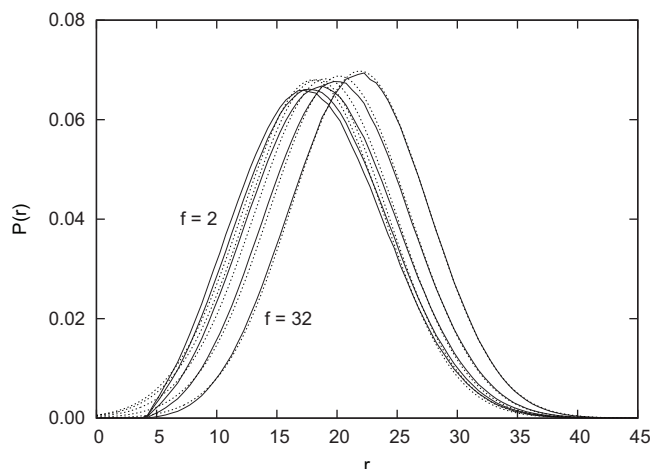
Figure 2.28: Probability distribution functions for end monomers of $f = 2, 4, 8, 16$ and 32 chains grafted onto a spherical surface of $R_s = 5.0$. The dotted lines are Gaussians with same mean and standard deviation as the raw data (full lines).

2.2.6 Block Copolymer Micelles

Constructing copolymer micelles followed the method described in Sections 2.1.4 and 2.4 of putting starting points randomly on a sphere around some origin, broadening their radial distribution and growing all chains and the core and corona block simultaneously. Core and corona monomers differed by their interaction features. While corona chains were simply athermal SAW chains as in the systems presented above, the core chain conformations yielded a Boltzmann factor of 2.0 for each non-chain next neighbor contact. This corresponds to a temperature of 1.443, well below the θ-temperature for the model of 3.717. Snapshots of micelles with association numbers between 6 and 24 are shown in Figure 2.29.

Testing the Micelle Constructing Ansatz

The micelles constructed by the PERM algorithm are not obtained spontaeously from a uniform distribution of unimers in space during a run, but are assumed to be spherical. Moreover, a determined radial distribution of the connection sites between the core and corona blocks is given as an input to the runs. Hence this ansatz had to be tested if it actually corresponds to the features of the system.

This test was achieved by simple dynamical Metropolis type Monte Carlo runs using only so-called reptation moves. As depicted in Figure 2.30, reptation moves chose a polymer chain in the system and then try to shift the whole chain in a randomly chosen direction by deleting a monomer at one end and adding one at the other end. For the case of a copolymer chain this consequently means that an core type monomer is deleted and a corona type one added (or vice versa), and a monomer type flip occurs in the center of the chain. The move is accepted due to the usual Metropolis rules by computing the energy change and comparing it to a random number.
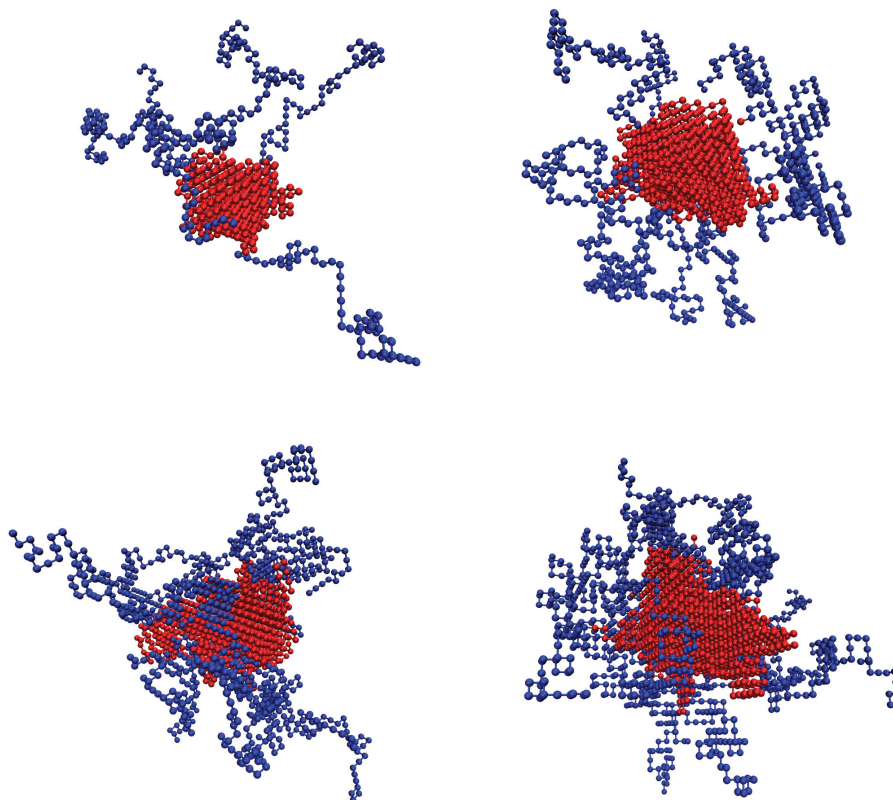
Figure 2.29: Snapshots of block copolymer micelles consisting of 6, 12, 18 and 24 chains of 50 core and 50 corona monomers each.
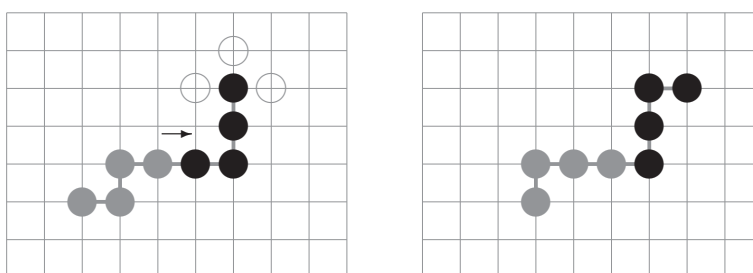
Figure 2.30: Reptation moves (depicted in 2D only for clearity): The original chain (left) is moved to the right and occupies a randomly chosen new position. The result is shown on the right picture.
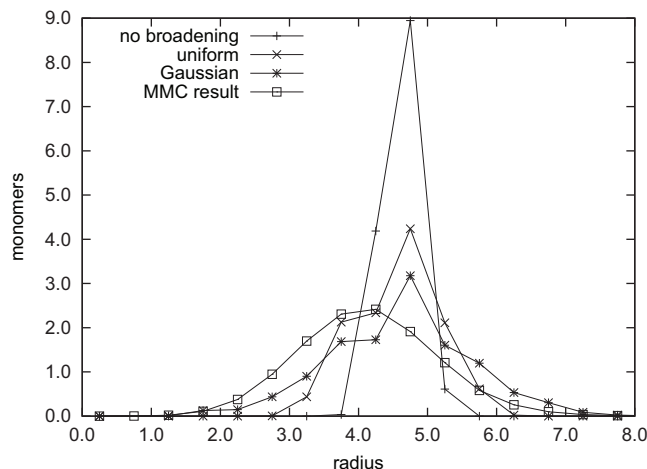
Figure 2.31: Comparison of the starting point distributions for 12 chains, obtained by different methods.

Figure 2.31 shows a comparison of different methods to distribute the starting points in space. There *no broadening* means that the randomly distributed points on the surface of a sphere were solely displaced to the nearest lattice site. In the case of *uniform* additional broadening was obtained by adding uniformly distributed random numbers (between -1.0 and $+1.0$) to the radius of each point prior to rounding to lattice sites. A similar procedure was used in the case of *Gaussian*, where broading was obtained by Gaussian distributed random numbers of variance $\sigma^2 = 1.0$. These three profiles are corrected for the lattice degeneracy (i.e. divided by the number of lattice sites in each bin shell times its volume).

Finally the curve labelled *MMC run* shows the results from a Metropolis run using reptation moves. In this run an ensemble of 27 configurations from an earlier PERM run was equilibrated by 3.8×10^6 MC steps and then the positions of the most central core type monomers were recorded during another 2.5×10^6 steps. Note that the distances in the latter case are measured with respect to the flexible center-of-mass of the actual micelle, where starting points are given at their distances to the origin of the coordinate system.

As can be seen in Figure 2.31, the proposed Gaussian broadening does indeed correspond closest to the radial starting point distribution from the MMC runs. Note that the radii for starting points (and also the radius of the core) decrease during equilibration by MMC reptation moves. This effect corresponds to the shortcoming of the approach of growing chains by PERM to a dense system on the sc lattice. The obtained density in the cores from PERM is somewhat lower than 1, see below.

The spherical shape of the micelle was conserved during Metropolis MC equilibration, apart from a few cases were a chain completely left the aggregate. This was measured by means of the principal moments of inertia for the aggregates, what yielded $I_1 \approx I_2 \approx I_3$, see Figure 2.32.
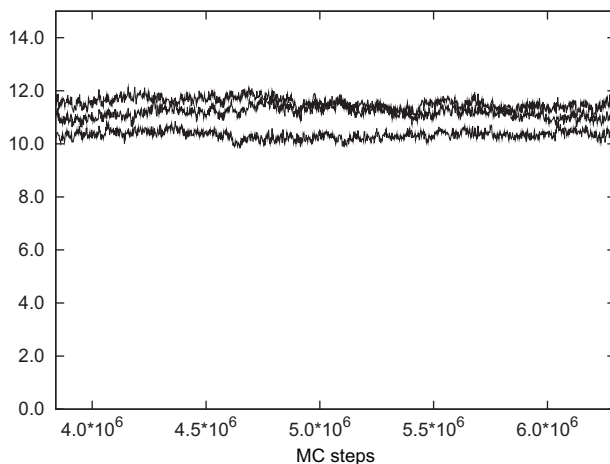
Figure 2.32: Principal moments of inertia I_1, I_2 and I_3 as obtained from Metropolis MC runs using reptation moves. Micelles consisted of 12 chains of 50 core and 50 corona type monomers, runs used averages over 27 conformations and measured every 20000 MC steps, first 3.8×10^6 steps were equilibration.

The Free Energy

To gain insight into the thermodynamic properties of micelles in the framework of the chosen model micelles of different sizes had to be constructed and their free energy in term of $-\ln Z$ had to estimated from the Rosenbluth weights. As the radius of the starting point sphere was assumed (see Section 2.1.4) and input to the runs, a scan over a range of radii had to be carried out in order to obtain the optimal one for a given chain length and aggregation number. These scans were done with a stepsize of 0.5 lattice units. A Gaussian broadening of the radial distribution of starting points with $\sigma^2 = 1.0$ was used in all simulations. Typical results from those scans are depicted in Figure 2.33. Note the dependence of the optimal radius on the chain length, which is the expected behavior. The error estimation stems from the results from 30 independent runs.

Taking the optimized radius for a range of chain lengths N and aggregation numbers f and combining these data results in a diagram as depicted in Figure 2.34, where the gain in free energy (in terms of $-\ln Z$) per chain is shown, when is is transferred from the free non-aggregated state into a micelle of aggregation number f. The error estimation stems from 20 independent simulation runs.

Figure 2.34 shows the free energy as a function of the aggregate size f which exhibits minima at some f. This is the expected behavior, as these minima are responsible for the occurence of micelles in solution.

Critical Micelle Concentration

The following chain of thought is inspired by [71] and [72], but modified to meet the requirements of this work.

Adding an amphiphilic substance to a solvent the following equilibria between unimers Z and aggregates Z_f of size f can be defined

$$fZ \rightleftharpoons Z_f \tag{2.47}$$

40
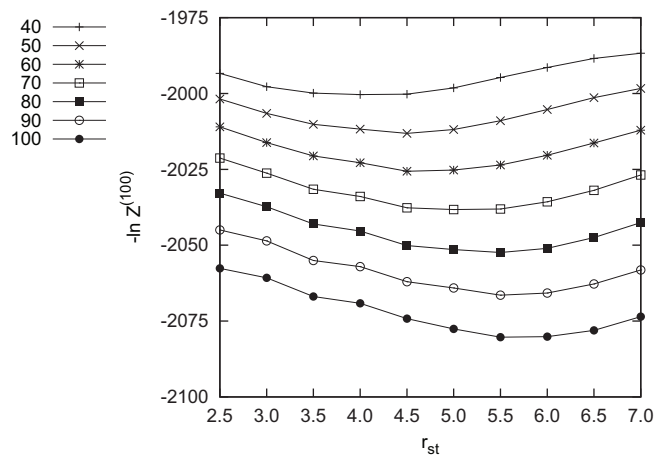
Figure 2.33: Values $-\ln Z$ for 12 chains of different lenghts (40—100) and different radii for the starting point sphere r_{st}. A Gaussian broadening of $\sigma^2 = 1.0$ was used. The scaling on the ordinate corresponds to chain length 100 (black line), the other graphs are shifted. Error bars smaller than symbols.
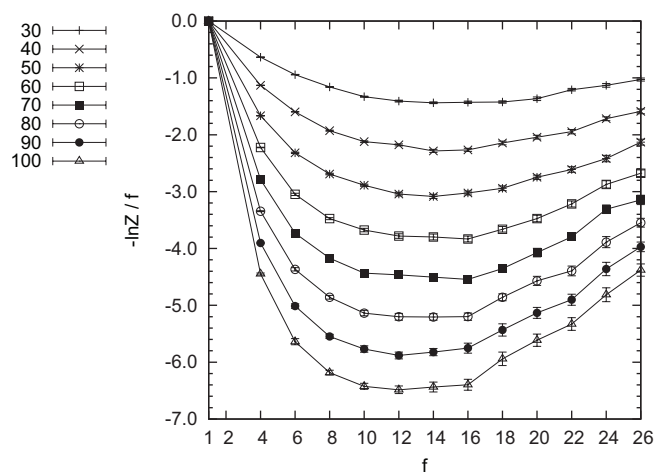
Figure 2.34: Changes in $-\ln Z$ per chain in the micelle in aggregates of different aggregation numbers f.

41

Note that for every aggregate size f such an equilibrium occurs, and these equilibria are coupled to each other. The equilibrium contants K_f are, using the concentrations $[Z]$ and $[Z_f]$

$$K_f = \frac{[Z_f]}{[Z]^f} \tag{2.48}$$

These are related to the change in free energy per chain ΔF_f^0, due to formation of a cluster Z_f of f unimers

$$kT \ln K_f = -f \Delta F_f^0 \tag{2.49}$$

with k being the Boltzmann constant and T the temperature. The fraction of unimers X_f being part of clusters of size f is then

$$X_f = f[Z_f] = f \left[X_1 \exp\left(\frac{-\Delta F_f^0}{kT} \right) \right]^f \tag{2.50}$$

And the total concentration C of amphiphiles is

$$C = X_1 + X_2 + \cdots = \sum_f X_f \tag{2.51}$$

At small amphiphile concentrations C most unimers will be in their free, non-aggregated state. Increasing the concentration forces more and more the formation of clusters, which occurs more or less pronounced at a distinct concentration C (see figure 2.35). The critical micelle concentration (CMC) marks the turnover from the single chain dominance ($X_1 \gg X_2 > X_3 > \cdots$) to the aggregate dominance, around position of arrow (a) in Figure 2.35.

An exacter way of defining the CMC follows [13] and was also used here. It is defined as the equal weight of homogeneous and micellar solutions

$$CMC = X_1^{crit} \approx \sum_{f=2}^{max} \frac{X_f}{f} = \sum_{f=2}^{max} X_1^f \exp\left[\frac{-f \Delta F_f^0}{kT} \right] \tag{2.52}$$

and is hence shifted somewhat to higher concentrations C, qualitatively shown by arrow (b) in Figure 2.35. CMCs were computed using equation 2.52 and the values for $-\Delta F_f^0/kT$ as depicted in figure 2.34 in an iterative manner. The results are compiled in table 2.2.

Figure 2.36 shows the influence of copolymer chain lengths on the CMC. Results from the present MC simulations are compared to experimental data for pluronics in aqueous medium, where the hydrophilic block consists of polyoxyethylene (E) and the hydrophic block of either polyoxypropylene (P), polyoxybutylene (B) or polyethylene (C = CH_2). Data are taken from [80] for $E_x P_y$ and from [81] for $E_x B_y$ and $E_x C_y$ and given for constant temperatures. The experimental data are ordered according to the hydrophobic block length, while the hydrophilic block length is kept roughly constant for $E_x P_y$ ($x \approx 100$) and constant for $E_x C_y$ ($x = 8$). The inset in Figure 2.36 shows computed values from the Nagarajan/Ganesh model [82] for constant hydrophilic block length, constant hydrophilic/hydrophobic ratio and constant hydrophobic block length (where the data are ordered according to their hydrophilic block length). The latter data show a rather small influence of the hydrophilic block length, what was also observed experimentally [80].
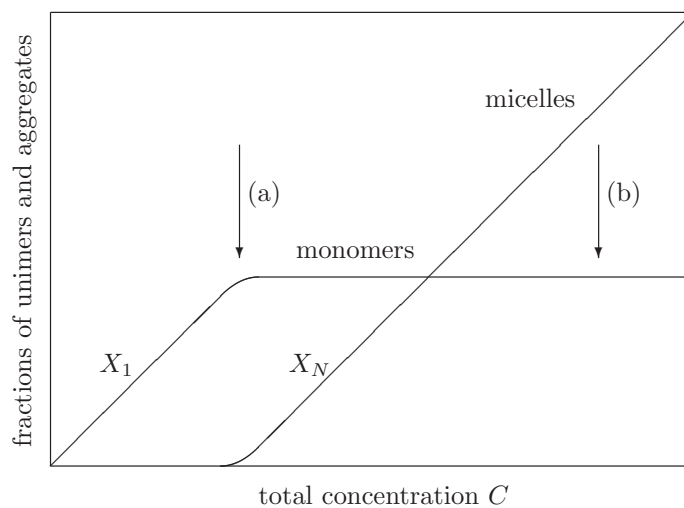
Figure 2.35: Schematic picture of the behavior of the mole fractions of unimers X_1 and aggregates X_N with increasing total concentration C (following [71]).

Table 2.2: Estimated CMC values for different total chain lengths.

N	CMC $\times 10^4$
30	1880.0
40	785.0
50	328.0
60	144.0
70	65.6
80	30.2
90	14.6
100	7.18
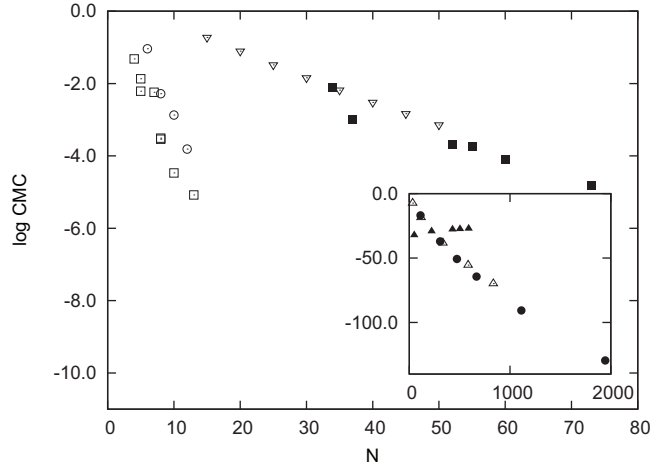
Figure 2.36: Influence of chain lengths on the CMC: ($\bigtriangledown$) this work, results for $N_A = N_B = 15, 20, 25, \ldots, 50$ and experimental results for ($\blacksquare$) $E_{100}P_N$ at 30°C, ($\circ$) E_8C_N at 25°C and ($\square$) E_xB_N at 25°C. The inset shows results for the Nagarajan/Ganesh model: ($\bullet$) $E_{429}P_N$, ($\triangle$) $E_{2.1N}P_N$ and ($\blacktriangle$) E_NP_{208}.

Table 2.3: Polymer total concentrations C for constant $m/V \sim C*N = 15$ and comparison to CMCs. The last two columns are the number and weight averages of aggregation numbers.

N	C	$C/$CMC	$\bar{N}_{\text{n,agg}}$	$\bar{N}_{\text{w,agg}}$
30	0.500	2.66	7.6	11.6
40	0.375	4.78	9.9	12.6
50	0.300	9.15	11.0	12.5
60	0.250	17.4	11.4	12.6
70	0.214	32.6	11.4	12.9
80	0.188	62.3	11.3	11.9
90	0.167	114.0	11.0	11.4
100	0.150	209.0	10.8	11.1

Cluster Weights in Solution

Figure 2.34 shows the gain in free energy when a unimer chain is transferred into a micelle. But what micelle sizes do occur in a solution of the diblock copolymer? This information can be extracted from the data $-\Delta F_f^0/kT$, depicted in Figure 2.34, and using expression 2.50. To mimic a typical experimental setting, a constant m/V, i.e. polymer mass per solution volume, well above the CMC was assumed. This values for C (see Table 2.3) were taken as starting values for X_1, and the set of equations for all cluster sizes f solved iteratively. The results, normalized for better comparison, are shown in Figure 2.37. In Table 2.3 values for the number and weight averages of micelle sizes are also given, where the latter corresponds to results of SAXS measurements. The aggregation numbers of micelles stay almost constant while changing the chain length of the diblock copolymer from 30 to 100 effective monomers.

This finding stays in contrast to theoretical considerations which usually
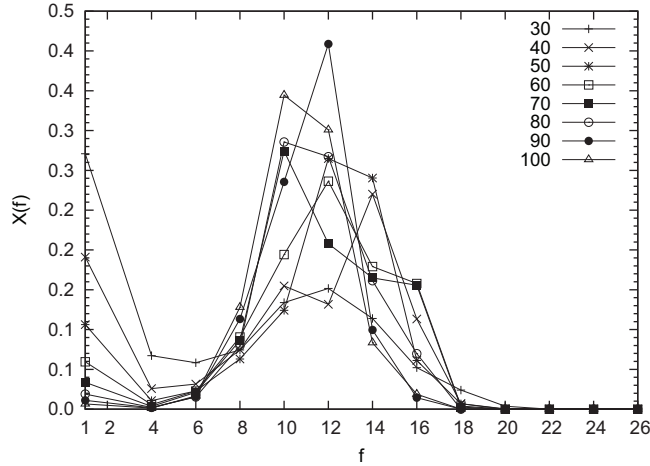
Figure 2.37: Cluster weights $X(f)$ according to their aggregation number f for a constant $C*N = 15$. All profiles are normalized to 1.

predict some dependence on the chain length of the core blocks: Zhulina and Birshtein [78] and Halperin [79] employ a Daoud–Cotton like model [58] and find $f \sim N_{\text{core}}^{4/5}$ for the limit of long corona chains (small core limit) and $f \sim N_{\text{core}}$ for the large core limit, when $N_{\text{core}} > N_{\text{corona}}$. Zhulina and Birshtein define the small core limit as $N_{\text{corona}} > N_{\text{core}}^{(1+2\nu)/5\nu} \approx N_{\text{core}}^{0.74}$ and have another intermediate region, where $f \sim N_{\text{core}}^2 N_{\text{corona}}^{-6\nu/(1+2\nu)} \approx N_{\text{core}}^2 N_{\text{corona}}^{-1.62}$, which is valid when $N_{\text{core}}^{(1+2\nu)/5\nu} > N_{\text{corona}} > N_{\text{core}}^{(1+2\nu)/6\nu}$. Nagarajan and Ganesh [82] derive another model which involves effective parameters according to the macromolecular compound and solvent under investigation and obtain e.g. for polyoxyethylene-polyoxypropylene (PEO-b-PPO) copolymers in water which is a good solvent for the corona PEO chains $f \sim N_{\text{core}}^{1.19} N_{\text{corona}}^{-0.51}$. Hence the latter two sources do also see a substantial influence of the corona chain length, which counterbalances to some extent the effect of the core chains.

This corona chain effect is also seen experimentally for PEO–PBO pluronics [80], when the hydrophilic lock lengths are kept constant. A few experimental data are compiled in Figure 2.38. Amongst PEO–PPO and PEO–PBO from [80] there are also data from Stubenrauch [75] for symmetric diblocks with $N_{\text{core}} \approx N_{\text{corona}} = N_X$, for which one finds roughly $f \sim N_X^{0.53}$.

It is assumed for the presented results that, concerning the relatively short corona chains which feel an idealized solvent, their effect on the association number is larger than in the above cases. Recall that the scaling exponent of the free energy change per chain in a brush tethered to a small sphere or to a planar surface was also found to be larger than in the conventional theories. Furthermore the interaction of core chains and hence their effect on the association number is underestimated by PERM, as the density in the core is lower than one, see below. The strongly swollen corona chains and the underestimation of the core influence result apparently in a cancellation of the two scaling factors to a large extent.
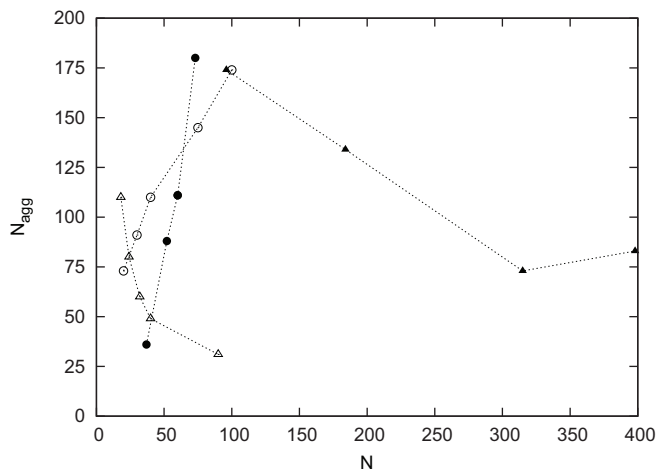
Figure 2.38: Some experimental data for association numbers N_{agg}: ($\circ$) symmetric block copolymer of *endo,exo*[2.2.1]bicyclo-2-ene-5,6-dicarboxylic acid and its dimethylester with $N \approx N_{\text{core}} \approx N_{\text{corona}}$ [75], ($\bullet$) $\mathrm{E}_{98-104}\mathrm{P}_N$, ($\triangle$) $\mathrm{E}_N\mathrm{B}_{10}$ and ($\blacktriangle$) $\mathrm{E}_N\mathrm{B}_{17-19}$ from [80].

Geometrical Features and Comparison with Scaling Theories

A check of the ability of the described method to sample successfully copolymer micelles with the expected core–shell structure is done by computing the radial probability distributions for core and corona monomers, as shown in Figure 2.39. The probabilities to find core (A) and corona (B) monomers at radius r from the center-of-mass are given for a typical micelle containing 12 chains with $N_A = N_B = 50$. As all observables in PERM, the results are obtained as an average weighted by the chain weights for the considered conformations. Additionally a (weighted) average was drawn from an ensemble of 20 runs, from which also the error bars are deduced. The distributions show, that micelles with the expected structure are indeed constructed and core and corona monomers are well separated.

Radial monomer density profiles are shown in Figure 2.40 for micelles of $f = 4, 6, 8, 10, \ldots, 24$ chains. The assumed dense core with $\phi(r) = 1$ in the Daoud–Cotton model [58] is not fully reached, in particular for small f. The maximum density in the core region is rather about 0.9. This deviation seems to be caused by the approach of growing chains from an outer shell inwards. Constructing an SAW at melt densities on the sc lattice is very inefficient and yields only a small number of configurations. The modification of the PERM algorithm—biasing new monomer positions towards regions with more free neighbors for the next step, see Section 2.4—enhanced the performance somewhat. As can be seen from the MMC runs with reptation moves above, the connecting monomers are slightly shifted to smaller radii, i.e. the core becomes denser when equilibrated by dynamical MC.

To study the decay of the profile, a double logarithmic plot with scaled densities is shown in Figure 2.41, in the same way as in the case of chains tethered to a small sphere. One can see that, after a roughly constant region at small r, the density decays quickly without exhibiting a determined scaling behavior
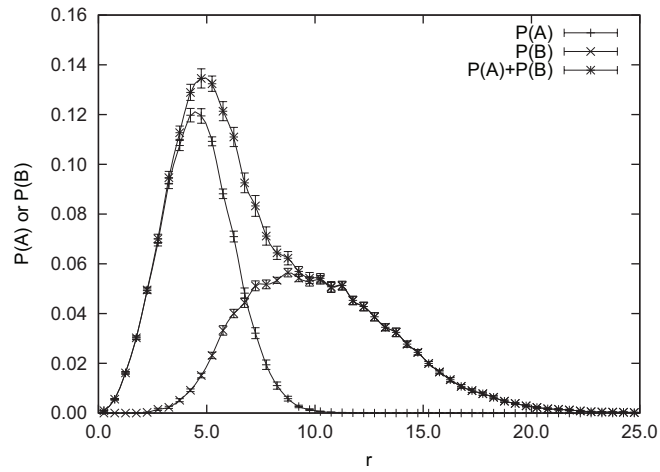
Figure 2.39: Radial probability distributions for core (A) and corona (B) monomers, $P(A)$ and $P(B)$, for a copolymer micelle of 12 chains with $N_A = N_B = 50$, and the sum of the two.
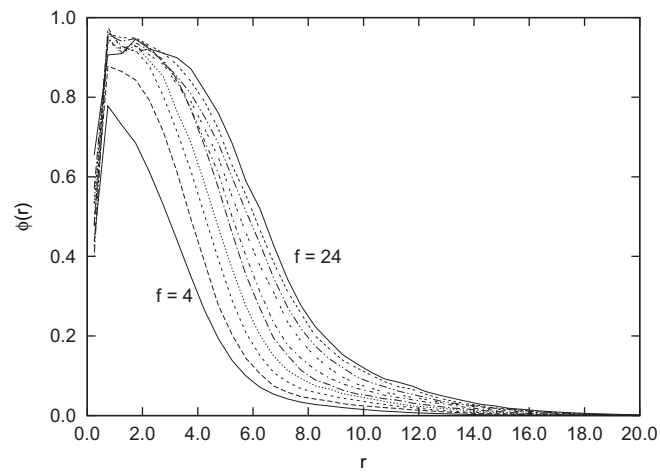
Figure 2.40: Radial density profiles of micelles with aggregation number $f = 4, 6, 8, \ldots, 24$.
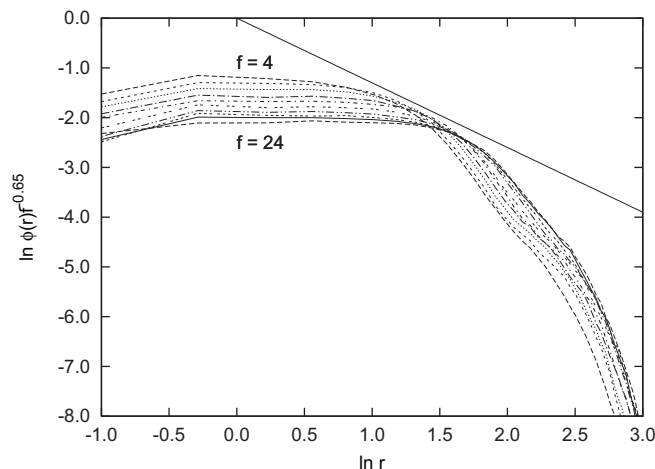
Figure 2.41: Double logarithmic plot of radial density profiles scaled by $f^{0.65}$ of micelles with aggregation number $f = 4, 6, 8, \ldots, 24$. The straight line has slope of -1.30.

$\sim r^{-\alpha}$. In particular the expected scaling law for the swollen corona of $r^{-1.30}$ is not found (straight line in Figure 2.41). This behavior of micelles of symmetric block copolymers with relatively short chain lengths was also found for e.g. polystyrene–polyisoprene in decane by SANS measurements and MC simulations [73] and for micelles of copolymers made from norbornene derivatives[11] via ring-opening metathesis polymerization (ROMP) by SAXS measurements [74, 75], which allowed the synthesis of relatively well defined chain lengths. A double logarithmic plot for data from the latter source is also shown in Figure 2.42 for symmetric block copolymers of different chains lengths. The block lenghts of 100–100, 75–75, 40–40, 30–30 and 20–20 are "theoretical", i.e. according to experimental parameters in synthesis. The effective ratio of lyophobic/lyphilic block by integration of the ^{1}H NMR signal are 1.0, 0.9, 1.0, 1.1 and 1.2 and the PDI are 1.13, 1.16, 1.08, 1.10 and 1.07 for the above series.

The decay of the density in Figure 2.41 sets in at larger radii the higher the aggregation number f is. This is consistent with simple geometric considerations, as the core radius increases with f (see below). Figure 2.41 shows furthermore a weak "shoulder" in the profile decay at larger radii. This shoulder was also observed experimentally, see Figure 2.42, and is associated with the separation of core and corona monomers in the copolymer micelle.

The values for the radius of gyration of the micellar cores, more specifically $\langle (R_g^{\text{core}})^2 \rangle^{1/2}$, are compiled in Figure 2.43. The error bars stem from an ensemble of 20 or 30 runs, depending on the system size. Although long runs were carried out and averages of several runs were taken, one still observes a significant statistical scattering amongst the data. Neveretheless I present a simple analysis in the form of a scaled plot, Figure 2.44. Assuming that the core monomers of f chains form a dense sphere of radius r_{core}, one puts

$$\frac{4\pi r_{\text{core}}^3}{3} = \frac{1}{2} N f \tag{2.53}$$

---

[11]To be more specific, copolymers with *endo,exo*[2.2.1]bicyclo-2-ene-5,6-dicarboxylic acid and its dimethylester as their building blocks, whose structures are given in Figure 2.1.
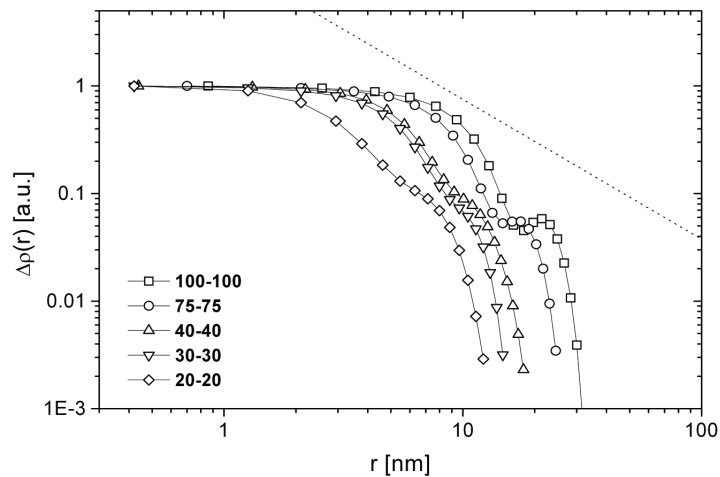
Figure 2.42: Radial density profiles from SAXS for symmetric block copolymers with block lengths of 100–100, 75–75, 40–40, 30–30 and 20–20, see text. The dotted line represents a scaling of $\sim r^{-4/3}$. Graph produced using data from [74, 75].
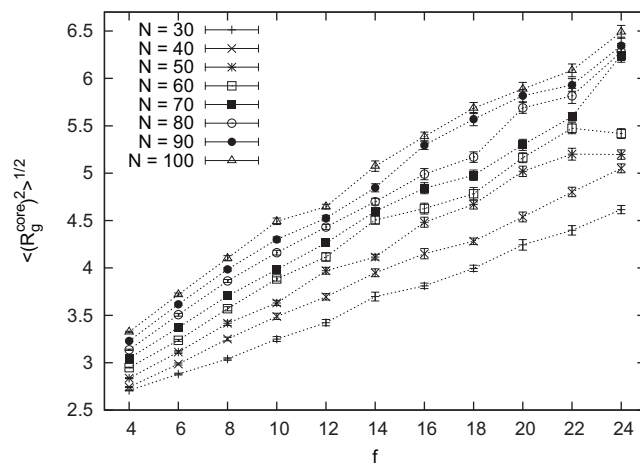
Figure 2.43: Radii of gyration of the A monomer cores of A–B block copolymer micelles consisting of $f = 4, 6, 8, \ldots, 24$ chains of $N = 30, 40, 50, \ldots, 100$ monomers.
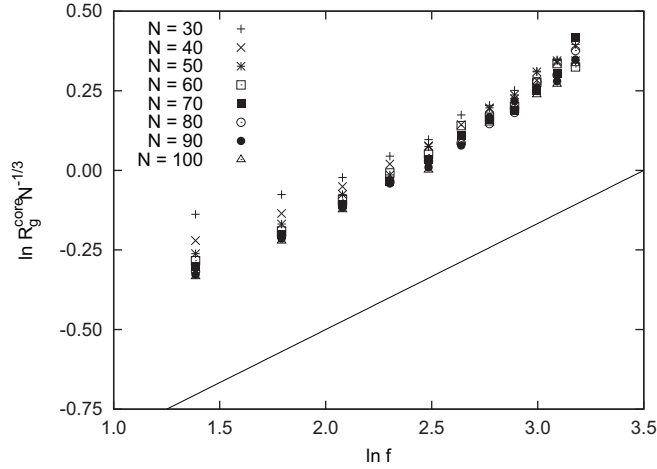
Figure 2.44: Radii of gyration of micelle cores scaled by $N^{1/3}$ in a double logarithmic plot. The straight line represents values for a solid sphere of density 1.0.

then

$$\ln r N^{-1/3} = \frac{1}{3} \ln f + C \qquad (2.54)$$

where the core chain length is assumed to be $N_A = N/2$. The straight line in Figure 2.44 refers to this solid sphere, for which the constant becomes $C = \ln(3/8\pi)^{1/3} + \ln(2/5)^{1/2}$, where the relationship $r = \sqrt{5/2}R_g$ is used. The results for R_g^{core} follow indeed roughly the expected scaling, albeit offset by a relatively constant value. This offset is caused by the core density lower than 1 and the rough surface, both connected to larger R_g-values. A closer look reveals that there are deviations from the slope of $1/3$ to flatter curves for micelles of few short chains and to steeper curves for the ones consisting of many chains of any length. The former effect is dedicated to deviations from the spherical shape for small cores[12], while the latter deviations are likely to be an artefact of the algorithm, which fails to construct large dense regions by growing chains stepwise as described.

In Figure 2.45 the raw data for radii of gyration of whole micelles $\langle (R_g^{\text{mic}})^2 \rangle^{1/2}$ are given, and Figure 2.46 shows double logarithmic plots of the radii of gyration and the distance vectors between the starting monomers (to which the corona chains are connected) and the free ends in the corona, both scaled by $\langle R_{g,1}^2 \rangle$ of a single chain of the same length like a corona chain. The expected scaling behavior $R_g \sim f^{0.41}$ (solid line) for the radii of gyration is reached, in particular for longer chains and larger aggregates. Note that all monomers, inclusively the core, are considered for the computation of $\langle (R_g^{\text{mic}})^2 \rangle^{1/2}$. Interestingly the end-to-end distance of corona chains stays almost constant over the range of f in the diagram (which covers most of the micelles that are expected to occur due to their free energy). This stays in relation to the case of chains tethered to a rigid sphere above, where an onset of the expected scaling was seen for

_____

[12]Recall that the surface roughness of the core sphere is given as an input to the runs. Although all data refer to starting points at radii which gave the minima in free energy, this might cause an additional error which is more pronounced for small cores.
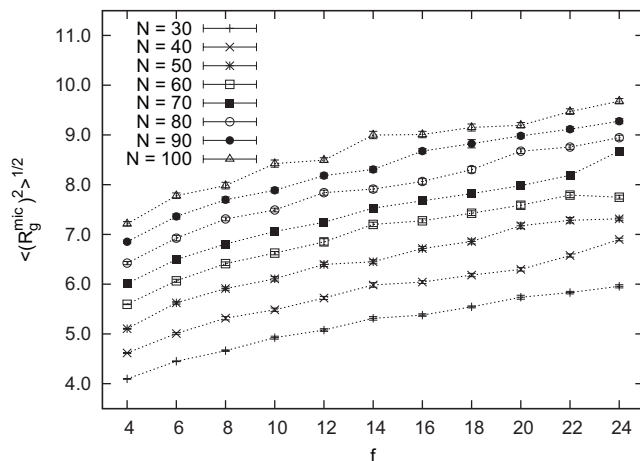
Figure 2.45: Radii of gyration whole A–B block copolymer micelles consisting of $f = 4, 6, 8, \ldots, 24$ chains of $N = 30, 40, 50, \ldots, 100$ monomers.
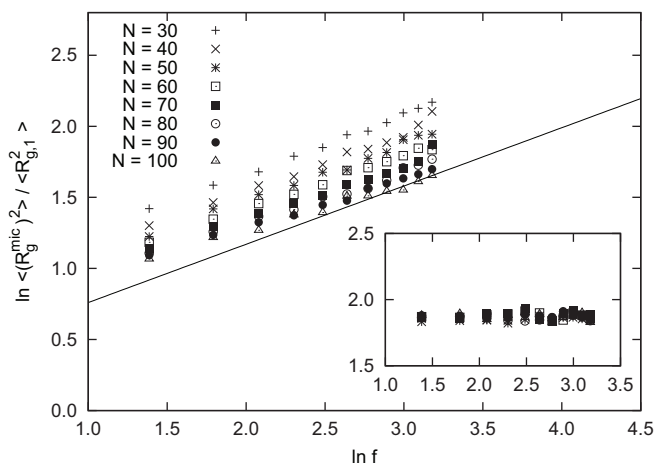
Figure 2.46: Radii of gyration $\langle (R_g^{\mathrm{mic}})^2 \rangle$ of whole A–B block copolymer micelles (main graph) and end-to-end distances of corona chains $\langle (R_{se}^{\mathrm{mic}})^2 \rangle$ (inset), scaled by $\langle R_{g,1}^2 \rangle$ of a single chain in a double logarithmic plot. Micelles consist of $f = 4, 6, 8, \ldots, 24$ chains of $N = 30, 40, 50, \ldots, 100$ monomers.

Table 2.4: Weight average values for R_g for cores and whole micelles and R_h obtained from the individual radii and cluster weights.

N	$\bar{R}_{g,\text{core}}$	$\bar{R}_{g,\text{mic}}$	$\bar{R}_{h,\text{mic}}$
30	3.45	5.07	10.09
40	3.80	5.80	11.42
50	4.00	6.38	12.37
60	4.23	6.95	13.31
70	4.33	7.31	13.90
80	4.41	7.74	14.51
90	4.47	8.08	14.99
100	4.60	8.48	15.56
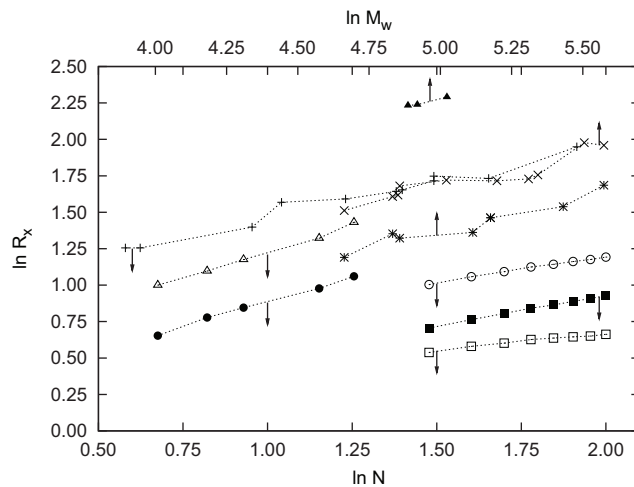
Figure 2.47: Comparison of micellar radii from different sources: ($\square$) $R_{g,\text{core}}$ ($\blacksquare$) $R_{g,\text{mic}}$ and ($\circ$) $R_{h,\text{mic}}$ from this work (+) $R_{g,\text{core}}$ of polystyrene-b-poly(cesium acrylate) in toluene by SAXS [85], $R_{h,\text{mic}}$ of polystyrene-b-polybutadiene in ($*$) DMF and ($\times$) n-heptane by DLS [84], ($\triangle$) $R_{g,\text{mic}}$ and ($\bullet$) $R_{g,\text{core}}$ by SAXS from Stubenrauch et al. [75] and ($\blacktriangle$) $R_{g,\text{mic}}$ of polystyrene-b-polybutadiene in heptane by SAXS [83].

$f = 32$. Obviously the radial scattering of connection points to the core chains introduces further degrees of freedom, so that chain stretching is avoided.

It is noteworthy that the experimental scaling behavior of R_g or R_h with the chain length N, which is accessible experimentally by SAXS and DLS, exhibits slightly higher exponents. In those cases a weighted average over a range of micelle sizes is measured—which is a different situation than for the constant f results above. A comparison of micellar radii from different sources is shown in Figure 2.47. Their scaling behavior is summarized in Table 2.5, from which it becomes obvious that the apparent scaling exponent found with the MC simulations is to small. This underestimation is introduced predominantly by the association numbers, which do not scale with N as in the experiments. The deviations are most significant for $R_{g,\text{core}}$, whereas $R_{g,\text{mic}}$ and $R_{h,\text{mic}}$ exhibit nonetheless a scaling close to experiments.

Table 2.5: Comparison of the scaling behavior of micellar radii from this work with experiments.

source	scaling	building blocks	technique
this work	$R_{g,\text{core}} \sim N^{0.23} \sim N^{0.23}_{\text{core}}$		
this work	$R_{g,\text{mic}} \sim N^{0.42}$		
this work	$R_{h,\text{core}} \sim N^{0.35}$		
Bluhm et al. [83]	$R_{g,\text{mic}} \sim N^{0.44}$	polystyrene-b-polybutadiene in n-heptane	SAXS
Oranli et al. [84]	$R_{h,\text{mic}} \sim N^{0.47}$	polystyrene-b-polybutydiene in DMF	DLS
Oranli et al. [84]	$R_{h,\text{mic}} \sim N^{0.43}$	polystyrene-b-polybutydiene in n-heptane	DLS
Nguyen et al. [85]	$R_{g,\text{core}} \sim N^{0.51}_{\text{core}}$	polystyrene-b-poly(cesium acrylate) in toluene	SAXS
Stubenrauch et al. [75]	$R_{g,\text{core}} \sim N^{0.57} \sim N^{0.57}_{\text{core}}$	ROMP polymerized $endo,exo$[2.2.1]bicyclo-2-ene-5,6-dicarboxylic acid and dimethylester in ethanole	SAXS
Stubenrauch et al. [75]	$R_{g,\text{mic}} \sim N^{0.61}$	ROMP polymerized $endo,exo$[2.2.1]bicyclo-2-ene-5,6-dicarboxylic acid and dimethylester in ethanole	SAXS

2.3 Conclusions

The PERM algorithm was applied to a structureless polymer model with effective interactions on the simple cubic lattice for various systems: a single SAW chain, a semi-dilute solution in good solvent, a single chain end-tethered to a planar inert surface, a polymer brush exposed to a good solvent, SAW chains grafted to a small sphere and micelles built of symmetric diblock copolymers. For the single chain systems, literature values could be reproduced with excellent agreement. Although this work was not intended on high-precision calibration data, the precision of the results is satisfactory. The first "new" system for the algorithm that was studied here is the many-chain system in the semi-dilute regime. The approach yielded results for the free energy/osmotic pressure of such solutions in good agreement with des Cloizeaux's rule and experimental data. This amounts to a validation of PERM for interacting chains in a good solvent, which plays an important role not only for the uniform semi-dilute solution, but also for the other systems studied here. The scaling with N was not reached for the end-to-end distance R_{ee} of the chains. An effect that is likely to be caused by the relatively short chain lengths—and also a general finding of this work: the radii were not always obtained to be scaling as expected, due to too short chains, and the statistical quality of their estimates not always satisfactory. In particular this was found for R_{ee}; the radius of gyration R_g was less scattered, as expected for a figure obtained from a larger number of data (all monomer positions). Polymer brushes with planar symmetry pose generally a challenge to static MC schemes as a relatively large portion of the space has to be crowded by stretched chains. The yield of successful configurations of the algorithm was hence poor and the range of grafting densities and chain lengths was limited. Furthermore the simple, yet unflexible ansatz on the sc lattice may have caused an additional deterioration. Hence the regime where the expected scaling should be valid could not be fully reached and the profiles and distributions of free end monomers where somewhat deviating from the long flexible chain limits. The behavior of the surface osmotic pressure is subject to diverging results from different approaches in literature. Carignano and Szleifer developed a single-chain mean-field approach and use several chain models over a broader range of grafting densities, what puts the differing data on a common ground. More recently, Ohno used an enrichment algorithm on the sc lattice. The results obtained here are in agreement with this latter work and fit also into the work of Carignano and Szleifer.

The situation is more favorable in spherical symmetry when chains are end-tethered to a curved surface as the density decays rapidly with r. Although, to my knowledge, there are no data in literature for the partition sums which allow a direct comparison, the general properties of the results are conform to the broad spectrum of studies of star polymers. This is also true for geometric observables, where with increasing chain lengths and numbers the two cases converege. The simple theory involving the cone approximation was not found to be valid for the chain lengths studied. But this finding is in accordance with MC simulations done by other authors.

The polymer brush in spherical symmetry was used as a test case for the sampling of micelles consisting of many symmetric block copolymer chains. This task is particularly difficult to achieve with other simulation techniques. It could be demonstrated that, given some preliminary assumptions which were checked

to be valid lateron, spherical micelles could be successfully constructed. Several observables, micellar radii, density profiles and monomer distributions, agreed reasonably with their expected properties, derived from models based on star polymers. One important feature where the results of this work disagree with the established models and experimental measurements is the scaling of association numbers with chain lengths. This is ascribed to both, the steeper dependence of the conformational free energy of corona chains on the number of chains found also by other authors, as well as the shortcoming of the present approach in describing the dense core of the micelles. This shortcoming is assumed to stem from the sc lattice that makes it difficult for the algorithm to fill all sites of the lattice with chains. Finally micellar radii for equilibated solutions were also computed, which agree surprisingly well with experimental data, regarding the deviating prediciton of cluster weights in equilibrium.

Suggestions for Further Work

A natural suggestion for further work is the test of more sophisticated lattices, e.g. the bond fluctuation model for the simulation of micelles. It is assumed that, as it allows for more flexible chains, the micellar core could be better sampled. But these models also introduce more degrees of freedom and the sampling of the larger phase space becomes more difficult.

In general the ansatz can be used to study the influence of several parameters of the system: e.g. relative block lengths and other architectures or temperature effects. Further computations on geometric features would also allow for more comparisons with experiments and hence a further validation of the method.

2.4 Pseudocodes

The Basic PERM Step

The pseudocode for PERM was taken from [4] and slightly modified to reflect the necessary steps for growing several chains simultaneously.

```
1 subroutine step(x, n, k)
      choose x′ next to x with equal probability p = 1/mₙ
      if there is no free site return
      wₙ = mₙ exp(−E(x′)/k_B T)
5     Wₙ = Wₙ₋₁wₙζ
      Zₙ = Zₙ + Wₙ
      measure R_ee, R_g,...
      if n < N_max and Wₙ > 0
          W> = c> Zₙ/Z₁
10        W< = c< Zₙ/Z₁
          if Wₙ > W>
              Wₙ = Wₙ/2
              call step(x′, n + 1, (k mod f) + 1)
              call step(x′, n + 1, (k mod f) + 1)
15        else if Wₙ < W<
              Wₙ = 2Wₙ
              compute random number ξ ∈ [0, 1]
              if ξ < 1/2
                  call step(x′, n + 1, (k mod f) + 1)
20            else
                  return
              endif
          endif
              call step(x′, n + 1, (k mod f) + 1)
25        endif
      endif
27 end
```

Notes:

There are f single unimers in the system treated simulaneously ($k = 1 \ldots f$), which consist of a total of n monomers. The next subroutine call adds the next monomer $n + 1$ to the next chain $(k \bmod f) + 1$. Furthermore the A and B branches of the unimers are grown alternately.

For better computational efficiency the coordinates $\mathbf{x}$ where stored twice: once in a three dimensional lattice array to quickly check neighbor sites, secondly in a two dimensional chain array $(n, \{x, y, z\})$ to quickly scan configurations for measurements.

The properly chosen factor ζ in line 5 prevents over- or underflow for variables W_n and Z_n. Results were subsequently corrected for ζ.

There are m_n free next neighbor sites to $\mathbf{x}$ (line 2).

In the case of *importance sampling* the weights w_n become $\sum_{i=1}^{m_n} \exp(-E(\mathbf{x}'_i)/k_B T)$ and new monomer positions are chosen *non-uniformly*, see below.

Finding New Monomer Positions - *"Simple Sampling"*

A new monomer position $\mathbf{x}'$ is chosen uniformly out of m_n free neighbors.

```
1 subroutine newpos(x)
      d = (0,0,0);  m = 0
      do i = 1,...,3
         d_i = -1
5        if lattice(x + d) = 0
            m = m + 1
            k(m) = x + d
         endif
         d_i = +1
10       if lattice(x + d) = 0
            m = m + 1
            k(m) = x + d
         endif
         d_i = 0
15    enddo
      if m = 0 return
      compute random number ξ ∈ [0, 1]
      j = integer(mξ) + 1
      x' = k(j)
20 end
```

Finding New Monomer Positions - *"Importance Sampling"*

New monomer positions are chosen according to their potential thermal inter-action. The probability to choose the jth site out of m_n free neighbors at $\mathbf{x}'$ is

$$p_j = \frac{\exp(-E(\mathbf{x}'_j)/k_B T)}{\sum_{i=1}^{m_n} \exp(-E(\mathbf{x}'_i)/k_B T)} \tag{2.55}$$

```
1 subroutine newpos(x)
      d = (0,0,0);  m = 0
      do i = 1,...,3
         d_i = -1
5        if lattice(x + d) = 0
            m = m + 1
            k(m) = x + d
            w(m) = w(m - 1) + exp(-E(k(m))/k_B T)
         endif
10       d_i = +1
         if lattice(x + d) = 0
            m = m + 1
            k(m) = x + d
            w(m) = w(m - 1) + exp(-E(k(m))/k_B T)
15       endif
         d_i = 0
      enddo
      if m = 0 return
```

```
        if biasing is done
  20        do i = 1,...,m
                if we put core monomer and r(k(i)) < r(x)
                    w(i) = w(i) (2(n-1)+3)/(2(n-1)+1)
                if we put core monomer and r(k(i)) > r(x)
                    w(i) = w(i) (2(n-1)+1)/(2(n-1)+3)
  25            if we put corona monomer and r(k(i)) < r(x)
                    w(i) = w(i) (2(n-1)+1)/(2(n-1)+3)
                if we put corona monomer and r(k(i)) > r(x)
                    w(i) = w(i) (2(n-1)+3)/(2(n-1)+1)
                if we put core monomer and r(k(i)) < r⊙
  30                w(i) = w(i)m(k(i))
            enddo
        endif
        compute random number ξ ∈ [0,1]
        ξ = w(m)ξ
  35    j = 1
        do while (w(j) < ξ)
            j = j + 1
        enddo
        x' = k(j)
  40 end
```

Notes:

The Boltzmann factors $\exp(\frac{-E(\mathbf{k}(m))}{k_B T})$ in lines 8 and 14 are determined in a similar way as determining free neighbors, looping a vector $\mathbf{d}$ over all neighbors of the potential new site and summing up thermal interactions.

The grey text (lines 19–32) refers to a bias, that favors core positions for core monomers and outer positions for corona monomers. r means the distance between the monomer position and center of the micelle (*i.e.* the origin around which the micelle is constructed). The factor was chosen to be $b = \frac{2(n-1)+3}{2(n-1)+1}$ and b^{-1}, respectively. With n being the number of core/corona monomers in the unimer chain.

In addition, core monomer positions $\mathbf{k}(i)$ are favored when the future position has more free sites $m(\mathbf{k}(i))$ around it (lines 29–30). This is done only inside a chosen core radius $r^{\odot}$.

In case this biasing is done, the monomer weight w_n in the basic PERM step has to be adjusted accordingly (see above).

Random Number Generator

The Fortran code for the long period random number generator of L'Ecuyer with Bays-Durham shuffle was taken from [26] and modified to take the computer's system time as seed.

```
  1 subroutine ran2(ξ)
        parameter m₁ = 2147483563; a₁ = 40014; q₁ = 53668; r₁ = 12211
        parameter m₂ = 2147483399; a₂ = 40692; q₂ = 52774; r₂ = 3791
        if first call
```

```
5        i_1 = time()
         do  j = N_tab + 8, ... , 1
             k = integer(i_1/q_1)
             i_1 = a_1(i_1 - kq_1) - kr_1
             if  i_1 < 0  then  i_1 = i_1 + m_1
10           if  j ≤ N_tab  then  i_v(j) = i_1
         enddo
         i_y = i_v(1)
     endif
     k = integer(i_1/q_1)
15   i_1 = a_1(i_1 - kq_1) - kr_1
     if  i_1 < 0  then  i_1 = i_1 + m_1
     k = integer(i_2/q_2)
     i_2 = a_2(i_2 - kq_2) - kr_2
     if  i_2 < 0  then  i_2 = i_2 + m_2
20   j = 1 + i_y / (1+(m_1-1)/N_tab)
     i_y = i_v(j) - i_2
     i_v(j) = i_1
     if  i_y < 1  then  i_y = i_y + m_1 - 1
     ξ = min ( i_y/m_1 , 1 - ε )
25 end
```

Notes:

The routine produces two sequences of random numbers i_1 (lines 14–16) and i_2 (lines 17—19) based on two sets of parameters m_1, a_1, q_1, r_1 and m_2, a_2, q_2, r_2, using Schrage's method.

i_1 is shuffled using an array $i_v(j)$ of size N_{tab}. The element is chosen using random number i_y (saved from previous call) by $j = 1 + \frac{i_y}{1+(m_1-1)/N_{tab}} \in [1, N_{tab}]$.

The two random number sequences are combined in line 21, divided by m_1 to produce a real number $\in [0,1]$. A maximum value 1 is replaced by $1 - \epsilon$, with ϵ being some small constant properly chosen.

Distributing Starting Monomers on a Spherical Surface

The following routine distributes points on a given spherical surface. This surface consists of lattice sites within a radius R_s from an origin (assumed to be $(0, 0, 0)$), occupied with monomers of value -1. The points are corrected to have not less than 1 and not more than 4 adjacent surface monomers.

```
1 subroutine startpts(f,  R_s)
      compute random numbers ξ_1 ... ξ_3
      r = √(ξ_1² + ξ_2² + ξ_3²)
      x_1^(r) = ξ_1 R_s/r; same for x_2^(r), x_3^(r)
5     x_1 = integer(sign((abs(x_1^(r)) + 0.5), x_1^(r))); same for x_2, x_3
      d = (0, 0, 0);  m = 0
      do  i = 1, ... , 3
          d_i = -1
          if lattice(x + d) = -1
```

```
10          m = m + 1
            k(m) = x + d
         endif
         d_i = +1
         if lattice(x + d) = −1
15          m = m + 1
            k(m) = x + d
         endif
         d_i = 0
      enddo
20    if  m = 0
         if  |x_1| > |x_2|, |x_3|
            x_1 = x_1 − sign(1, x_1)
         elseif  |x_2| > |x_1|, |x_3|
            x_2 = x_2 − sign(1, x_2)
25       else
            x_3 = x_3 − sign(1, x_3)
         endif
      elseif  m > 4
         if  |x_1| > |x_2|, |x_3|
30          x_1 = x_1 + sign(1, x_1)
         elseif  |x_2| > |x_1|, |x_3|
            x_2 = x_2 + sign(1, x_2)
         else
            x_3 = x_3 + sign(1, x_3)
35       endif
      endif
      do  (i > j) = 1, …, f
         if  x_1(i) = x_1(j) and x_2(i) = x_2(j) and x_3(i) = x_3(j)
            start again
      enddo
41 end
```

Notes:

In line 4 real coordinates are computed, these are rounded to the next integer lattice site in line 5. The function `sign(arg1,arg2)` returns `arg1` with the sign of `arg2`.

After checking for adjacent surface monomers (lines 6–19), the points are moved towards smaller radii, when there is no surface neighbor (lines 20–27), and to larger radii, when there are more than 4 (lines 28–36). This is done by altering the component with the largest contribution to the distance from origin.

Finally, the points are checked not to lie on top of each other (lines 37–40).

Dynamical Monte Carlo using Reptation Moves

```
1 subroutine dynamo({conformations})
      do  i = 1, …, N_{max}
         call energy_one(x_i, E_i)
         E = E + E_i
```

```
 5    enddo
      E = E/2
      do i = 1,...,loops
          compute random number ξ ∈ [0, 1]
          choose chain and chain end at random
10        call energy_one(x_ω, E_del)
          call energy_one(x_c, E_flip1)
          call newpos(x_α)
          clear monomer at x_ω
          flip monomer type at x_c
15        call energy_one(x'_α, E_put)
          call energy_one(x_c, E_flip2)
          ΔE = E_put − E_del − E_flip1 + E_flip2
          accept = .false.
          if ΔE < 0
20            accept = .true.
          else
              w = e^{−ΔE/k_B T}
              compute random number ξ ∈ [0, 1]
              if ξ < w then accept = .true.
25        endif
          if (accept)
              E = E + ΔE
              update conformation
          else
30            discard changes to conformation
          endif
        do measurements and statistics
        enddo
34 end
```

Notes:

A reptation move of an A–B block copolymer chain consists of adding a monomer of the same type at the chain head $\mathbf{x}_\alpha$, deleting one at the chain tail $\mathbf{x}_\omega$ and flipping one monomer type in the center of the chain $\mathbf{x}_c$.

Routine newpos, which is called in line 12, chooses a free neighbor site with equal probability (as in the "simple sampling" case above).

If a move is not accepted or no free neighbor site is found to put the new monomer, the original conformation is preserved (jump from line 12 to 32 in the latter case).

The routine energy_one sums up interaction energies with next neighbors according to monomer types, in a manner similar to routine newpos for the "importance sampling" case above. The do-loop at lines 2–6 just computes once the total energy of whole conformations (and corrects for double counting).

Runs worked on several conformations in parallel and averaged the individual results. As in the PERM case, conformations were saved twice. Once in a chain array to quickly scan through chains, and secondly on a three dimensional lattice array. Up to 31 conformations were saved simultaneously in the latter, altering the bits of a 32-bit integer by adding $+2^j$ for an A monomer of conformation j and -2^j for a B monomer.

Bibliography

[1] K. Binder, Monte Carlo and Molecular Dynamics Simulations of Amorphous Polymers, in J. Bizerano (ed.), *Computational Modelling of Polymers*, Marcel Dekker, 1992, p. 221

[2] D. Raabe, *Computational Materials Science*, Wiley-VCH, 1998

[3] I. Geroff, A. Milchev, K. Binder and W. Paul, *J. Chem. Phys.* **98**, 6526 (1993)

[4] P. Grassberger, *Phys. Rev. E* **56**, 3682 (1997)

[5] P.-G. de Gennes, *Scaling Concepts in Polymer Physics*, Cornell University Press, 1979

[6] D. P. Landau and K. Binder, *A Guide to Monte Carlo Simulations in Statistical Physics*, 2nd ed., Cambridge University Press, 2005

[7] J. des Cloizeaux and G. Jannink, *Polymers in Solution – Their Modelling and Structure*, Clarendon Press, 1990

[8] A. Sokal, Monte Carlo Methods for the Self-Avoiding Walk, in K. Binder (ed.), *Monte Carlo and Molecular Dynamics Simulations in Polymer Science*, Oxford University Press, 1995, p. 47

[9] P. J. Flory, *Principles of Polymer Chemistry*, Cornell University Press, 1953

[10] G. Strobl, *The Physics of Polymers - Concepts for Understanding their Structures and Behavior*, Springer-Verlag, 2007

[11] S.-T. Sun, I. Nishio, G. Swislow and T. Tanaka, *J. Chem. Phys.* **73**, 5971 (1980)

[12] A. Z. Panagiotopoulos, M. A. Floriano and S. K. Kumar, *Langmuir* **18**, 2940 (2002)

[13] A. Cavallo, M. Müller and K. Binder, *Macromolecules* **39**, 9539 (2006)

[14] M. N. Rosenbluth and A. W. Rosenbluth, *J. Chem. Phys.* **23**, 356 (1955)

[15] F. T. Wall and J. J. Erpenbeck, *J. Chem. Phys.* **30**, 634 (1959)

[16] P. Grassberger, *Phys. Rev. E* **65**, 031807 (2002)

[17] H.-P. Hsu, W. Paul and K. Binder, *Europhys. Lett.* **92**, 28003 (2010)

[18] H.-P. Hsu, V. Mehra and P. Grassberger, *Phys. Rev. E* **68**, 037703 (2003)

[19] S. Bhattacharya, H.-P. Hsu, A. Milchev, V. G. Rostiashvili and T. A. Vilgis, *Macromolecules* **41**, 29203 (2008)

[20] H.-P. Hsu, W. Nadler and P. Grassberger, *Macromolecules* **37**, 4658 (2004)

[21] H.-P. Hsu, W. Paul and K. Binder, *Macromol. Theor. Simul.* **16**, 660 (2007)

[22] L. I. Klushin, A. M. Skvortsov, H.-P. Hsu and K. Binder, *Macromolecules* **41**, 5890 (2008)

[23] P. L'Ecuyer, *Comm. ACM* **31**, 742 (1988)

[24] M. Luscher, *Comp. Phys. Comm.* **79**, 100 (1994)

[25] F. James, *Comp. Phys. Comm.* **79**, 111 (1994)

[26] W. H. Press, S. A. Teutolsky, W. T. Vetterling and B. P. Falnnery, *Numerical Recipies in Fortran 77*, 2nd ed., Cambridge University Press, 1992

[27] L. Schrage, *ACM Trans. Math. Softw.* **5**, 132 (1979)

[28] P. Grassberger, P. Sutter and L. Schäfer *J. Phys. A: Math. Gen.*, **30** 7039 (1997)

[29] B. Li, N. Madras and A. D. Sokal, *J. Stat. Phys.* **80**, 661 (1995); arXiv:hep-lat/9409003v1

[30] R. Hegger and P. Grassberger, *J. Phys. A: Math. Gen.* **27**, 4069 (1994)

[31] W. Humphrey, A. Dalke and K. Schulten, *J. Mol. Graphics* **14**, 33 (1996)

[32] M. Daoud, J. P. Cotton, B. Farnoux, G. Jannink, G. Sarma, H. Benoit, R. Duplessix, C. Picot and P.-G. de Gennes, *Macromolecules* **8**, 804 (1975)

[33] K. Shida, K. Ohno, M. Kimura and Y. Kawazoe, *Comput. Theor. Polym. S.*, **10** 281 (2000)

[34] C.-C. Huang, R. G. Winkler, G. Sutmann and G. Gompper, *Macromolecules*, **43** 10107 (2010)

[35] A. Pelissetto, *J. Chem. Phys.*, **129** 044901 (2008)

[36] I. Noda, N. Kato, T. Kitano and M. Nagasawa, *Macromolecules* **14**, 668 (1981)

[37] P. Grassberger, *J. Phys. A: Math. Gen.* **38**, 323 (2005)

[38] H. W. Diehl and M. Shpot, *Nucl. Phys. B* **528**, 595 (1998)

[39] T. D. Hahn and J. Kovac, *Macromolecules* **23**, 5153 (1990)

[40] G. S. Grest and M. Murat, Computer Simulations of Tethered Chains, in K. Binder (ed.), *Monte Carlo and Molecular Dynamics Simulations in Polymer Science*, Oxford University Press, 1995, p. 476

[41] G. S. Grest, *Macromolecules* **27**, 418 (1994)

[42] E. Raphaël, P. Pincus, G. H. Frederickson, *Macromolecules* **26**, 1996 (1993)

[43] B. J. Factor, L.-T. Lee, M. S. Kent and F. Rondelez, *Phys. Rev. E* **48**, R2354 (1993)

[44] A. Chakrabarti and R. Toral, *Macromolecules* **23**, 2016 (1990)

[45] P.-Y. Lai and K. Binder, *J. Chem. Phys.* **95**, 9288 (1991)

[46] S. T. Milner, *J. Chem. Soc. Faraday Trans.* **86**, 1349 (1990)

[47] S. Alexander, *J. Physique* **38**, 983 (1977)

[48] P.-G. de Gennes, *Macromolecules* **13**, 1069 (1980)

[49] Ye. B. Zhulina, *Vysokomolek. Soedin. B* **25**, 834 (1983)

[50] S. T. Milner, T. A. Witten and M. E. Cates, *Macromolecules* **21**, 2610 (1988)

[51] M. A. Carignano and I. Szleifer, *J. Chem. Phys.* **100**, 3210 (1994)

[52] M. A. Carignano and I. Szleifer, *J. Chem. Phys.* **98**, 5006 (1993)

[53] M. A. Carignano and I. Szleifer, *J. Chem. Phys.* **102**, 8662 (1995)

[54] K. Ohno, T. Sakamoto, T. Minagawa and Y. Okabe, *Macromolecules* **40**, 723 (2007)

[55] M. S. Kent, L.-T. Lee, B. Farnoux and F. Rondelez, *Macromolecules* **25**, 6240 (1992)

[56] R. Toral and A. Chakrabarti, *Phys. Rev. E* **47**, 4240 (1993)

[57] G. S. Grest, K. Kremer and T. A. Witten, *Macromolecules* **20**, 1376 (1987)

[58] M. Daoud and J. P. Cotton, *J. Physique* **43**, 531 (1982)

[59] G. S. Grest, *Macromolecules* **27**, 3493 (1994)

[60] B. J. Bauer, L. J. Fetters, W. W. Graessley, N. Hadjichristidis and G. F. Quack, *Macromolecules* **22**, 2337 (1989)

[61] G. S. Grest, K. Kremer, S. T. Milner and T. A. Witten, *Macromolecules* **22**, 1904 (1989)

[62] K. Ohno and K. Binder, *J. Chem. Phys.* **95**, 5444 (1991)

[63] J. Batoulis and K. Kremer, *Macromolecules* **22**, 4277 (1989)

[64] M. K. Wilkinson, D. S. Gaunt, J. E. G. Lipson and S. G. Whittington, *J. Phys. A: Math. Gen.* **19**, 789 (1986)

[65] J. A. Barrett and D. L. Tremain, *Macromolecules* **20**, 1687 (1987)

[66] K. Shida, K. Ohno, M. Kimura and Y. Kawazoe, *Macromolecules* **33**, 7655 (2000)

[67] K. Ohno, *Cond. Mat. Phys.* **5**, 15 (2002)

[68] R. Guida and J. Zinn-Justin, *J. Phys. A: Math. Gen.* **31**, 8103 (1998)

[69] Ch. von Ferber and Yu. Holovatch, *Cond. Mat. Phys.* **5**, 117 (2002)

[70] T. A. Witten and P. A. Pincus, *Macromolecules* **19**, 2509 (1986)

[71] J. N. Israelachvili, in V. Degiorgio (ed.), *Physics of Amphiphiles: Micelles, Vesicles and Microemulsions*, Proc. Int. School Phys. Enrico Fermi, course XC, 1985, p. 24

[72] C. Tanford, *Proc. Nat. Acad. Sci. USA* **71**, 1811 (1974)

[73] J. S. Pedersen, C. Svaneborg, K. Almdal, I. W. Hamley and R. N. Young, *Macromolecules* **36**, 416 (2003)

[74] K. Stubenrauch, *Functional Amphiphilic Block Copolymers Prepared via Ring Opening Metathesis Polymerization*, PhD Thesis, Graz University of Technology, 2007

[75] K. Stubenrauch, C. Moitzi, G. Fritz, O. Glatter, G. Trimmel and F. Stelzer, *Macromolecules* **39**, 5865 (2006)

[76] V. Castelletto, I. W. Hamley and J. S. Pedersen, *J. Chem. Phys.* **117**, 8124 (2002)

[77] V. Castelletto and I. W. Hamley, *Langmuir* **20**, 2992 (2004)

[78] I. W. Hamley, *Block Copolymers in Solution: Fundamentals and Applications*, John Wiley & Sons Ltd., 2005

[79] A. Halperin, *Macromolecules* **20**, 2943 (1987)

[80] C. Booth and D. Attwood, *Macromol. Rapid Commun.* **21**, 501 (2000)

[81] Y.-W. Yang, N.-J. Deng, G.-E. Yu, Z.-K. Zhou, D. Attwood and C. Booth, *Langmuir* **11**, 4703 (1995)

[82] R. Nagarajan and K. Ganesh, *J. Chem. Phys.* **90**, 5843 (1989)

[83] T. L. Bluhm and M. D. Whitmore, *Can. J. Chem.* **63**, 249 (1985)

[84] L. Oranli, P. Bahadur and G. Riess, *Can. J. Chem.* **63**, 2691 (1985)

[85] D. Nguyen, C. E. Williams and A. Eisenberg, *Macromolecules* **27**, 5090 (1994)

Chapter 3

Electronic Excitations of some Photoinitiator Molecules

3.1 Background

In the following sections a short introduction to the concepts of static and time-dependent Density Functional Theory, many-body theory in the so-called *GW* approximation and the Bethe–Salpeter equation is given as a digest of literature (see citations given in the following sections). This is solely intended as a basis for the discussion and interpretation of the results, as this work was restricted to applying existing concepts to the problems of interest here. There was also a number of standard quantum chemistry methods in use, namely the computation of gradients and geometry optimization on the basis of various theories, calculation of nuclear shielding tensors (NMR chemical shifts) following the Gauge-Independent Atomic Orbital method (GIAO), Complete Active Space SCF (CASSCF) and the modelling of a solvent in the Polarizable Continuum Method (PCM). A description of which can be found in textbooks of quantum chemsitry, e.g. [1, 2, 3].

3.1.1 Density Functional Theory and Time-Dependent Density Functional Theory

Ground State Density Functional Theory

The short overview of Density Functional Theory (DFT) given here follows some prominent books and reviews on the topic [4, 5, 6, 7].

This is all about solving the Schrödinger equation for the many electron problem

$$\left(\hat{T} + \hat{V}_{ee} + \hat{V}_{ext}\right) \Psi(x_1, \ldots, x_N) = E\Psi(x_1, \ldots, x_N) \tag{3.1}$$

with the operator for the kinetic energy

$$\hat{T} = -\frac{1}{2}\sum_{i=1}^{N}\nabla_i^2 \tag{3.2}$$

and the operator for the external potential

$$\hat{V}_{ext} = \sum_{i=1}^{N} v_{ext}(\mathbf{r}_i) = \sum_{i=1}^{N}\sum_{A=1}^{N_{nuc}}\frac{Z_A}{r_{iA}} \tag{3.3}$$

acting on the wave function $\Psi(x_1,\ldots,x_N)$. In the last expression the external potential is supposed to stem solely from the interaction with the nuclei. It is assumed that the nuclei are fixed and decoupled from the electrons. This is known as the Born–Oppenheimer approximation.

Finally, the electron–electron interaction is represented by the two-electron operator

$$\hat{V}_{ee} = \frac{1}{2}\sum_{i\neq j}^{N}\frac{1}{\mathbf{r}_i - \mathbf{r}_j}. \tag{3.4}$$

This last contribution makes the solution of the problem difficult, because it couples the coordinates of the electrons. Otherwise it would have been possible to break the Schrödinger equation down to one-particle equations and make the calculation very simple and straightforward. And it is this point where approximations have to come in.

Note that the wave function is antisymmetric with respect to electron interchange

$$\Psi(x_1,\ldots,x_i,\ldots,x_j,\ldots,x_N) = -\Psi(x_1,\ldots,x_j,\ldots,x_i,\ldots,x_N) \tag{3.5}$$

and normalized

$$\int dx_1\ldots\int dx_N|\Psi(x_1,\ldots,x_N)|^2 = 1. \tag{3.6}$$

The ground state energy is yielded from the Rayleigh-Ritz variational principle, stating that any (antisymmetric, normalized) wave function which differs from the true ground state wave function results in an energy, that is *higher* than the true ground state energy.

$$E = \min_{\Psi}\langle\Psi|\hat{T} + \hat{V}_{ee} + \hat{V}_{ext}|\Psi\rangle \tag{3.7}$$

In **Hartree–Fock Theory (HF)** [8] the two-electron interaction 3.4 is replaced by an effective one-electron mean-field interaction. The system of interacting electrons is hence approximated by a system of non-interacting electrons. The wave function $\Psi(x_1,\ldots,x_N)$ becomes then Φ, the well-known Slater determinant of one-particle orbitals ϕ_i

$$\Phi(x_1,\ldots,x_N) = \frac{1}{\sqrt{N!}}\begin{vmatrix} \phi_1(x_1) & \cdots & \phi_N(x_N) \\ \vdots & & \vdots \\ \phi_1(x_N) & \cdots & \phi_N(x_N) \end{vmatrix} \tag{3.8}$$

If a closed shell system is treated, the Slater determinant can be *restricted* to having the same orbital for the spin-up and spin-down electrons, so the spacial

orbital appears twice—in other words doubly occupied—and is just multiplied by the respective spin function $\sigma(s)$, i.e. $\phi_i(x) = \phi_i(\mathbf{r})\sigma(s)$. The electron–electron interaction reduces then to two contributions

$$\langle \Phi | \hat{V}_{ee} | \Phi \rangle = U[\Phi] + E_{\mathrm{X}}[\Phi] \tag{3.9}$$

Where the first term is the Hartree energy, the Coulomb interaction of a charge distribution with itself.

$$U[\Phi] = \frac{1}{2} \sum_{\sigma\sigma'} \sum_{i,j} \int d\mathbf{r} d\mathbf{r}' \frac{\phi_{i\sigma}^*(\mathbf{r})\phi_{j\sigma'}^*(\mathbf{r}')\phi_{i\sigma}(\mathbf{r})\phi_{j\sigma'}(\mathbf{r}')}{|\mathbf{r} - \mathbf{r}'|} \tag{3.10}$$

It is based on the Coulomb potential,

$$v_i^{\mathrm{coul}}(\mathbf{r}) = \sum_{\sigma'} \sum_{j \neq i} \int d\mathbf{r}' \frac{|\phi_{j\sigma'}(\mathbf{r}')|^2}{|\mathbf{r} - \mathbf{r}'|} \tag{3.11}$$

which is the interaction felt by electron i at $\mathbf{r}$ associated with the charge density of all the other electrons $j \neq i$ averaged over all space. It is *local*, so for instance one could plot a Coulomb potential contour plot in a diagram. The second term in 3.9 is the exchange energy

$$E_{\mathrm{X}}[\Phi] = -\frac{1}{2} \sum_{\sigma} \sum_{i,j} \int d\mathbf{r} d\mathbf{r}' \frac{\phi_{i\sigma}^*(\mathbf{r})\phi_{j\sigma}^*(\mathbf{r}')\phi_{i\sigma}(\mathbf{r}')\phi_{j\sigma}(\mathbf{r})}{|\mathbf{r} - \mathbf{r}'|} \tag{3.12}$$

which is a *non-local* effect due to the Pauli exclusion principle, formally introduced by the antisymmetric Slater determinant[1] There is no simple and exact exchange potential uniquely defined at a point in space, like for the Coulomb part.

The deviation of the Hartree–Fock total energy from the exact one is the definition of the so-called *correlation* energy.

Density Functional Theory (DFT) is of a different spirit. The basic quantity which was proofed to determine all properties of the electronic system is its ground-state electron density $n(\mathbf{r})$. The total energy can hence be written as a *functional* of the density. Any approximate electron density, which differs from the exact density yields a total energy, that is higher than the exact total energy (provided that the functional is exact). This is the counterpart of the variational principle stated for the wave function above.

$$E = \min_n \left(F[n] + \int d\mathbf{r}\, v_{ext}(\mathbf{r})n(\mathbf{r}) \right) \tag{3.13}$$

$F[n]$ is the *universal* part of the energy functional which applies to *all* systems, the remainder is the influence of the external potential that determines the actual electron density. The formal basis of DFT is stated in the Hohenberg–Kohn theorems [9]. For every system it is possible to define a so-called Kohn-Sham system [10], a reference system of non-interacting electrons that yields the same electron density as the real system, defined by the one-particle equations

$$\left[-\frac{1}{2}\nabla^2 + v_s(\mathbf{r}) \right] \phi_i(\mathbf{r}) = \varepsilon_i \phi_i \tag{3.14}$$

---

[1]Note that for one electron the terms for the exchange (3.12) and the Hartree energies (3.10) cancel.

with $v_s(\mathbf{r})$ being the KS potential, and assuming a Slater determinant Φ. The universal functional is

$$F[n] = T_s[n] + U[n] + E_{\mathrm{XC}}[n] \tag{3.15}$$

it contains the exact kinetic energy of the non-interacting KS system $T_s[n]$,

$$T_s[n] = \sum_\sigma \sum_{j=1}^{N_\sigma} \int d\mathbf{r} \frac{1}{2} |\nabla \phi_{j\sigma}(\mathbf{r})|^2 \tag{3.16}$$

which is a good approximation for the kinetic energy of the real system, and the Hartree energy $U[n]$ is equivalently to 3.10

$$U[n] = \frac{1}{2} \sum_{\sigma\sigma'} \int d\mathbf{r}d\mathbf{r}' \frac{n_\sigma(\mathbf{r})n_{\sigma'}(\mathbf{r}')}{|\mathbf{r} - \mathbf{r}'|} \tag{3.17}$$

The remainder is called exchange–correlation energy $E_{\mathrm{XC}}[n]$. It contains by definition an exchange term, a correction for the kinetic energy part and accounts for effects that are subsummarized under the name correlation as above—and is *a priori* unknown. Note that the KS orbitals are *not* that same as the HF orbitals. An expression for the KS potential is obtained from the functional derivatives of the above terms

$$v_{\mathrm{S}\sigma}(\mathbf{r}) = v_{\mathrm{ext}}(\mathbf{r}) + v_{\mathrm{H}}(\mathbf{r}) + v_{\mathrm{XC}\sigma}(\mathbf{r}) \tag{3.18}$$

$$v_{\mathrm{H}}(\mathbf{r}) = \frac{\delta U[n]}{\delta n(\mathbf{r})} = \sum_{\sigma'} \int d\mathbf{r}' \frac{n_{\sigma'}(\mathbf{r}')}{|\mathbf{r} - \mathbf{r}'|} \tag{3.19}$$

$$v_{\mathrm{XC}\sigma}(\mathbf{r}) = \frac{\delta E_{\mathrm{XC}}[n_\alpha, n_\beta]}{\delta n(\mathbf{r})} \tag{3.20}$$

There are several approximations for the unknown exchange–correlation energy functional. An early and simple approach is the *local density approximation* (LDA), which assumes that it is possible to use the features of the uniform electron gas of the same but constant density as the volume element $d\mathbf{r}$ in space one looks at and integrate over all space.

$$E_{\mathrm{XC}}^{\mathrm{LDA}}[n] = \int d\mathbf{r}\, n(\mathbf{r})\varepsilon_{\mathrm{XC}}(n(\mathbf{r})) \tag{3.21}$$

The expression for the exchange part in $\varepsilon_{\mathrm{XC}}(n(\mathbf{r}))$ is taken from the exact expression for exchange [11] of the uniform electron gas.

$$\varepsilon_{\mathrm{X}}^{\mathrm{LDA}} = -\frac{3}{4} \left(\frac{3}{\pi}\right)^{1/3} n(\mathbf{r})^{1/3} \tag{3.22}$$

Note that unlike in the HF case, this effect is assumed to be completely local. It contains the so-called *self-interaction error*—Hartree and exchange–correlation energies for a one-electron system do not cancel, i.e. $U[n] + E_{\mathrm{XC}}[n_\alpha, 0] \neq 0$. For the correlation part, defined to be the remainder $E_{\mathrm{C}} = E_{\mathrm{XC}} - E_{\mathrm{X}}$, there are two often used approximations due to Perdew and Zunger [12] and Vosko, Wilk and Nusair [13], where an approximate correction for the self-interaction error is also incorporated into the functional.

A natural extension to the LDA would be to make the functional not only dependent on the local density, but additionally on the *gradient* of the local density, what yields finally an approximation which is termed *Generalized Gradient Approximation* (GGA). These functionals are sometimes called *semi-local*. Popular examples are the exchange and correlation functionals of Perdew and Wang (PW91) [15], Becke (B88) [14], Perdew, Burke and Ernzerhof (PBE) [17] or Lee, Yang and Parr (LYP) [16].

A more pragmatic approach is to combine several types of functionals, adding their strengths and maximizing cancelations of errors, along with a portion of HF-like *non-local* exchange using expression 3.12 with KS orbitals. The weight of the contributions is optimized by fitting them to reproduce as close as possible properties of a limited number of chemical compounds. This is realized in the B3LYP functional, which is in particular popular in organic chemistry. It has the following ingredients

$$E_{\mathrm{XC}}^{\mathrm{B3LYP}} = (1-a)E_{\mathrm{X}}^{\mathrm{LDA}} + aE_{\mathrm{X}}^{\mathrm{HF}} + bE_{\mathrm{X}}^{\mathrm{B88}} + (1-c)E_{\mathrm{C}}^{\mathrm{VWN}} + cE_{\mathrm{C}}^{\mathrm{LYP}} \qquad (3.23)$$

The parameters were obtained by fitting to a data set of organic molecules, although the b parameter was derived recently [18]. B3LYP uses 20% of exact exchange.

Time-Dependent Density Functional Theory

A lot of literature on TDDFT is available [19, 20, 21, 22, 23] and was used as reference for this short introduction. The formal basis of TDDFT was given by Runge–Gross theorem [27], which plays the same role as the Hohenberg–Kohn theorems for the ground state case. It states that there is a one-to-one mapping between the time dependent density and the time dependent external potential, the potential can hence be written as a functional of the density n (the initial wave function Ψ_0 is assumed to be the non-degenerate ground state), i.e. $v_{\mathrm{ext}}[n](\mathbf{r}t)$.

Similar to the ground state case one can then define a Kohn–Sham system by the following—now time dependent—equation

$$i\frac{\partial \phi_{j\sigma}(\mathbf{r}t)}{\partial t} = \left(-\frac{\nabla}{2} + v_{\mathrm{KS}\sigma}[n](\mathbf{r}t)\right)\phi_{j\sigma}(\mathbf{r}t) \qquad (3.24)$$

where the KS potential is

$$v_{\mathrm{KS}\sigma}[n](\mathbf{r}t) = v_{\mathrm{ext}\sigma}[n](\mathbf{r}t) + \int d\mathbf{r}' \frac{n(\mathbf{r}'t)}{|\mathbf{r}-\mathbf{r}'|} + v_{\mathrm{XC}\sigma}[n](\mathbf{r}t) \qquad (3.25)$$

Starting from a converged ground state KS wave function one can propagate a system in time using equation 3.24. If at the beginning an electromagnetic field is applied, one obtains from this propagation the optical features of the system under investigation and can extract linear and non-linear properties, such as one- and two-photon induced neutral electron excitations.

But usually it is computationally more effective to calculate the first-order response of the ground state to the field, which also corresponds to the linear optical absorption properties. Introducing the response function The first-order response is given by

$$\delta n_\sigma(\mathbf{r}t) = \sum_{\sigma'} \int dt' \int d\mathbf{r}' \chi_{\sigma\sigma'}[n_0](\mathbf{r},\mathbf{r}';t-t')\delta v_{\mathrm{ext}\sigma'}(\mathbf{r}'t') \qquad (3.26)$$

or, based on the KS system

$$\delta n_\sigma(\mathbf{r}t) = \sum_{\sigma'} \int dt' \int d\mathbf{r}' \chi_{\mathrm{KS}\sigma\sigma'}[n_0](\mathbf{r}, \mathbf{r}'; t - t') \delta v_{\mathrm{KS}\sigma'}(\mathbf{r}'t') \qquad (3.27)$$

where the change in the KS potential is again the sum of the individual changes of the external potential and the Hartree and exchange–correlation contributions $\delta v_{\mathrm{KS}\sigma}(\mathbf{r}t) = \delta v_{\mathrm{ext}\sigma}(\mathbf{r}t) + \delta v_{\mathrm{H}\sigma}(\mathbf{r}t) + \delta v_{\mathrm{XC}\sigma}(\mathbf{r}t)$ and $\delta v_{\mathrm{ext}\sigma}(\mathbf{r}t)$ contains a weak electromagnetic field. It can be written in the following form

$$\delta v_{\mathrm{KS}}(\mathbf{r}\omega) = \delta v_{\mathrm{ext}}(\mathbf{r}\omega) + \int d\mathbf{r} \left\{ \frac{1}{|\mathbf{r} - \mathbf{r}'|} + f_{\mathrm{XC}}(\mathbf{r}\mathbf{r}'\omega) \right\} \delta n(\mathbf{r}'\omega) \qquad (3.28)$$

f_{XC} is the so-called exchange–correlation kernel. It is in general a quantity non-local in both, space and time (ω-dependence). Setting it to zero yields the *Random Phase Approximation (RPA)*[2] In conventional TDDFT f_{XC} is usually simplified applying the *adiabatic approximation*. It states that the exchange–correlation potential $v_{\mathrm{XC}}[n](\mathbf{r}t)$ remains the one of the instantaneous ground state $v_{\mathrm{XC}}[n_0](\mathbf{r}t)$, what requires the changes to occur slowly and the system to remain in its ground state at any time. If, additionally, LDA or GGA is employed, f_{XC} looses all non-locality in space and time and becomes, e.g. in the LDA case ("ALDA")

$$f_{\mathrm{XC}}[n](\mathbf{r}\mathbf{r}'\omega) \approx f_{\mathrm{XC}}^{\mathrm{ALDA}}[n_0](\mathbf{r}\mathbf{r}') = \delta(\mathbf{r} - \mathbf{r}') \frac{\partial^2 (n\epsilon_{\mathrm{XC}}(n))}{\partial n^2} \bigg|_{n=n_0(\mathbf{r})} \qquad (3.29)$$

The KS independent-particle response function χ_0 can be constructed employing the Lehmann representation from the KS eigenfunctions $\phi_{i\sigma}(\mathbf{r})$ and eigenvalues ϵ_i

$$\chi_{0\sigma\sigma'}(\mathbf{r}\mathbf{r}'\omega) = \delta_{\sigma\sigma'} \sum_{i,j} (n_{j\sigma} - n_{i\sigma}) \frac{\phi_{j\sigma}^*(\mathbf{r})\phi_{i\sigma}(\mathbf{r})\phi_{i\sigma}^*(\mathbf{r}')\phi_{j\sigma}(\mathbf{r}')}{\omega - (\epsilon_i - \epsilon_j) + i0^+} \qquad (3.30)$$

$n_{i\sigma}$ is the occupation number of orbital $\phi_{i\sigma}(\mathbf{r})$ and 0^+ a positive infinitesimal introduced for mathematical reasons. χ_0 has poles at the KS eigenvalue differences, obvious from equation 3.30, while the poles of χ are at the true excitation energies. The connection between χ_0 and χ is given by the following Dyson-like equation, which is obtained from equating 3.26 and 3.27 and inserting the terms for the KS potential

$$\chi(\mathbf{r}\mathbf{r}'\omega) = \chi_0(\mathbf{r}\mathbf{r}'\omega) +$$
$$\int d\mathbf{r}_1 d\mathbf{r}_2 \, \chi_0(\mathbf{r}\mathbf{r}_1\omega) \left(\frac{1}{|\mathbf{r}_1 - \mathbf{r}_2|} + f_{\mathrm{XC}}(\mathbf{r}_1\mathbf{r}_2\omega) \right) \chi(\mathbf{r}_2\mathbf{r}'\omega) \qquad (3.31)$$

It can be expressed in the following way

$$\chi(\mathbf{r}\mathbf{r}'\omega) = 2 \sum_s \frac{\rho_s(\mathbf{r})\rho_s(\mathbf{r}')}{\omega - \omega_s + i0^+} \qquad (3.32)$$

---

[2]Note that RPA in this context uses KS wave functions to construct excitations. The acronym is also sometimes used to refer to time-dependent HF—in this case HF wave functions are the basis, of course.

where ω_s are the TDLDA excitation energies. The normal modes ρ_s are expanded in the basis of electron transitions i–a between KS orbitals ϕ

$$\rho_s(\mathbf{r}) = \sum_{ia\sigma} X_{ia}^s \phi_{i\sigma}(\mathbf{r}) \phi_{a\sigma}(\mathbf{r}) \left(\frac{\epsilon_a - \epsilon_i}{\omega_s} \right)^{1/2} \tag{3.33}$$

The coefficients X_{ia} and excitation energies ω_s are obtained from the eigenvalue equation

$$\mathbf{R}^{1/2} \left[\mathbf{R} + 4(\mathbf{K}^{\mathrm{H}} + \mathbf{K}^{\mathrm{XC}}) \right] \mathbf{R}^{1/2} \mathbf{X} = \omega_s^2 \mathbf{X} \tag{3.34}$$

with

$$R_{iai'a'} = \delta_{ii'} \delta_{aa'} (n_i - n_a)(\epsilon_a - \epsilon_i) \tag{3.35}$$

and the matrices introducing the Hartree

$$K_{iai'a'}^{\mathrm{H}} = \int d\mathbf{r} d\mathbf{r}' \phi_i(\mathbf{r}) \phi_a(\mathbf{r}) \frac{1}{|\mathbf{r} - \mathbf{r}'|} \phi_{i'}(\mathbf{r}') \phi_{a'}(\mathbf{r}') \tag{3.36}$$

and exchange–correlation interactions

$$K_{iai'a'}^{\mathrm{XC}} = \int d\mathbf{r} \phi_i(\mathbf{r}) \phi_a(\mathbf{r}) f_{\mathrm{XC}}(\mathbf{r}) \phi_{i'}(\mathbf{r}) \phi_{a'}(\mathbf{r}). \tag{3.37}$$

In that way, the linear response equations are solved in the space of single-particle transitions. Having the converged results of the eigenvalue problem 3.34 at hand the oscillator strengths are obtained as

$$f_{ia\sigma} = \frac{2}{3} \left(\left| \vec{x}^T \mathbf{R}^{1/2} \vec{F}_{ia\sigma} \right|^2 + \left| \vec{y}^T \mathbf{R}^{1/2} \vec{F}_{ia\sigma} \right|^2 + \left| \vec{z}^T \mathbf{R}^{1/2} \vec{F}_{ia\sigma} \right|^2 \right) \tag{3.38}$$

where $\vec{F}_{ia\sigma}$ are the elements of the converged eigenvectors $\mathbf{X}$ of 3.34. Note the oscillator strength sum rule for a complete basis of excitations is[3]

$$\sum_{ia\sigma} f_{ia\sigma} = (\text{number of electrons}) \tag{3.39}$$

The connection to the extinction coefficient $\varepsilon(\nu)$ or $\varepsilon(\tilde{\nu})$, which is usually determined in experiments, is given by integrating the absorption spectrum of a transition

$$f = 4.33 \times 10^{-9} \int_0^\infty \varepsilon(\tilde{\nu}) d\tilde{\nu} \tag{3.40}$$

In the above chain-of-thought, the so-called *Tamm-Dancoff approximation (TDA)* was applied. It assumes essentially that the significant contributions to Casida's equation come only from i–a electron transfers, the admixture of emissions a–i is disregarded. This is the TDDFT analogue to configuration interaction method of quantum chemistry involving single excitations only (CIS), and is e.g. used in the implementations of the method in the GAMESS, TURBOMOLE and Gaussian codes.

The TDA has the advantage that it is computationally more effective, but it is an additional approximation in the method. Usually the results with and without TDA do not differ significantly. Contrarely there are cases, when TDA does

---

[3]The vectors $\vec{F}_{ia\sigma}$ form a orthonormalized set $\sum_{ia\sigma} \vec{F}_{ia\sigma} \vec{F}_{ia\sigma}^T = \mathbf{1}$

better than the full treatment, e.g. when excitations far off the equilibrium geometry using hybrid functionals are computed and for open shell systems. This is due to the triplet instability, the occurrence of imaginary excitation energies connected to a poor description of static correlation effects by the exchange–correlation functional for the ground state, which is cured when TDA is used [22]. Note the the Parsec/RGWBS codes were used without this approximation.

3.1.2 Green's Function Based Many Body Perturbation Theory

As can be seen in the preceding section, there are several shortcomings in TDDFT, namely the non-locality in space and time of the exchange–correlation kernel, what leads to poor description of charge-transfer excitations and other long range effects in molecules, and the single particle character of the KS reference system. In this section a different way of describing a many electron system is introduced, which is not yet much in use in chemistry, Green's function or propagator based methods [22, 24, 25, 26, 8].

Any differential equation can be solved involving a so-called Green's functions, for more background see e.g. [28], and so this is the case for the Schrödinger equation defining the many-electron problem stated at the beginning.

$$\hat{H}_0 \Psi = E \Psi \tag{3.41}$$

The Green's function for this zeroth-order problem is

$$(E - \hat{H}_0) G_0(\mathbf{r}, \mathbf{r}', E) = \delta(\mathbf{r} - \mathbf{r}') \tag{3.42}$$

Assuming an effective one-particle description with the Hamiltonian $\hat{H}_0 = \sum_i \hat{f}(i)$, as it is the case in both, HF and the KS system, one can write

$$\hat{f}(i) \phi_i(\mathbf{r}) = \epsilon_i \phi_i(\mathbf{r}) \tag{3.43}$$

and the Green's function becomes

$$G_0(\mathbf{r}, \mathbf{r}', E) = \sum_i \frac{\phi_i(\mathbf{r}) \phi_i^*(\mathbf{r}')}{E - \epsilon_i} \tag{3.44}$$

where i runs over all occupied and unoccupied orbitals and the resulting Green's function has poles for E equal to the eigenvalues of the HF or KS orbitals ϵ_i. The *exact* Green's function $G(E)$ has poles at the exact energy differences between the N and the $(N \pm 1)$-particle systems. These particles have all interactions included in their single particle properties (they are said to be *renormalized*) and are hence called *quasiparticles*. The connection between the non-interacting HF or KS Green's function $G_0(E)$ and $G(E)$ is made by introducing an effective potential, the so-called *self energy* Σ, which is a non-local, energy dependent quantity.

$$G(E) = G_0(E) + G_0(E) \Sigma(E) G(E) \tag{3.45}$$

3.45 is known as Dyson equation. The self energy is then expanded in terms of a *screened Coulomb potential W* instead of the bare Coulomb potential 3.4. W is the interaction of two electrons including the effect of the other electrons around, which is in many cases much weaker than the bare interaction. This transforms

the problem of strongly interacting particles to the problem of weakly interacting quasiparticles and leads to much better convergence than conventional perturbation theory (such as Rayleigh–Schrödinger theory, commonly known as Møller–Plesset theory in quantum chemistry). This leads to a set of equations after Hedin [29]. Where[4]

$$\Sigma(1,2) = i \int d(34) G(1,3) W(4,1^+) \Gamma(3,2;4) \tag{3.46}$$

expresses the self energy in terms of the screened interaction W and the vertex function Γ (see 3.49),

$$W(1,2) = V(1,2) + \int d(34) V(1,3) \chi(3,4) W(4,2) \tag{3.47}$$

is the screened electron–electron interaction,

$$\chi(1,2) = -i \int d(34) G(1,3) G(4,1^+) \Gamma(3,4;2) \tag{3.48}$$

is the polarizability, i.e. the response of the system to an additional particle or hole, and

$$\Gamma(1,2;3) = \delta(1,2)\delta(1,3) + \int d(4567) \frac{\delta\Sigma(1,2)}{\delta G(4,5)} G(4,6) G(7,5) \Gamma(6,7;3) \tag{3.49}$$

is the vertex function obtained from the change in the self energy due to the addition of the particle (or hole)[5]. In general this set requires a self-consistent solution.

In the practical calculations in this work the approach of M. Tiago et al. [30] was used. Assuming a fast convergence in Hedin's equations one can set the self energy in the vertex function 3.49 to zero, it becomes then

$$\Gamma(1,2;3) \approx \delta(1,2)\delta(1,3) \tag{3.50}$$

The polarizability reduces to the RPA polarizability

$$\chi(1,2) \approx -iG(1,2^+)G(2,1) \equiv \chi_0(1,2) \tag{3.51}$$

And for the screened Coulomb interaction one gets

$$W_0(1,2) = \int d(3) \epsilon_0^{-1}(1,3) V(3,2) \tag{3.52}$$

with the dielectric function

$$\epsilon_0(1,2) = \delta(1,2) - \int d(3) V(1,3) \chi_0(3,2) \tag{3.53}$$

And the self energy becomes

$$\Sigma(1,2) = iG(1,2) W_0(2,1^+) \tag{3.54}$$

---

[4]In the following, 1 stays for $(\mathbf{r}_1, \sigma_1, t_1)$, 2 for $(\mathbf{r}_2, \sigma_2, t_2)$ and so forth A "+" denotes holes instead of electrons.

[5]In other words the linear response of the self-energy to a change in the total potential. Vertex corrections acount for exchange–correlation effects between an electron the other electrons in the screening density cloud [22]

This non–self-consistent, approximate solution to Hedin's equations is sometimes called the "one-shot" GW_0 approximation.

It can be enhanced using TDLDA instead of RPA for the polarizability. At the starting point the self energy is taken to be

$$\Sigma(1,2) \approx V_{\text{XC}}(1)\delta(1,2) \tag{3.55}$$

This expression is inserted into 3.49 to give for the vertex function

$$\Gamma(1,2;3) \approx \delta(1,2)\delta(2,3) + \int d(45)\left\{-i\delta(1,2)f_{\text{XC}}(1)\right\}G(1,4)G(5,1^+)\Gamma(4,5;3) \tag{3.56}$$

The irreducible polarizability χ becomes

$$\chi(1,2) = \chi_0(1,2) + \int d(3)\chi_0(1,3)f_{\text{XC}}\chi(3,2) \tag{3.57}$$

and the screened Coulomb interaction

$$W(1,2) = V(1,2) + \int d(34)V(1,3)\Pi(3,4)v(4,2) \tag{3.58}$$

contains the full polarizability Π

$$\Pi(1,2) = \chi(1,2) + \int d(34)\chi(1,3)V(3,4)\Pi(4,2) \tag{3.59}$$

which in terms of

$$\chi(1,2) = \chi_0(1,2) + \int d(3)\chi_0(1,3)f_{\text{XC}}\chi(3,2) \tag{3.60}$$

is

$$\Pi(1,2) = \chi_0(1,2) + \int d(34)\chi_0(1,3)\left\{V(3,4) - f_{\text{XC}}\delta(3,4)\right\}\Pi(4,2) \tag{3.61}$$

which is nothing else than the TDLDA response function.

$$\Pi_f(1,2) = \frac{\delta n(1)}{\delta V_{\text{ext}}(2)} \tag{3.62}$$

Finally the self energy has the following form

$$\Sigma(1,2) = iG(1,2)\left[V(1^+,2) + \int d(34)\left\{V(1,3) + f_{\text{XC}}(1)\delta(1,3)\right\}\Pi(3,4)V(4,2)\right] \tag{3.63}$$

Compared the the RPA based approximation above, the self energy now contains an additional vertex term. This latter level of approximation is denoted GW_f approximation, following [30]. In any case one gets the eigenvalue equation

$$\left[H_{\text{LDA}} + \Sigma - V_{\text{XC}}\right]\psi_j = E_j\psi_j \tag{3.64}$$

with the quasiparticle orbitals ψ_j as an expansion in the basis of Kohn–Sham eigenfunctions and the LDA Hamiltonian H_{LDA}. The equation is then solved by

diagonalization for quasiparticle energies and wave functions. Unlike the Kohn–Sham eigenvalues the quasiparticle energies do have a physical meaning and can be compared directly to photoemission and electron affinity measurements.

Originally it is intended to solve Hedin's equations iteratively to self-consistency, while it remains open how at best to achieve that and what is the effect on the final results [24]. Within this approach, self-consistency could be reached by solving Equation 3.64 and constructing all quantities on the basis of the last iterations quasiparticle eigenfunctions and eigenvalues. Although in practice smooth convergence could not be achieved due to numerical accuracy and thereby triggered instabilities.

3.1.3   The Bethe–Salpeter Equation

The Bethe–Salpeter equation describes neutral excitations of the quasiparticle system in terms of the electron–hole correlation function $L(1, 2; 1^+, 2^+)$ [30] which is

$$L(1, 2; 3, 4) = G(1, 4)G(2, 3) + \int d(5678)G(1, 5)G(6, 3)K(5, 7; 6, 8)L(8, 2; 7, 4)$$
(3.65)

where the Green's function constructed from the eigenvalues and eigenfunctions above enters. The kernel operator, which describes the interaction between the excited electron and hole left behind, is connected to the self-energy by

$$K(1, 2; 3, 4) = -i\delta(1, 3)\delta(2, 4)V(1, 2) + \frac{\delta\Sigma(1, 3)}{\delta G(4, 2)}$$
(3.66)

Several levels of approximation are possible: constructing G from LDA Kohn–Sham eigenvalues and eigenfunctions and letting $\Sigma(1, 2) \approx V_{\mathrm{XC}}(1)\delta(1, 2)$ one returns to the TDLDA eigenvalue equation 3.34, what opens a direct connection between TDDFT and BSE and thereby a way of enhancing f_{XC}; obtaining G from GW_0 and putting $\delta\Sigma/\delta G = iW_0$, what makes $K(1, 2; 3, 4)$ consisting of bare exchange and screened Coulomb interaction; or working on the basis of GW_f, what adds another term to the kernel—a vertex correction based on LDA. In any case an eigenvalue problem like or similar to Equation 3.34 is yielded which is then diagonalized for excitation energies.

3.1.4   Technical Considerations

The above theories can be realized in different bases. The usual way that is followed in computational chemistry is to use sets of Gaussian functions to approximate the wave function of the theory and adjust their coefficients in the course of the SCF procedure [1]. A lot of refined and optimized code libraries are available for the tasks that occur in these calculations and common quantum chemistry software packages such as GAMESS or Gaussian rely heavily on them. Apart from coding, their advantages are that all electrons of light atoms are included explicitly and that a whole lot of data is available in literature, which demonstrates the accuracy and computational cost of a specific basis set. At the other hand, there is no systematic way of converging the quality of the basis set to achieve the desired accuracy of the result, the method is mostly limited to

zero dimensional problems[6] and massive parallelization is not straight forward.

In this work Gaussian basis set based codes were used for HF and DFT geometry optimizations and TDDFT calculations in vacuum and a solvent model.

One alternative that was employed by the Parsec and RGWBS codes is to work in real space [5], i.e. superimposing a lattice at whose sites the wave function and other quantities are computed. This has several advantages: the potential operator is diagonal and reduces computational cost, the mesh size can be converged to the desired numerical accuracy and the technique works for zero dimensional and periodic systems on the same footing. Disadvantages are that the use of pseudopotentials is obligatory, what introduces another source of error, and that the computational cost for small systems with narrowly located electrons (small mesh size necessary) is by far less effective than a computation using a Gaussian basis.

In this work the real space codes were used for LDA single point, TDLDA, GW and GW-BSE computations.

3.1.5 Selection Rules for Electronic Excitations

The approximations in the calculations of electronic excitations, amongst others the Born–Oppenheimer approximation of separating electronic and nuclear wave functions, introduce selection rules. These selection rules are not all strictly fulfilled in the real system but provide a good guidance to the importance of an electronic transition [31].

The transition moment integral M can be separated approximately into

$$M = \int \psi'^* \hat{\mu} \psi d\tau \approx \int \psi_{v'}^* \psi_v d\tau_v \int \psi_{e'}^* \hat{\mu}_e \psi_e d\tau_e \int \psi_{s'}^* \psi_s d\tau_s \tag{3.67}$$

where the first integral is the Frank–Condon factor due to the vibrational states, which is not studied within this work. The second integral is the electronic contribution to the transition moment integral causing the orbital selection rules ($\hat{\mu}_e$ denotes the component of the dipole moment operator that depends only on electron coordinates), and the last term accounts for the spin selection rule. Primed wave functions are always referring to the excited state.

The *spin selection rule* is simple: the multiplicity of the two states involved in the transition must be the same. Hence only singlet–singlet, triplet–triplet transitions and so forth are allowed. This rule is rather strict, spin forbidden transitions have in general a very low absorbance.

The *orbital selection rule* is somewhat less strict, typical extinction coefficients for orbital forbidden transitions are in the order of 10^0–10^3 M^{-1} cm^{-1}. It is determined from the character tables for the symmetry point group of the molecule, what is demonstrated in the following for the two point groups relevant in this work: C_2 and C_{2v}.

For the C_2 point group the character table is

C_2	E	C_2	
A	1	1	z
B	1	-1	x, y
$\Gamma_{x,y,z}$	3	-1	

(3.68)

---

[6]The term zero dimensional refers to single molecules or small clusters, as opposed to long chains (1-dim), surfaces (2-dim) or crystals (3-dim), where a box with periodic boundary conditions contents the system.

The dipole moment operator $\hat{\mu}_e$ has three components which transform as x, y or z. As the ground state is always totally symmetric (A) and the excited state can be of A or B symmetry one finds two cases for the symmetry of the orbital selection integral

$$\int \psi_{e'}^* \hat{\mu}_e \psi_e \sim \quad A \begin{pmatrix} a \\ b \end{pmatrix} A = \begin{pmatrix} a \\ b \end{pmatrix} \tag{3.69}$$

$$\text{and} \quad B \begin{pmatrix} a \\ b \end{pmatrix} A = \begin{pmatrix} b \\ a \end{pmatrix} \tag{3.70}$$

If now the ground state symmetry A is found in the triple product $\Gamma(\psi_{e'}) \times \Gamma(\hat{\mu}_e) \times \Gamma(\psi_e)$, the transition is allowed—what is true for both cases above.

For the C_{2v} point group the character table looks like

C_{2v}	E	C_2	$\sigma_v(xz)$	$\sigma_v'(yz)$	
A_1	1	1	1	1	z
A_2	1	1	-1	-1	
B_1	1	-1	1	-1	x
B_2	1	-1	-1	1	y
$\Gamma_{x,y,z}$	3	-1	1	1	

$$\tag{3.71}$$

and the orbital selection rules are determined by

$$\int \psi_{e'}^* \hat{\mu}_e \psi_e \sim \quad A_1 \begin{pmatrix} a_1 \\ b_1 \\ b_2 \end{pmatrix} A_1 = \begin{pmatrix} a_1 \\ b_1 \\ b_2 \end{pmatrix} \tag{3.72}$$

$$A_2 \begin{pmatrix} a_1 \\ b_1 \\ b_2 \end{pmatrix} A_1 = \begin{pmatrix} a_2 \\ b_2 \\ b_1 \end{pmatrix} \quad \text{forbidden!} \tag{3.73}$$

$$B_1 \begin{pmatrix} a_1 \\ b_1 \\ b_2 \end{pmatrix} A_1 = \begin{pmatrix} b_1 \\ a_1 \\ a_2 \end{pmatrix} \tag{3.74}$$

$$\text{and} \quad B_2 \begin{pmatrix} a_1 \\ b_1 \\ b_2 \end{pmatrix} A_1 = \begin{pmatrix} b_2 \\ a_2 \\ a_1 \end{pmatrix} \tag{3.75}$$

So it is demonstrated that transitions from the gound to an A_2 excited state do not yield the ground state symmetry in the triple product. Hence these transitions are forbidden by orbital symmetry.

3.2 Results

In the following sections data for optimized geometries and neutral excitation properties for benzophenone, 1,5-diphenylpenta-1,4-diyn-3-one (DPD) and its derivatives 1,5-bis(4-methoxyphenyl)penta-1,4-diyn-3-one (ODPD), 1,5-bis-(4-(methylthio)phenyl)penta-1,4-diyn-3-one (SDPD) and 1,5-bis(4-(dimethylamino)phenyl)penta-1,4-diyn-3-one (NDPD) are presented. The data are compared to experimental measurements and results from other methods, according to availability. TDDFT was done for all compounds, whereas GW and GW-BSE could only be applied to benzophenone and DPD for computational reasons.

3.2.1 Benzophenone

Geometry

Being a small molecule the geometry of benzophenone, Figure 3.1, is not very difficult to determine, with one exception—the torsion angle between the phenyl rings and the keto plane O=C–C^1–C^2 or, equivalently, the angle between the two phenyl rings, which should be defined here as the dihedral C^1–C^6–C$^{1'}$– C$^{6'}$ (referring to the two vertical *ipso-ortho* aromatic bonds in Figure 3.1). This internal coordinate was in question in both, experimental observations and computational approaches.

In this work the geometry was obtained from an HF/cc-pVTZ optimization run, see Figure 3.2, using GAMESS [32] with a maximum gradient of 10^{-5} Hartree Bohr^{-1} taken as convergence criterium. A C_2 symmetry was assumed. It revealed a dihedral angle between the phenyl ring and the keto plane of 33.8, and an angle between the ring planes of 57.7°. Additionally, a geometry optimum was determined on the B3LYP/cc-pVTZ hypersurface using the same parameters as above. Both results are compared to previous theoretical results and experimental data, see Table 3.1.
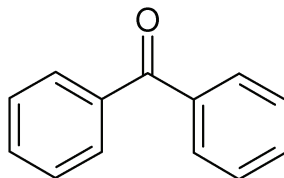
Figure 3.1: Schematic structure of the benzophenone molecule.
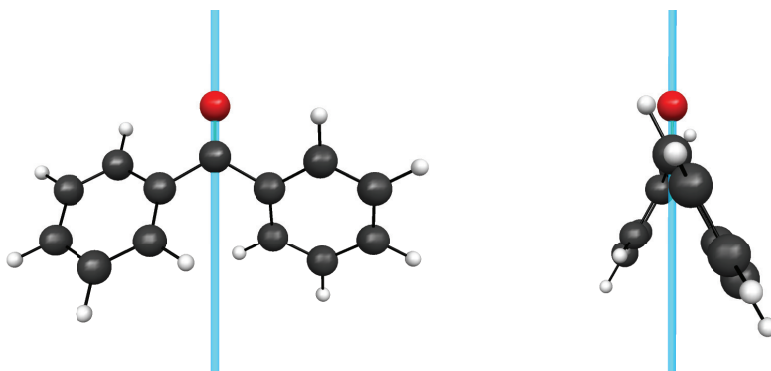
Figure 3.2: Front and side views [33] of the HF/cc-pVTZ optimized structure of benzophenone. The blue line marks the C_2 rotation axis of the assumed symmetry.

Table 3.2 compiles ^{1}H and ^{13}C NMR chemical shifts from experiment [38] and calculations using the Gauge-Independent Atomic Orbital (GIAO) method as implemented in Gaussian [39] with default parameters at the B3LYP/ IGLO-II level for both, the HF- and the B3LYP-optimized geometries. The isotropic

Table 3.1: Geometric data of benzophenone from optimizations with different methods and basis sets and from X-ray experiments for the crystals (superscripts mean *(c)arbonyl, (i)pso, (o)rtho, (m)eta* and *(p)ara*; [a] this work).

internal coord.	HF STO-3G [34]	MP2 3-21G [35]	X-ray [36]	HF cc-pVTZ [a]	B3LYP cc-pVTZ [a]
$O-C^c$	1.225 Å	1.261 Å	1.23 Å	1.191 Å	1.218 Å
C^c-C^i	1.528 Å	1.505 Å	1.48–1.50 Å	1.501 Å	1.499 Å
$C^i-C^c-C^{i'}$	119.1°	119.1°	122°	120.4°	120.6°
$O-C^c-C^i-C^o$	33.3°	—	—	33.8°	27.8°
$C^o-C^i-C^{i'}-C^{o'}$	54°	49°	56°	57.7°	52.9°

Table 3.2: ^{1}H and ^{13}C NMR chemical shifts for benzophenone, measured values in d-chloroform taken from [38] (superscripts mean *(c)arbonyl, (i)pso, (o)rtho, (m)eta* and *(p)ara*); all values in ppm.

	experiment	calculated values	
		HF geometry	B3LYP geometry
H^o	7.79	7.32 / 7.95	7.62 / 8.28
H^m	7.46	7.21 / 7.42	7.43 / 7.63
H^p	7.57	7.41	7.64
C^c	196.50	196.05	201.79
C^i	137.58	143.81	145.24
C^o	129.96	134.06 / 134.71	136.79 / 137.97
C^m	128.21	130.34 / 132.68	132.45 / 134.77
C^p	132.33	135.47	138.19

nuclear shieldings are referenced to tetramethylsilane, whose shielding was computed in the same way.

Deviations between the two geometries occur for the carbonyl C–O bond and the angle between the two phenyl rings. HF underestimates the C–O bond length, an observation that was made before [1]. HF comes closer to the phenyl–phenyl dihedral angle measured by X-ray diffraction [36]. Note that the latter was measured for the crystal phase. But there is evidence that a similar picture is true for powders, melts and solutions [37]. All sited experimental sources find the C_2 symmetry within standard errors of the data, which was used as a constraint to the geometry optimizations. The NMR shifts show the usual uncertainties of the GIAO method at the applied level, although the HF geometry shows better agreement, in particular for the ^{13}C shifts (and inclusively the carbonyl C).

Ground State Properties and Neutral Excitations

Ground state properties and electronic excitations were determined using the previously obtained geometries. Most calculations were done with the HF/cc-pVTZ-optimized structure, while the B3LYP structure was used for a few tests only, to show how minor geometry changes affect the results.

Within DFT/TDDFT, a first approach was to use LDA to allow also a comparison with the results from the real space code (RGWBS), with the Perdew–Zunger functional PZ81 employed[7]. Secondly a GGA functional was used: PBE, for the reasons of being increasingly popular in quantum chemistry and its comparably sound theoretical basis [23]. These calculations were done using again the GAMESS code and starting from a well converged wave function, obtained with a convergence threshold of 1×10^{-7} change in the electron density. The basis set for all tasks was cc-pVTZ, which is assumed to be large enough to cover all major effects but still permits smooth convergence. Results of linear response TDDFT using the LDA and GGA functionals are given in Table 3.3, along with Kohn–Sham orbital assignments and experimental data for the gas phase and solutions in acetonitrile and hexane. Real space TDLDA excitation energies from Parsec (see below) are given in Table 3.6.

The lowest excitation in the TDLDA and TDPBE spectrum is almost exclusively of $n_O \rightarrow \pi^*$ character, compare Table 3.3 and Figure 3.3, in accordance with what can be deduced from experimental solvent shifts [42, 44]—a hypsochromic shift (increasing excitation energy with increasing solvent polarity) and the absence of the band in acidic media due to protonation of the carbonyl O. Furthermore its energy is in good agreement with the measured flourescence excitation spectrum. The nature of the intensive band (state no. 6 after both functionals) is predicted to be the $\pi \rightarrow \pi^*$ transition, like experimental absorptions spectra suggest. The excitation energy here seems to be too low (the $\pi \rightarrow \pi^*$ exhibits a bathochromic shift, i.e. the excitation energy increases with decreasing solvent polarity [44]). TDLDA and TDGGA excitation energies differ only marginally, a behavior that was found already for e.g. naphthalene [23].

Note that, strictly speaking, the Kohn–Sham orbitals do not have a chemical significance themselves[8], they only belong to the reference system of non-interacting electrons and produce the total electron density of the real system (if the functional is exact). However it was shown that KS orbitals are nevertheless physically sound and suitable for qualitative chemical appliations [45, 46].

A natural extension for molecules containing polar groups is the inclusion of HF-like exchange, popularly done in the form of hybrid functions. The choice was like for the geometry optimizations B3LYP. The excitation energies and assignments are given in Table 3.4. The assigned KS orbitals are shown in Figures 3.3 and 3.6. TDB3LYP results were also obtained for the B3LYP optimized geometry. Additionally TDB3LYP calculations were done considering a solvent environment. This was included employing the PCM model for acetonitrile. The calculations were carried out with the Gaussian03 program suite. The cavity was built of spheres from the United Atom Topological Model with 1.2 times the UFF force field radii. Two different models were used, the default UA0 model and another one whose radii are optimized for DFT calculations (UAKS). Note the difference in the B3LYP functional between GAMESS, where VWN equation number 5 is used, and Gaussian03 taking expression 1 of VWN [13]. This results in slight but insignificant deviations. The basis set was again cc-pVTZ.

Table 3.4 and Figures 3.6 and 3.7 show excitation properties and orbitals

---

[7]The LDA functional better known in chemistry is VWN; only insignificant differences to PZ81 were found in some test calculations.

[8]Note also that arguing chemical properties on the basis of orbitals of a single configuration does have in general its limitations.

from TDB3LYP in gas phase and PCM acetonitrile. In general admixing HF exchange in the functional increases the excitation energies, as found in other cases [23]. Note that the orbital order changes (HOMO−3 ⟷ HOMO−4), while the assignments stay rather similar. Diffuse excitations are often improved, but for valence excitations this is not always the case. This might be also the reason for the shift of the intensive B-bands (states 4 and 15 in Table 3.4), although no direct comparison with experiment is available. Note the lesser $n_O \to \pi^*$ character in the weak A-band, compared to TDLDA, and the deviation from the gas phase value. The difference between HF-optimized and B3LYP-optimized geometries is significant (0.1–0.2 eV), with comparable deviations from experiment. The larger change in excitation energy occurs with the $\pi \to \pi^*$ transitions, where also the ground state optimized geometry differed at most from the HF picture, namely in the phenyl–phenyl dihedral angle influenced by the phenyl π-electron cloud. The shifts in excitation energies when transferring the molecule from vacuum into acetonitrile are in accordance with the experiments. While the orbitals and transition assignments are not fundamentally changed.

Simulated spectra from all TDDFT levels, along with the experimental spectrum in acetonitrile [43, 51] are shown in Figures 3.4 and 3.5. The theoretical excitation energies and oscillator strenghts were broadened by Gaussians of width 0.4 eV and superimposed to match a typical experiment. The 15 lowest excitations were used, where the highest considered excitation energies are 5.6 eV for TDLDA, 5.7 eV for TDPBE and 6.3 eV for TDB3LYP. A comparison of HF- and B3LYP-optimized structures is shown in the same manner in Figures 3.8 and 3.9.

GW_f-BSE calculations were based on LDA Kohn–Sham orbitals obtained with the Parsec code [47, 48] in real space. The benzophenone geometry from HF/cc-pVTZ-optimization was set into a spherical cavity of radius 8 Å (convergence: 0.0001 eV for the HOMO and total energy, and 0.01 eV for LUMO+10) and a grid spacing of 0.20 Å (convergence: 0.0003 eV for individual orbitals, and 0.01 eV for the total energy). Wave functions vanish outside the cavity. Pseudopotentials (PP) were generated using Martins' code [49] and the Troullier–Martins scheme [50] employing the PZ81 LDA functional. In general PPs were soft (large cutoff radii) to facilitate SCF convergence and tested extensively for the physico-chemical relevance of the obtained results. Parameters were as follows: for hydrogen the 1s electron was left in the valence, the cutoff radius was set to 2.00 a.u. (1.06 Å); for carbon the 1s orbital was incorporated into the core, cutoff radii for the 2s and 2p valence orbitals were 1.64 a.u. (0.46 Å); for oxygen the 1s orbital was also part of the core, cutoffs for 2s and 2p orbitals were 1.79 a.u. (0.95 Å). In all cases the core charge cutoff was set to the radius where core and valence charges have the same magnitude. The convergence criterion for the LDA SCF cycles was set to 2×10^{-4} Ry. In the calculation of the TDLDA excitation energies, the TDLDA polarizability, static screened interaction, self energy corrections, quasiparticle energies and the Bethe–Salpeter equation 34 occupied and 366 unoccupied orbitals were used. Thereby the sum rule in TDLDA was satisfied to within 28%, a value which was found to assure a accuracy of 0.1 eV in the quasiparticle energies [30].

Eigenvalues of HF, Kohn–Sham and quasiparticle states are compiled in Table 3.5. Only the HF and KS HOMOs and the GW eigenvalues have a physical meaning, provided in the KS case that the exact functional is known.

Table 3.3: Important TDLDA and TDPBE excitations for the HF/cc-pVTZ-optimized structure of benzophenone from GAMESS along with major contributions of KS orbital transitions.

state	energy	sym	osc.	major contributions		
	eV			origin	target	percent
TDLDA						
1	3.25	A	0.001	HOMO	LUMO	91
6	4.42	B	0.165	HOMO−4	LUMO	40
				HOMO−2	LUMO	22
				HOMO	LUMO+2	17
15	5.64	B	0.064	HOMO−6	LUMO	48
				HOMO−3	LUMO+2	31
TDPBE						
1	3.30	A	0.001	HOMO	LUMO	92
6	4.45	B	0.155	HOMO−4	LUMO	35
				HOMO−2	LUMO	22
				HOMO	LUMO+2	21
15	5.68	B	0.165	HOMO−3	LUMO+2	53
experiment, gas phase [a]						
	3.30 (3.25)		maximum (0_0^0 onset) from vibrationally resolved spectrum of S_1			
experiment, solution [b]						
	3.66; 3.58		0.1–0.2			
	4.96; 5.01		16.6–21.8			

[a] measured fluorescence excitation in a collision free supersonic jet in He gas carrier [41];
[b] measured in MeCN and hexane (2nd values), extinction coefficients $\varepsilon \times 10^{-3}$ M^{-1} cm^{-1} [42, 43, 44]; osc. = oscillator strength.

LUMO+1
$\epsilon = -1.74$ eV
A

LUMO+2
$\epsilon = -1.61$ eV
A

LUMO+3
$\epsilon = -1.42$ eV
B

HOMO−1
$\epsilon = -6.78$ eV
B

HOMO
$\epsilon = -5.85$ eV
B

LUMO
$\epsilon = -2.80$ eV
B

HOMO−4
$\epsilon = -6.91$ eV
A

HOMO−3
$\epsilon = -6.83$ eV
B

HOMO−2
$\epsilon = -6.83$ eV
A
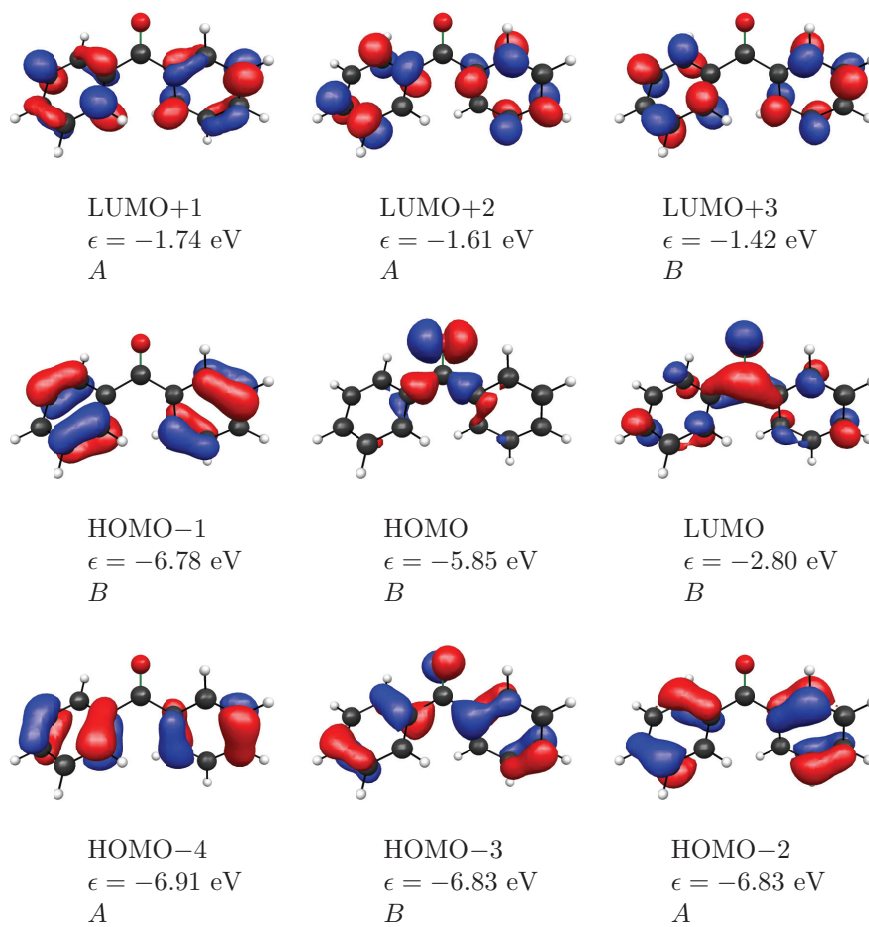
Figure 3.3: LDA KS orbitals for benzophenone (HF-optimized) from GAMESS. The KS orbital eigenvalues ϵ and their symmetry is also specified, the contour value for the plot was 0.05.

Table 3.4: Lowest important TDB3LYP excitations for benzophenone along with major contributions of KS orbital transitions (comments on experiments see Table 3.3).

state	energy eV	sym	osc.	origin	target	percent
					major contributions	
				origin	target	percent
TDB3LYP(VWN5) [a]						
1	3.76	A	0.001	HOMO	LUMO	77
4	4.94	B	0.228	HOMO−3	LUMO	53
				HOMO−2	LUMO	34
15	6.27	B	0.166	HOMO−4	LUMO+2	38
				HOMO−3	LUMO+3	31
TDB3LYP(VWN5) [b]						
1	3.61	A	0.001	HOMO	LUMO	74
4	4.76	B	0.251	HOMO-3	LUMO	45
				HOMO-2	LUMO	43
15	6.19	B	0.144	HOMO-3	LUMO+3	32
				HOMO-4	LUMO+2	29
TDB3LYP(VWN1) in PCM MeCN [a,c]						
1	3.90	A	0.001	HOMO	LUMO	62
	3.84		*0.001*			*70*
4	4.79	B	0.326	HOMO−3	LUMO	68
	4.84		*0.295*			*64*
13	6.25	B	0.137			
15	*6.29*		*0.127*	*HOMO−4*	*LUMO+2*	*52*
experiment, gas phase						
3.30 (3.25)			maximum (0_0^0 onset) from vibrationally resolved spectrum of S_1			
experiment, solution						
3.66; 3.58			0.1–0.2			
4.96; 5.01			16.6–21.8			

[a] calculation for HF/cc-pVTZ-optimized geometry; [b] calculation for B3LYP/cc-pVTZ-optimized geometry; [c] the cavity is based on UA0 topological model, italic values are based on an optimized model for DFT (UAKS).

Table 3.5: HF, Kohn–Sham and quasiparticle eigenvalues (in eV) for benzophenone for the HF/cc-pVTZ-optimized geometry. The experimental PES shows a broad $5e^-$ band with maximum at 9.41 and shoulder at 8.97 eV [40].

orbital	HF [a]	LDA [a]	LDA [b]	PBE [a]	B3LYP [a]	GW [b]
HOMO	−9.39	−5.84	−5.85	−5.63	−6.80	−8.92
HOMO−1	*−9.45*	*−6.77*	*−6.70*	*−6.53*	*−7.19*	−8.92
HOMO−2	*−9.47*	*−6.82*	*−6.77*	*−6.58*	*−7.24*	−9.14
HOMO−3	*−9.59*	*−6.83*	*−6.80*	*−6.59*	*−7.33*	−9.20
HOMO−4	*−11.41*	*−6.90*	*−6.85*	*−6.66*	*−7.34*	−9.25

[a] in cc-pVTZ Gaussian basis using GAMESS; [b] in real space using Parsec, see text for details; the italic figures do not have an immediate physical meaning.
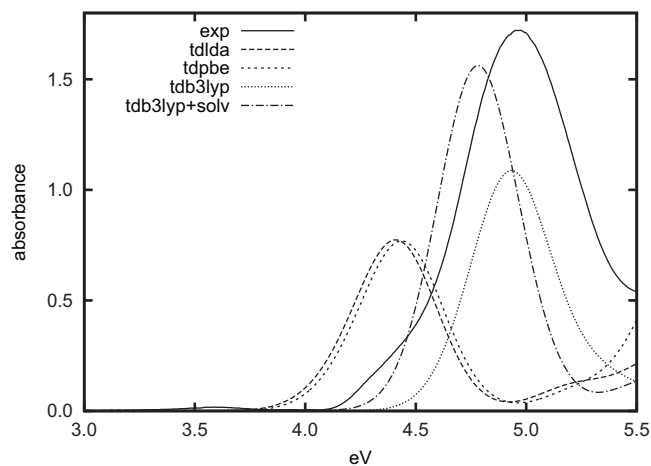
Figure 3.4: TDLDA, TDPBE, TDB3LYP(VWN5), TDB3LYP(VWN1) with PCM acetonitrile of benzophenone (HF-optimized) and experimental UV/vis spectrum in acetonitrile [51]. The left scale belongs to the experimental line, the scaling of the computed spectra is arbitrary but the same for the four.

Figure 3.5: Same as figure 3.4 but zoom to lowest weak transition. Experimental spectrum is 1×10^{-3} M in acetonitrile [51].

LUMO+1
$\epsilon = -0.65$ eV
A

LUMO+2
$\epsilon = -0.49$ eV
A

LUMO+3
$\epsilon = -0.27$ eV
B

HOMO−1
$\epsilon = -7.18$ eV
B

HOMO
$\epsilon = -6.80$ eV
B

LUMO
$\epsilon = -1.71$ eV
B

HOMO−4
$\epsilon = -7.35$ eV
B

HOMO−3
$\epsilon = -7.32$ eV
A

HOMO−2
$\epsilon = -7.24$ eV
A

Figure 3.6: B3LYP KS orbitals for benzophenone (HF-optimized). ϵ refers to the KS eigenvalue for the orbital, at the bottom the symmetry is specified. The contour value for the plot was 0.05.

LUMO+1
$\epsilon = -0.72$ eV
A

LUMO+2
$\epsilon = -0.67$ eV
B

LUMO+3
$\epsilon = -0.54$ eV
A

HOMO−1
$\epsilon = -7.23$ eV
B

HOMO
$\epsilon = -7.05$ eV
B

LUMO
$\epsilon = -1.89$ eV
B

HOMO−4
$\epsilon = -7.51$ eV
B

HOMO−3
$\epsilon = -7.36$ eV
A

HOMO−2
$\epsilon = -7.29$ eV
A
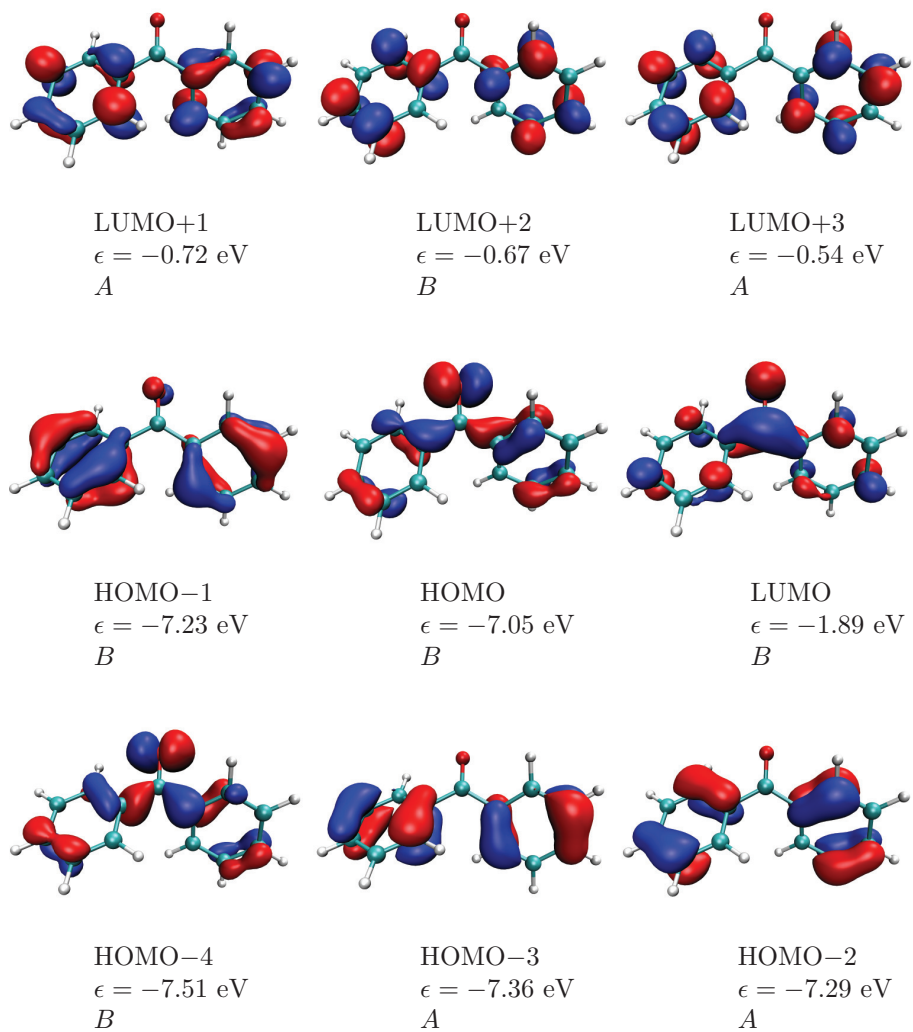
Figure 3.7: B3LYP/cc-pVTZ KS orbitals for benzophenone (HF-optimized) from Gaussian03 in PCM acetonitrile. Underneath the orbital specification ϵ refers to the KS eigenvalue, the contour value for the plot was 0.05 (graphics by VMD, see [31] in Chapter 2).
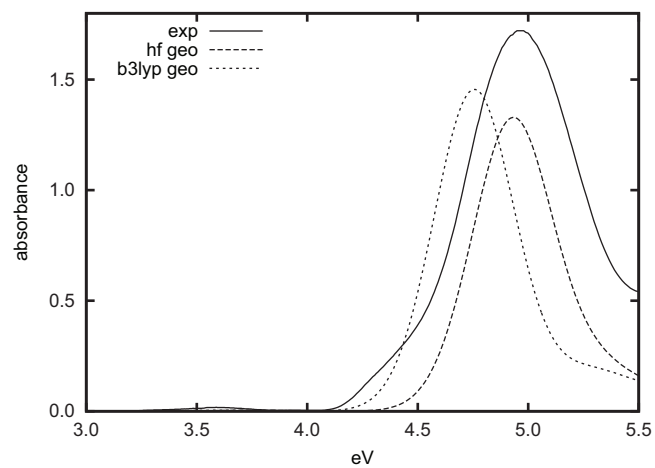
Figure 3.8: TDB3LYP(VWN5) for HF and B3LYP optimized structures and experimental UV/vis spectrum in acetonitrile (red, solid) [51] of benzophenone.
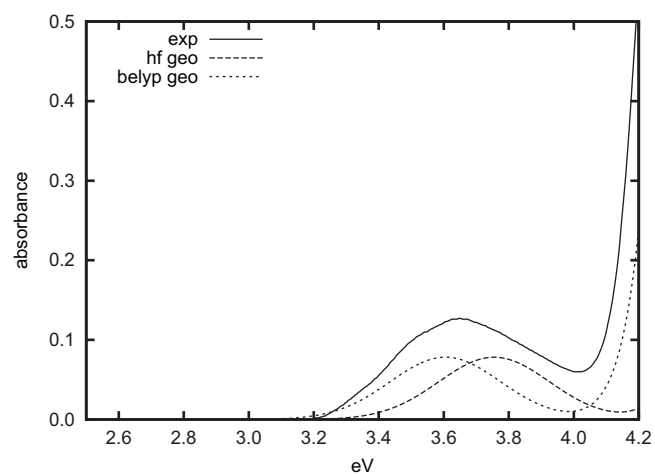
Figure 3.9: Same as figure 3.8 but zoom to lowest weak transition. Experimental spectrum is 1×10^{-3} M in acetonitrile [51].

Table 3.6: Important TDLDA and GW-BSE excitations of HF/cc-pVTZ-optimized benzophenone from Parsec/RGWBS codes (osc. str. = oscillator strength).

LDA			GW_f-BSE		
energy (eV)	osc. str.	symmetry	energy (eV)	osc. str.	symmetry
3.28	0.001	A	3.07	0.001	A
4.40	0.133	B	4.39	0.402	B
5.65	0.177	B	6.29	0.703	B
6.27	0.072	A	6.38	0.188	B
6.29	0.062	B			

The photoelectron (PE) spectrum [40] shows a broad band with a maximum at 9.47 eV and a shoulder at 8.97 eV, which corresponds to five electrons, four from the π-ionizations originating from the orbitals at the phenyl rings and one from the lone pair of the carbonyl oxygen n_O. Note that the experimental values refer to the maxima of the band, i.e. the vertical energy difference between ground and ionized states. Strictly the adiabatic 0-0 transitions should be compared to the KS eigenvalues and quasiparticle energies, which are expected to lie a few hundredths to tenths of an eV lower.

While HF overestimates the ionization potential by 0.4 eV, LDA and GGA are off by more than 3 eV, an effect that is connected to the general poor quality of higher KS eigenvalues due to the deviation of their potential from the exact one far from the nuclei [23]. This situation is only in part cured by admixture of HF exchange in the case of B3LYP. At the other hand quasi-particle energies of GW_f compare well to experimental values. The quasi-particle energy of -8.92 eV and the group of orbitals with eigenvalues between -9.10 and -9.25 eV can be assigned to the highest, broad band in the PE spectrum. The onset of lower-lying orbitals in the spectrum is then about 11.5 eV, which in turn corresponds to the HOMO-5 of GW with -11.55 eV. Klasinc et al. [40] assign the lone pair ionization to the high energy side of the broad band, rather than to the shoulder. In contrast the GW results suggest some lone pair ionization character in both sides of the band, see Figure 3.12.

The quasiparticle orbitals, depicted in Figure 3.12, support the DFT picture. In particular this is true for B3LYP, whose orbital order also agrees with GW_f. The GW_f-BSE excitation energy of the lowest, weak A-transition is further lowered compared with TDLDA, thus is agrees less with the experiment (but still better than B3LYP). At the other hand the intensive B-band stays almost unchanged. Higher (diffuser) excitations are shifted, in particular the second intense B-transition, which is increased from 5.65 eV in TDLDA to 6.29 eV— again a support for the B3LYP values. Note also that the oscillator strength of this high excitation is increased from TDLDA by all, TDPBE, TDB3LYP and GW_f-BSE. The LDA KS orbitals from Parsec underlying the GW_f and BSE calculations are approximately the same as the ones found with GAMESS in Figure 3.3, and not shown for this reason. Simulated spectra containing all excitations from TDLDA and GW_f-BSE, broadened by Gaussians of width 0.4 eV, are shown again in Figures 3.10 and 3.11, along with the experimental spectrum in acetonitrile [43, 51].
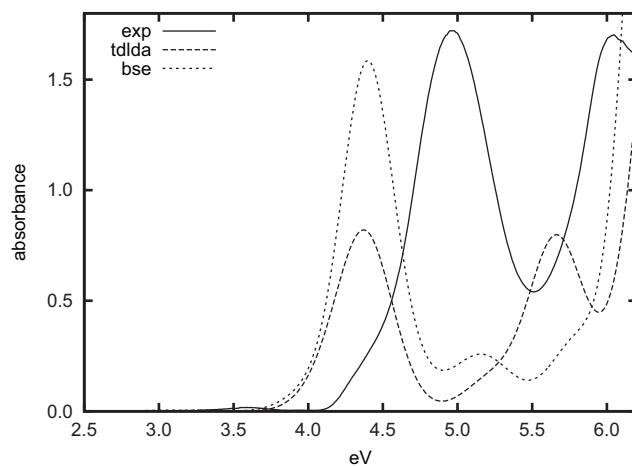
Figure 3.10: TDLDA and GW-BSE spectra of benzophenone (HF-optimized) and experimental UV/vis spectrum [51]. The left scale belongs to the experimental line, the scaling of the TDLDA and GW-BSE lines is arbitrary but the same for the two.
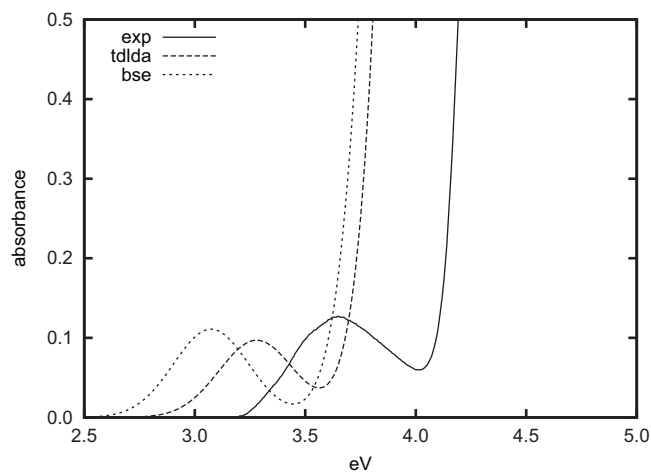
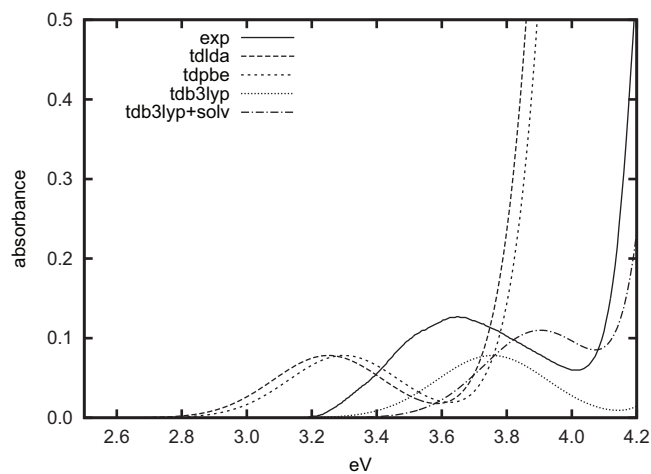
Figure 3.11: Same as figure 3.10 but zoom to lowest weak transition. Experimental spectrum is 1×10^{-3} M in acetonitrile [51].
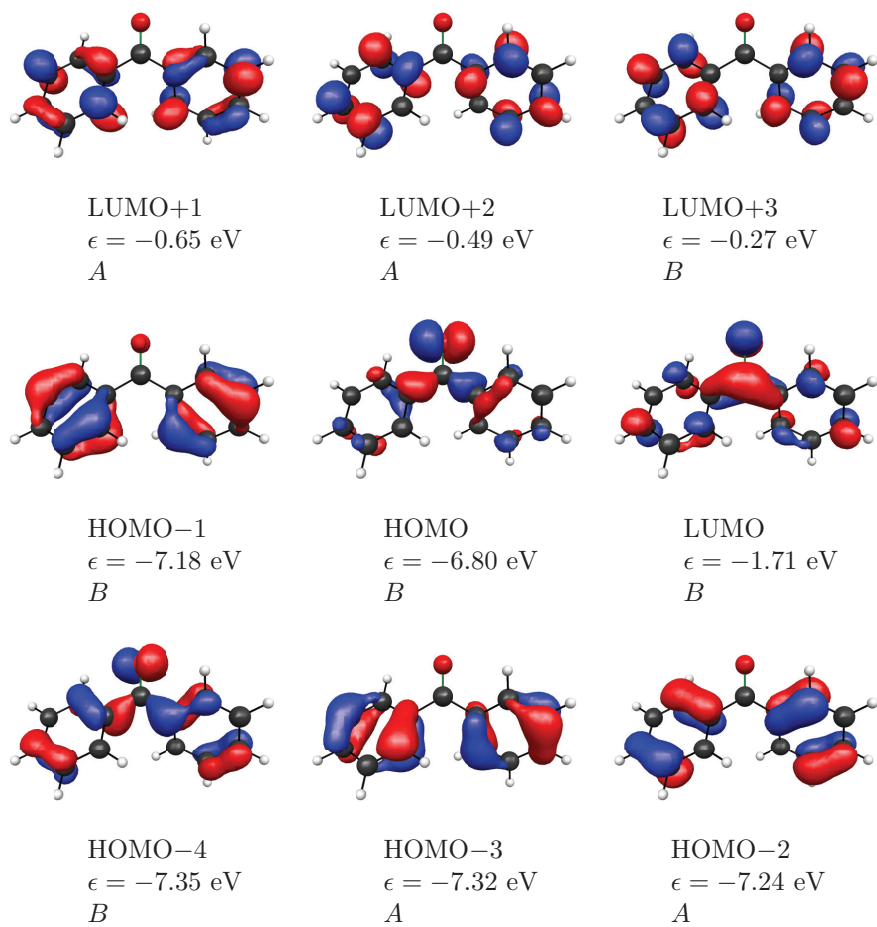
LUMO+1$_{\text{(LUMO+1)}}$
$\epsilon = 0.67$ eV
A, $c = 0.04$

LUMO+2$_{\text{(LUMO+2)}}$
$\epsilon = 0.42$ eV
A, $c = 0.04$

LUMO+3$_{\text{(LUMO+3)}}$
$\epsilon = 0.67$ eV
B, $c = 0.03$

HOMO−1$_{\text{(HOMO−1)}}$
$\epsilon = -8.92$ eV
B, $c = 0.04$

HOMO$_{\text{(HOMO)}}$
$\epsilon = -8.92$ eV
B, $c = 0.09$

LUMO$_{\text{(LUMO)}}$
$\epsilon = -1.04$ eV
B, $c = 0.06$

HOMO−4$_{\text{(HOMO−3)}}$
$\epsilon = -9.25$ eV
B, $c = 0.08$

HOMO−3$_{\text{(HOMO−4)}}$
$\epsilon = -9.20$ eV
A, $c = 0.04$

HOMO−2$_{\text{(HOMO−2)}}$
$\epsilon = -9.14$ eV
A, $c = 0.03$
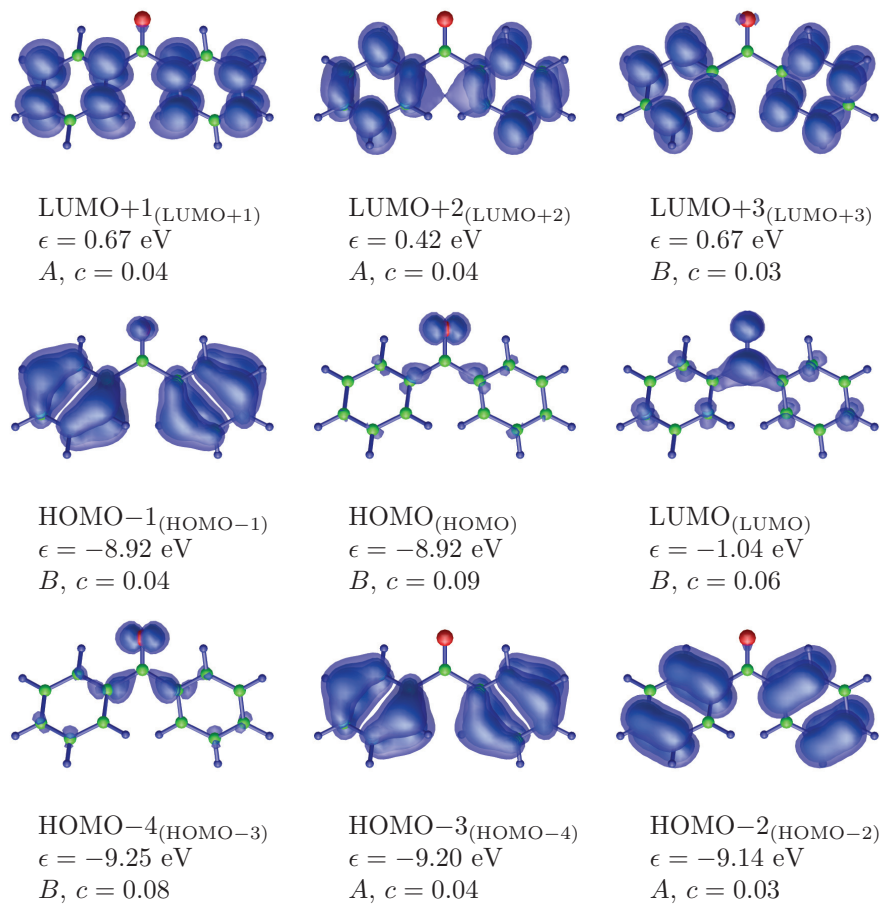
Figure 3.12: Quasiparticle orbitals for benzophenone from PARSEC/GW-BSE codes. The orbital specification in parenthesis refers to the corresponding zeroth order LDA KS orbital, ϵ is the eigenvalue (quasi-particle energy) and c the outer contour value for the plot.

3.2.2   1,5-Diphenylpenta-1,4-diyn-3-one (DPD)

Geometry

As in the benzophenone case ground state optimized geometries of DPD, Figure 3.13, were obtained at the HF/cc-pVTZ and B3LYP/cc-pVTZ levels. A C_{2v} symmetry was assumed in the optimizations, which was also found when lifting the symmetry constraint and starting optimizations from non-planar C_2 and C_s symmetries. The HF-geometry is shown in Figure 3.14, data for both are given in Table 3.7. The last line in the table refers to the dihedral angle between the phenyl and keto planes—which is constraint to 0° by C_{2v} symmetry.
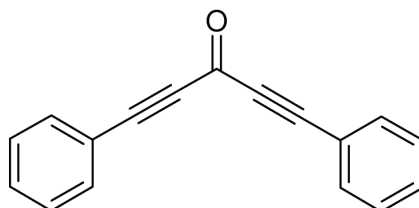
Figure 3.13: Schematic sketch of 1,5-Diphenylpenta-1,4-diyn-3-one (DPD).
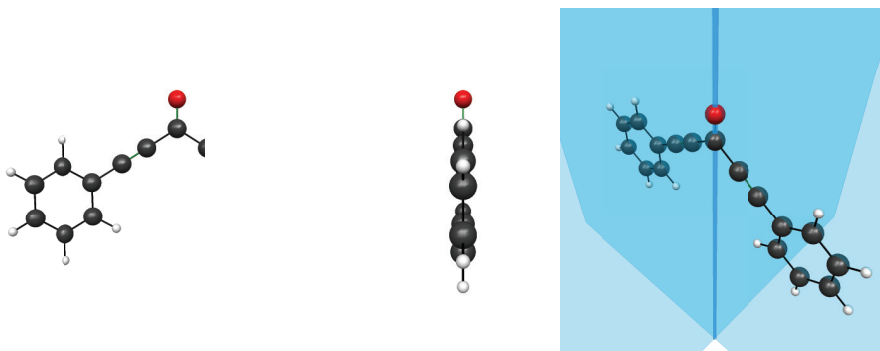
Figure 3.14: Front, side and diagonal views of the HF/cc-pVTZ optimized structure of DPD. The blue planes mark the mirror planes of the C_{2v} symmetry.

B3LYP generally predicts longer bonds that HF—with the exception of the single bonds, which are slightly shortened. In particular the carbonyl C–O bond is longer in the B3LYP geometry, by following the tendency from the benzophenone case. Table 3.8 compiles ^{1}H and ^{13}C NMR chemical shifts computed for both geometries with the GIAO method at the B3LYP/IGLO-II level. Also here similar tendencies as in the case of benzophenone are seen, all-over the HF-geometry yields lower deviations from the experiment with the exception of the carbonyl C.

Table 3.7: Some geometric data of DPD obtained from optimizations at the HF/cc-pVTZ and B3LYP/cc-pVTZ levels.

internal coordinate	HF geometry	B3LYP geometry
O=C	1.185 Å	1.220 Å
C≡C	1.185 Å	1.208 Å
C^{carb}–C≡	1.454 Å	1.442 Å
≡C–C^{ar}	1.436 Å	1.420 Å
C^i–C^o	1.389 Å	1.404 Å
C^o–C^m	1.379 Å	1.386 Å
C^m–C^p	1.383 Å	1.392 Å
O=C – phenyl ring	0.0°	0.0°

Table 3.8: NMR chemical shifts of ^{1}H and ^{13}C for DPD, measured values in d-chloroform taken from [43].

	experiment	calculated values	
		HF geometry	B3LYP geometry
aryl H^m and H^p	7.34–7.58	7.26(H^m) / 7.65(H^p)	7.48(H^m) / 7.54(H^p)
aryl H^o	7.59–7.77	7.54 / 7.55	7.79 / 7.82
C=O	160.80	156.85	163.57
aryl C^o	133.35	137.91 / 139.15	141.71 / 142.83
aryl C^m	128.72	131.96 / 132.31	133.99 / 134.38
aryl C^p	131.27	134.32	136.88
aryl C^i	119.42	125.47	127.56
phen–C≡	91.68	89.66	93.24
≡C–carb	89.42	93.55	97.35
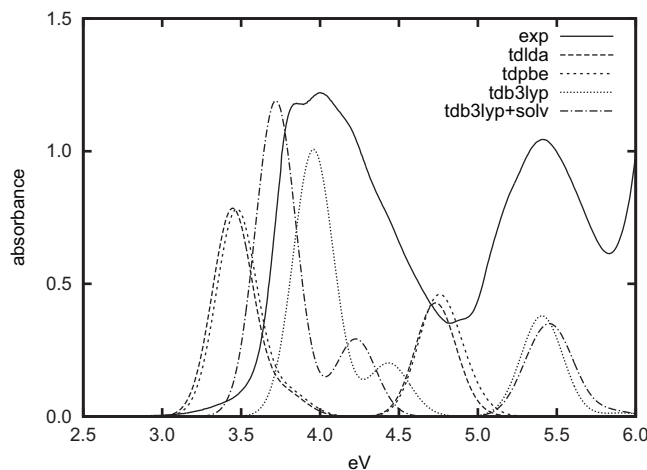
Figure 3.15: Experimental and TDDFT spectra of DPD (HF-optimized). Experimental line was obtained at a concentration of 5×10^{-5} mol L^{-1} in acetonitrile [51].

Ground State Properties and Neutral Excitations

Electronic ground state properties and excitations were computed mostly for the HF/cc-pVTZ symmetry in C_{2v} symmetry. As for benzophenone DFT and TDDFT results were obtained for LDA, PBE and B3LYP functionals. To learn about the influence of geometric differences, excitations from TDB3LYP are compared for both, the HF- and the B3LYP-optimized structures. Excitation energies, oscillator strengths and orbital assignments are compiled for all functionals in Table 3.9, KS orbitals from LDA are depicted in Figure 3.16 and from B3LYP in Figure 3.17. The 15 lowest excitation energies[9] and oscillator strengths are combined in the simulated spectrum (Gaussians broadened by 0.4 eV) in Figure 3.15.

Comparing the TDLDA and TDPBE results one finds that they differ only marginally and GGA does not improve substantially over LDA. Note that the first transition of symmetry A_2 is symmetry forbidden and hardly observed in the experiment[10]. The picture changes significantly when going to the B3LYP hybrid functional. The finding for benzophenone of a general shift in excitation energies due to hybrid mixing in the functional applies also here, all transitions are shifted by 0.5–0.7 eV from their LDA/GGA counterparts. This leads to a better, if not excellent agreement with the experimental energies. Note though that the comparison with the low resolution spectra taken in solution might be misleading somewhat. At most this comparison could be made for the results in

---

[9]Highest included excitations were at 4.9 eV for TDLDA and TDPBE, 5.9 eV for TDB3LYP and 6.0 eV for TDB3LYP/PCM.

[10]Pucher et al. [52] do report a weak band of $\varepsilon \approx 100$ M^{-1} cm^{-1} at 3.1 eV that exhibits a hypsochromic shift.

Table 3.9: Important TDDFT excitations for DPD along with their major contributions of KS orbital transitions.

state	energy (eV)	sym	osc. str.	major contributions		
				origin	target	percent
			TDLDA [a]			
1	3.05	A_2	0.000	HOMO	LUMO	94
2	3.45	B_2	0.583	HOMO$-$1	LUMO	85
3	3.78	A_1	0.019	HOMO$-$4	LUMO	40
				HOMO$-$2	LUMO	39
11	4.73	B_2	0.305	HOMO$-$2	LUMO+1	77
			TDPBE [a]			
1	3.11	A_2	0.000	HOMO	LUMO	95
2	3.47	B_2	0.581	HOMO$-$1	LUMO	86
3	3.80	A_1	0.053	HOMO$-$2	LUMO	67
11	4.74	B_2	0.311	HOMO$-$2	LUMO+1	79
			TDB3LYP(VWN5) [a]			
1	3.64	A_2	0.000	HOMO$-$2	LUMO	89
2	3.96	B_2	0.750	HOMO	LUMO	90
4	4.43	A_1	0.138	HOMO$-$1	LUMO	84
8	5.36	A_1	0.112	HOMO	LUMO+1	81
11	5.43	B_2	0.168	HOMO$-$1	LUMO+1	86
			TDB3LYP(VWN5) [b]			
1	3.34	A_2	0.000	HOMO$-$2	LUMO	90
2	3.72	B_2	0.771	HOMO	LUMO	89
4	4.21	A_1	0.143	HOMO$-$1	LUMO	82
8	5.15	A_1	0.121	HOMO	LUMO+1	79
10	5.22	B_2	0.160	HOMO$-$1	LUMO+1	86
			TDB3LYP(VWN1) in PCM acetonitrile [a]			
1	3.78	A_2	0.000	HOMO$-$4	LUMO	88
2	3.79	B_2	0.859	HOMO	LUMO	90
5	4.32	A_1	0.018	HOMO$-$1	LUMO	92
8	5.37	A_1	0.131	HOMO	LUMO+1	82
11	5.49	B_2	0.167	HOMO$-$1	LUMO+1	82
			experiment, MeCN [43] [c]			
	3.83		21.6*			
	3.99		22.4*			
	5.41		19.0*			
			experiment [52] [d]			
	≈ 3.1		$\approx 0.1^*$			
	3.91			n-hexane		
	3.85		25.0*	MeCN		

[a] computed for the HF/cc-pVTZ-optimized geometry; [b] computed for the B3LYP/cc-pVTZ-optimized geometry; [c] the first two maxima build one band in the low resolution spectrum, their energies in benzene are 3.80 and 3.99 and in MeOH 3.87 and 4.03 [43]; [d] first vibronic transitions; osc. str. = oscillator strength; * max. extinction coefficient $\times 10^{-3}$ L mol^{-1} cm^{-1}.

97

LUMO+1 LUMO+2 LUMO+3

HOMO−1 HOMO LUMO

HOMO−4   HOMO−3   HOMO−2
$\epsilon = -7.02$ eV $\epsilon = -7.02$ eV $\epsilon = -6.61$ eV
B_1 B_2 B_1

Figure 3.16: LDA/cc-pVTZ KS orbitals for DPD (HF-optimized). Underneath the orbital specification ϵ refers to the KS eigenvalue and its symmetry, the contour value for the plot was 0.05.

LUMO+1   LUMO+2   LUMO+3

HOMO−1   HOMO   LUMO

HOMO−4
$\epsilon = -7.46$ eV
A_2

HOMO−3
$\epsilon = -7.46$ eV
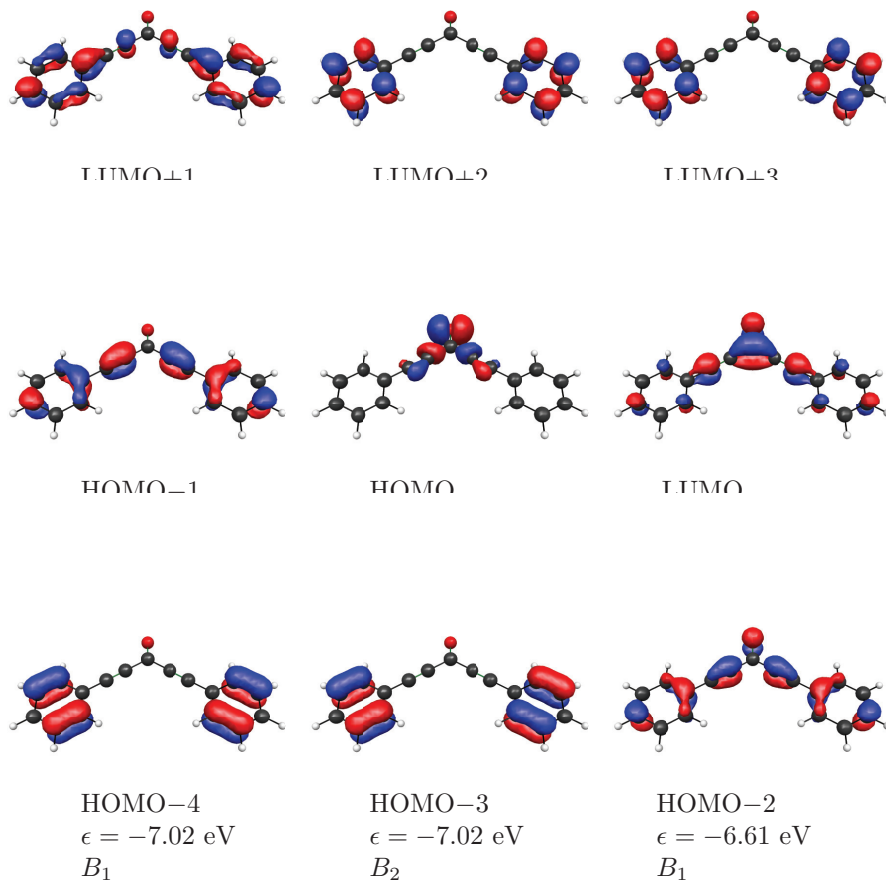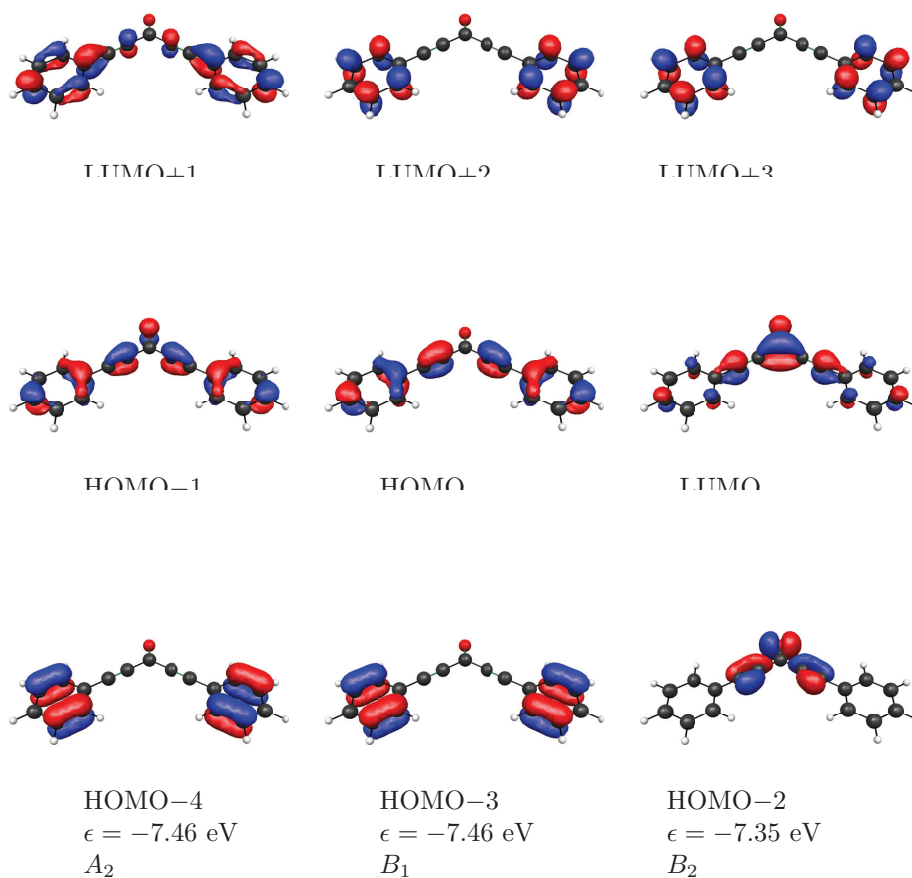B_1

HOMO−2
$\epsilon = -7.35$ eV
B_2

Figure 3.17: B3LYP/cc-pVTZ KS orbitals for DPD (HF-optimized). Underneath the orbital specification ϵ refers to the KS eigenvalue and its symmetry, the contour value for the plot was 0.05.

PCM acetonitrile (MeCN)—which still agree well with the experiments. Recall also from the benzophenone case that the hybrid functional deteriorated the excitation energy for the lowest $n_O \rightarrow \pi^*$ transition.

All TDDFT approximations predict the lowest strong transition to be of $\pi \rightarrow \pi^*$ character (note the orbital reordering between LDA and B3LYP). Whereas the $n_O \rightarrow \pi^*$ transition is symmetry forbidden and easily obscured experimentally. The practical importance of this finding lies in the fact that for both transition types electron transfer occurs, but only the $n_O \rightarrow \pi^*$ type transitions are efficient in hydrogen abstraction for the photoinitiation process. In [43] it was deduced from a small hypsochromic shift, that the strong band with maxima at 3.83 and 3.99 eV is of $n_O \rightarrow \pi^*$ character, a conclusion that is not supported by TDDFT. Contrary Pucher et al. [52] assign a $\pi \rightarrow \pi^*$ to the strong absorption band and find the weak $n_O \rightarrow \pi^*$ band by "closer inspection", in accordance with this work.

To learn more about the excitations in DPD CASSCF(6,5)/cc-pVTZ calculations for ground and excited states were done for the HF-optimized geometry. The CAS space consisted of 6 electrons in 5 orbitals. The starting orbitals for the CASSCF were chosen to be 3 occupied HF orbitals: in addition to the two highest occupied HF orbitals, a lower lying orbital was rotated into the CAS space to ensure some n_O character in addition to π-orbitals, similar to the B3LYP orbital space in Figure 3.17. The unoccupied orbitals were just the 2 lowest unoccupied HF orbitals. Everything was done in cc-pVTZ basis. The resulting orbitals and net occupation numbers of the active space are depicted in Figure 3.18.

The ground state orbitals are obtained roughly similar to the DFT orbitals. In the lowest state in B_2 symmetry about one electron charge is transferred from a π to a π^*-type anti-bonding orbital, while the $n_O \rightarrow \pi^*$ character of the transition from ground into the $S_1(A_2)$ state is also found with CASSCF. The obtained dipole moments μ in Debye are

state	μ_x	μ_y	μ_z
S_1 (A_1)	0.00	0.00	-4.73
S_1 (A_2)	0.00	0.00	-1.63
S_1 (B_2)	0.00	0.00	-8.15

(3.76)

where z-axis is the C_2 torisonal axis (z^+ heading up in Figure 3.14) and the x- and y-axes lie in the mirror planes. Hence the dipole vector lies in the carbonyl axis and heads "downwards" (referring again to Figure 3.14). Note the large increase in the dipole moment for the transition to the $S_1(B_2)$ state, which is connected to an electron transferred from a π-orbital delocalized over the whole molecule. This explains also the good performance of the hybrid functional in contrast to TDLDA for the two $\pi \rightarrow \pi^*$ transitions—due to its partly non-local character—and the substantial corrections of GW_f-BSE on TDLDA below. The transition to the $S_1(A_2)$ state triggers a stiff decrease in transition moment, due to a charge adjustment in the carbonyl group. The transition is at the same time predicted to be rather localized on >C=O. This finding is consistent with the much better performance of TDLDA and TDGGA in case of the $n_O \rightarrow \pi^*$ transition. The hybrid functional seems to introduce here a spurious shift, which is not found from solving the BSE.
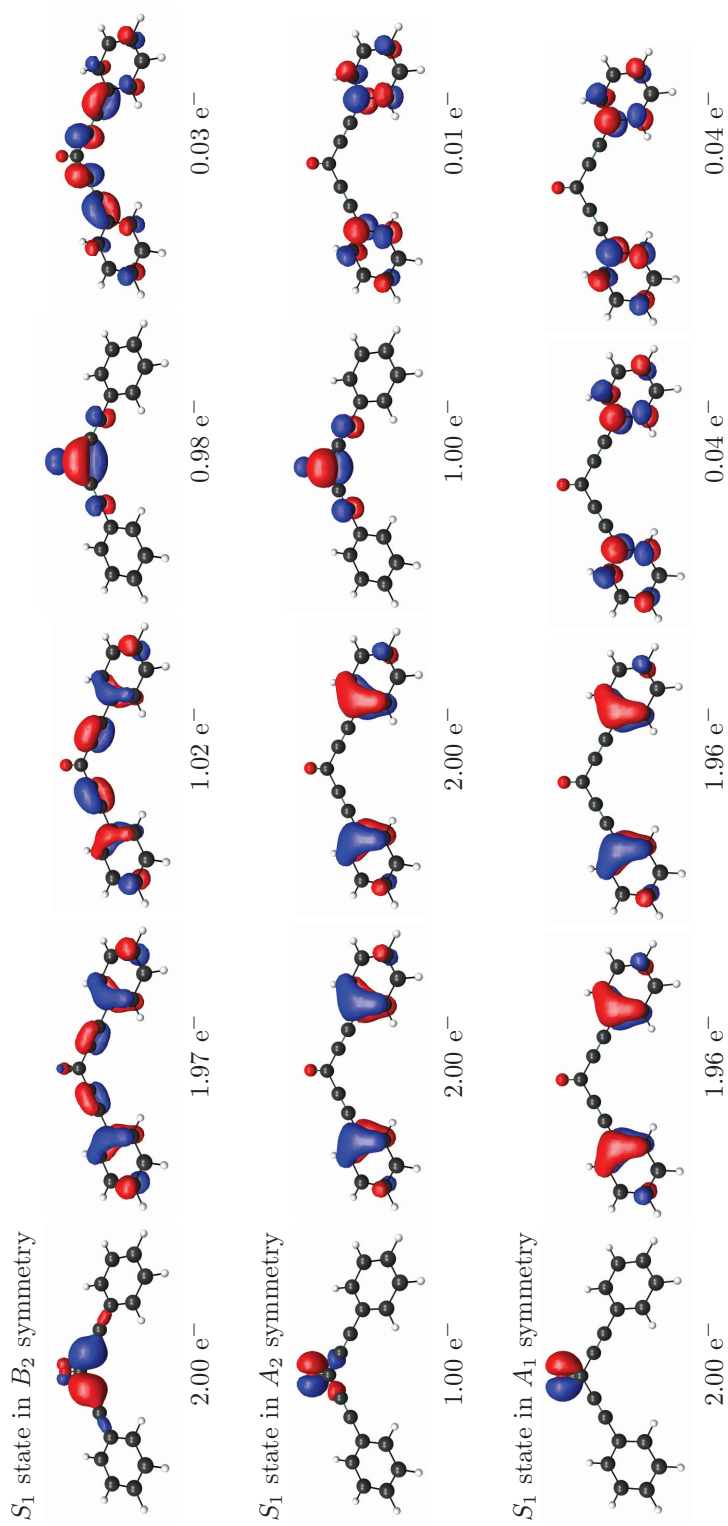
Figure 3.18: Principal origin and target CASSCF(6,5)/cc-pVTZ orbitals for the ground, $S_1(A_2)$ and $S_1(B_2)$ states of DPD (HF-optimized). All orbitals in the active space are depicted, along with their electron occupation underneath. The contour value for the plot was 0.05.

S_1 state in B_2 symmetry

2.00 e$^-$ 1.97 e$^-$ 1.02 e$^-$ 0.98 e$^-$ 0.03 e$^-$

S_1 state in A_2 symmetry

1.00 e$^-$ 2.00 e$^-$ 2.00 e$^-$ 1.00 e$^-$ 0.01 e$^-$

S_1 state in A_1 symmetry

2.00 e$^-$ 1.96 e$^-$ 1.96 e$^-$ 0.04 e$^-$ 0.04 e$^-$
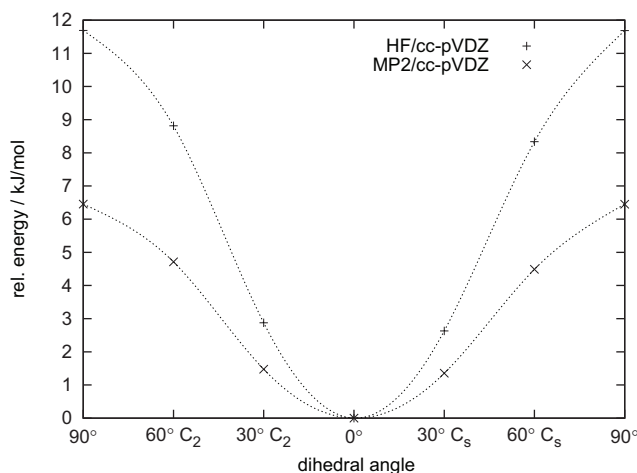
Figure 3.19: Electronic energies of non-planar DPD structures in C_2 and C_s symmetries from HF/cc-pVDZ and MP2/cc-pVDZ, relative to the planar structure in kJ mol^{-1}. The abscissa means dihedral angle between keto and phenyl planes.

But there is more about this. Up to now all calculations were done for the C_{2v} planar structure of DPD, which is the minimum on both the HF and B3LYP hypersurface. But that does not mean that only this stucture is present at room temperature. Figure 3.19 shows the relative electronic energies (without any vibrational contributions) when twisting the phenyl rings out of the molecular plane. This is possible in two ways, either in opposite directions in a C_2 symmetry (conserving a C_2 axis) or in like directions in a C_s symmetry (conserving a mirror plane σ)[11]. Energies from HF/cc-pVDZ and MP2/cc-pVDZ in Figure 3.19 show little difference between the two symmetries. But they also show that the energy barrier of the phenyl torison is rather low (6.45 kJ mol^{-1} by MP2/cc-pVDZ). Hence there is a significant portion of DPD present whose phenyl rings are twisted out of the molecular plane. This twist breaks the C_{2v} symmetry and allows the former A_2 transition of $n_O \rightarrow \pi^*$ character[12]. This process may explain the fair activity of DPD as a photoinitiator. In the experimental spectrum of DPD the transition could be causing the "foot" at the low energy side of the broad band, although this assignment is somewhat speculative.

GW_f and BSE calculations were also done for the HF/cc-pVTZ structure of DPD. Similar to benzophenone, the molecule was set into a spherical box of now 10.0 Å radius and a grid spacing of 0.20 Å was used to reach a comparable accuracy. For the excitations and self energy parts of the method a total of 800 states (42 occupied and 758 virtual states) was used. The TDLDA sum rule was thereby fulfilled to 72%. Quasiparticle orbitals are shown in Figure 3.20 and resemble closely the B3LYP orbital shape and order. As in the benzophenone

---

[11]The structure with phenyl rings perpendicular to the molecular plane posesses again C_{2v} symmetry.

[12]This situation is frequently seen and responsible for the finite absorption of symmetry forbidden transitions. For a general discussion of these phenomena see e.g. Herzberg [53].

LUMO+1
$\epsilon = -0.38$ eV
A_2, $c = 0.03$

LUMO+2
$\epsilon = 0.17$ eV
B_1, $c = 0.03$

LUMO+3
$\epsilon = 0.18$ eV
A_2, $c = 0.03$

HOMO-1
$\epsilon = -8.91$ eV
B_1, $c = 0.04$

HOMO
$\epsilon = -8.69$ eV
A_2, $c = 0.03$

LUMO
$\epsilon = -1.83$ eV
B_1, $c = 0.07$

HOMO-4
$\epsilon = -9.24$ eV
B_1, $c = 0.03$

HOMO-3
$\epsilon = -9.24$ eV
A_2, $c = 0.03$

HOMO-2
$\epsilon = -9.20$ eV
B_2, $c = 0.10$
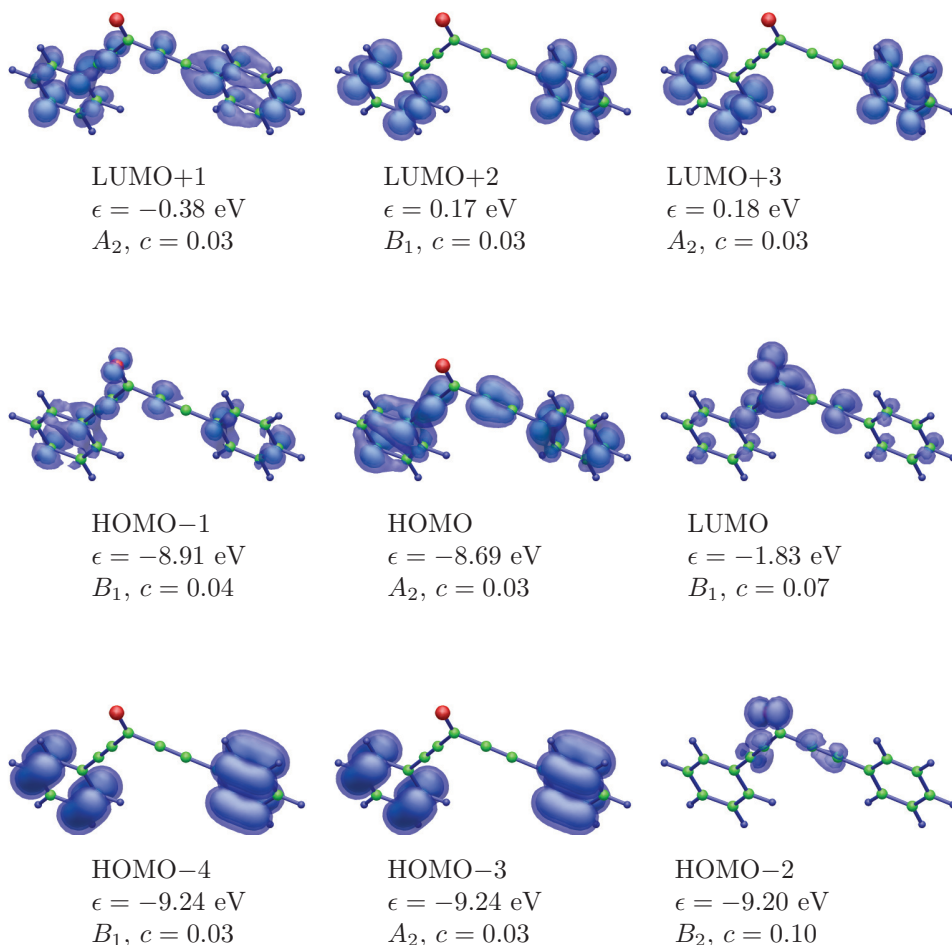
Figure 3.20: Quasiparticle orbitals for DPD (HF-optimized). Underneath the orbital specification the eigenvalues ϵ, symmetries and the plot's contour values c are given.

case, HOMO eigenvalues are changed significantly from -6.26 eV (LDA) and -6.83 eV (B3LYP) to -8.69 eV (GW_f).

Excitation energies and oscillator strengths from Parsec/RGWBS codes for the Random Phase Approximation (RPA), TDLDA and GW_f-BSE levels of approximation are presented in Table 3.10. The comparably crude RPA yields excitation energies which deviate substantially from the other levels of theory and the experiment (note once more the limited comparability of the experimental spectra), in particular for higher excitations. The lowest A_2 transition is comparable to TDLDA and—interestingly—in good agreement with BSE. The TDLDA case was discussed already above. The slight deviations from the GAMESS results stem from the different technical realization (real space and PPs vs. Gaussian basis), where both introduce their own errors.

Excitation energies obtained from BSE exhibit once more similarities to

Table 3.10: Lowest significant RPA, TDLDA and GW_f-BSE excitations for DPD (HF-optimized) from PARSEC/RGWBS codes.

RPA			TDLDA			GW_f-BSE		
energy	osc.	sym	energy	osc.	sym	energy	osc.	sym
2.91	0.000	A_2	3.10	0.000	A_2	2.78	0.000	A_2
3.05	1.150	B_2	3.41	0.602	B_2	3.59	1.011	B_2
3.23	0.523	A_1	3.76	0.065	A_1	4.26	0.049	A_1
4.25	0.275	A_1	4.73	0.286	B_2	5.44	0.020	B_2
4.44	0.482	B_2	4.89	0.123	A_1			
experiment, MeCN [43] [a]								
			3.83	21.6*				
			3.99	22.4*				
			5.41	19.0*				
experiment [52] [b]								
			3.91	n-hexane				
			3.85	MeCN				

[a] the first two maxima build one band in the low resolution spectrum, their energies in benzene are 3.80 and 3.99 and in MeOH 3.87 and 4.03; [b] first vibronic transitions; osc. str. = oscillator strength; * max. extinction coefficient $\times 10^{-3}$ L mol^{-1} cm^{-1}.

the benzophenone case. The lowest $n_O \rightarrow \pi^*$ transition is further lowered, compared to TDLDA, but unfortunately there is no experimental reference to decide whether this is an improvement or not. The intensive $\pi \rightarrow \pi^*$ band is shifted slightly and in relatively good agreement with TDB3LYP and the experimental measurements. Higher excitations are corrected further to higher energies, again in agreement with TDB3LYP and the experiments. The primary difference to these two values is the much weaker oscillator strength. Simulated spectra of all excitations as above are again shown in Figure 3.21.
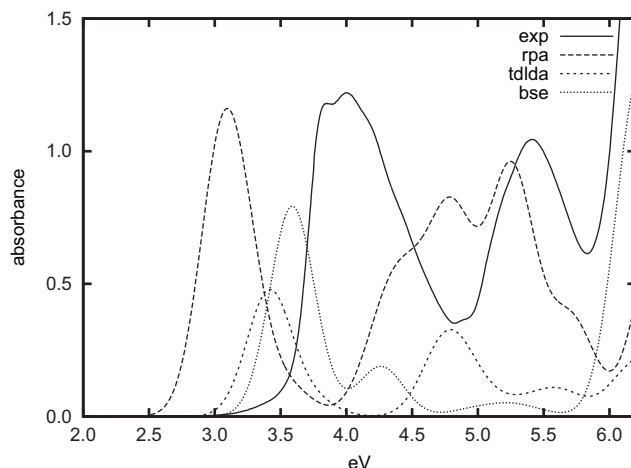
Figure 3.21: RPA, TDLDA, GW_f-BSE and experimental spectra of DPD, Gaussian broadened by 0.4 eV. Experimental parameters are the same as above [51].

3.2.3 Derivatives of DPD

1,5-Bis(4-methoxyphenyl)penta-1,4-diyn-3-one (ODPD) and 1,5-Bis(4-(thiomethyl)phenyl)penta-1,4-diyn-3-one (SDPD)

The structures of ODPD and SDPD, Figure 3.22, are even more flexible as in the case of DPD. Several internal coordinates are expected to have low barriers for a twist or flip: the phenyl–keto dihedral angle like for DPD, the position of the methyl group relative to the phenyl ring and the torsion of the methyl H atoms.

The structures were determined at the HF/cc-pVTZ level with a gradient convergence tolerance of 10^{-5} H Bohr^{-1}. For ODPD two local minima were studied in this work for comparison: one with planar phenyl rings and dihedral angles C^3–C^i–X–C^{mex} of 0° (mex = methoxy or thiomethyl, with X = O or S; i.e. methyl groups head "up"), which is presumably the global minimum, and a second one with the dihedral angle C^3–C^i–X–C^{mex} of 180° (i.e. methyl groups head "down"). The latter structure has an HF/cc-pVTZ electronic energy of 0.77 kJ mol^{-1} above the former and shall be named "twisted" ODPD (ODPDt) henceforth. Data for the obtained geometries are compiled in Table 3.11, both were obtained in C_{2v} symmetry. Also for SDPD a structure with C^3–C^i–X–C^{mex} of 0° and a twisted SDPD structure with an angle of 180° are local minima, the latter 0.77 kJ mol^{-1} higher in HF/cc-pVTZ electronic energy. The optical properties of the two are approximately the same, similar to the case of ODPD (see below). Therefore only the "non-twisted" structure was studied in greater detail. Additionally, a local minimum in C_2 symmetry with thiomethyl groups twisted against the phenyl ring by roughly 90° was found, but this was 28.02 kJ mol^{-1} higher than the C_{2v} symmetry and was not studied further. Pictures of

105

the optimized ("non-twisted") ODPD and SDPD structures are shown in Figure
3.23. As before, computed ^{1}H and ^{13}C NMR chemical shifts for HF/cc-pVTZ
geometries at the GIAO B3LYP/IGLO-II level are compared with experimental
values in Table 3.12.
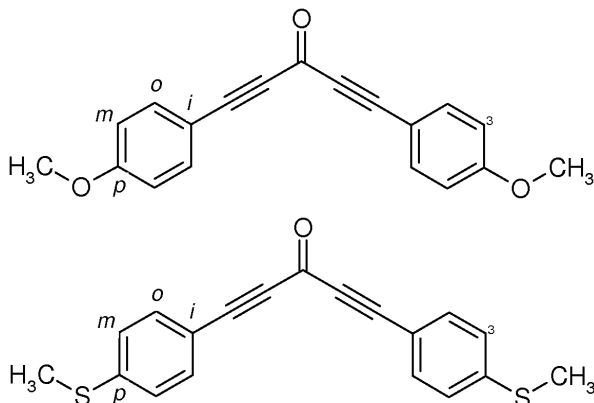
Figure 3.22: Schematic sketches of ODPD and SDPD. The number refers to the ge-
ometry definitions.

Table 3.11: Structure data of HF/cc-pVTZ-optimized structures for ODPD, ODPDt
and SDPD.

internal coord	ODPD	ODPDt	SDPD
O=C	1.186 Å	1.186 Å	1.185 Å
C≡C	1.186 Å	1.186 Å	1.185 Å
C^{carb}–C≡	1.452 Å	1.452 Å	1.453 Å
≡C–C^{ar}	1.432 Å	1.432 Å	1.433 Å
O=C – phenyl ring	0.0°	0.0°	0.0°
C^i–C^o	1.383^a; 1.395^b Å	1.396^a; 1.383^b Å	1.385^a; 1.392^b Å
C^o–C^m	1.383^a; 1.369^b Å	1.369^a; 1.383^b Å	1.381^a; 1.372^b Å
C^m–C^p	1.385^a; 1.393^b Å	1.393^a; 1.385^b Å	1.385^a; 1.393^b Å
C^p–X	1.337 Å	1.337 Å	1.763 Å
X–C^{mex}	1.399 Å	1.399 Å	1.798 Å
C^p–X–C^{mex}	120.3°	120.3°	104.6°
C^3–C^p–X–C^{mex}	0.0°	180.0°	0.0°

^{a} data for the "upper side" of the phenyl rings (i.e. C^m = C^3, $C^{3'}$ in Figure 3.22); ^{b} data for
the "lower side" of the phenyl ring (*not* including C^3, $C^{3'}$).

Neutral electronic excitations of ODPD were computed using TDLDA and
TDB3LYP levels in cc-pVTZ basis, and with TDB3LYP in combination with the
PCM model and UFF radii enlarged by a factor of 1.2 for the cavity, see Table
3.13. The general picture developed from the benzophenone and DPD cases
is also true here. The exception is that there are now two orbital forbidden
$n_O \rightarrow \pi^*$ type transitions of symmetry A_2, compare Table 3.13 with Figure

106
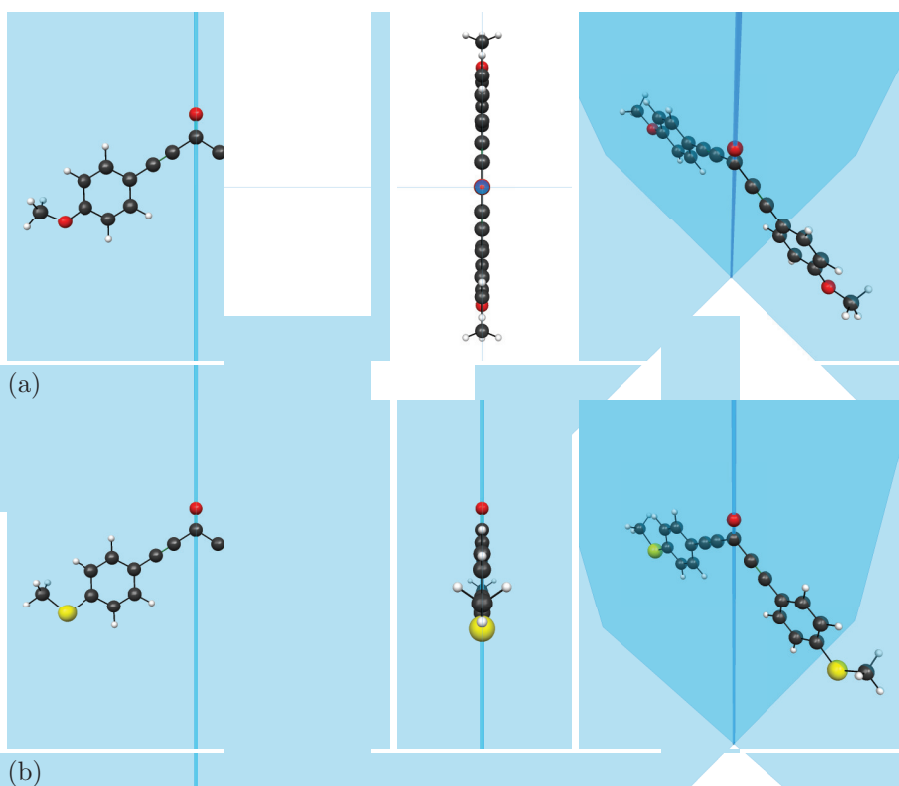
Figure 3.23: Front, top/side and diagonal views of the HF/cc-pVTZ optimized structures of (a) ODPD and (b) SDPD. The blue planes mark the mirror planes of the C_{2v} symmetry.

Table 3.12: Computed NMR chemical shifts of ^{1}H and ^{13}C for HF/cc-pVTZ optimized ODPD, ODPDt and SDPD, experimental values measured values in d-chloroform taken from [54].

		ODPD	ODPDt	SDPD	
	exp.	calc.	calc.	exp.	calc.
aryl H^o	7.61	7.39 / 7.47	7.41 / 7.45	7.55	7.29 / 7.42
aryl H^m	6.92	6.40 / 6.78	6.38 / 6.79	7.23	6.68 / 7.00
–XCH$_3$ H	3.86	3.33 / 3.81	3.32 / 3.81	2.51	1.83 / 2.13
C=O	162.0	156.54	153.45	160.6	156.31
aryl C^p	160.9	165.49	162.47	144.1	154.06
aryl C^o	135.4	139.45 / 141.15	136.82 / 137.67	133.6	123.63 / 128.24
aryl C^m	114.4	110.23 / 121.21	106.86 / 118.41	125.3	136.97 / 139.63
aryl C^i	111.4	116.39	113.46	115.1	119.43
phen–C≡	92.5	89.74	86.58	92.0	89.71
≡C–carb	89.7	93.75	90.76	90.1	94.09
–XCH$_3$ C	55.5	53.28	50.25	14.8	15.73

3.24 for LDA orbitals and Figure 3.25 for B3LYP orbitals. These excitations lie above the lowest $\pi \to \pi^*$ transition (which is state 1 in both, TDLDA and TDB3LYP). PCM shifts them even above the two lowest transitions of this type. This data stay in contrast to Pucher et al. [52] who report a weak $n_O \to \pi^*$ transition around 3.1 eV, *below* the strong $\pi \to \pi^*$ absorption band, where the assignment was done due to solvent shifts. As before, TDB3LYP shifts the TDLDA excitation energies by roughly 0.6 eV, and yields thereby energies partly above the experimental values (which are measured in solvents and are hence of limited comparability). PCM increases the $n_O \to \pi^*$ transitions and lowers $\pi \to \pi^*$, what is a plausible effect in good agreement with the experimental data. Simulated spectra[13] as before are shown in Figure 3.26.

The twisted ODPDt structure which is expected to have a significant Boltzmann weight due to its relative electronic energy does not cause much of a change. The excitations are not influenced significantly by the twist, see Table 3.13 and Figure 3.27[13], apart from flipping of closely lying states. Also the orbitals which are important for excitations are not affected significantly (not shown for this reason).

A similar picture can be drawn from Table 3.14 for SDPD, where the A_2 states are further shifted with respect to the lowest excitation. B3LYP orbitals are shown in Figure 3.28. Simulated spectra[13] are given in Figure 3.29, where the broadening was reduced to 0.3 eV for better comparability with the experimental spectrum in MeCN.

---

[13]Including the 15 lowest excitations. Highest excitation energies are for ODPD: 4.6 eV (TDLDA), 5.6 eV (TDB3LYP) and 5.5 eV (TDB3LYP/PCM); for ODPDt: 5.6 eV (TDB3LYP); for SDPD: 4.3 eV (TDLDA), 5.5 eV (TDB3YP) and 5.1 eV (TDB3LYP/PCM).

Table 3.13: Lowest important TDDFT excitations from GAMESS for ODPD along with the major contributions of KS orbital transitions.

state	energy (eV)	sym	osc. str.	major contributions		
				origin	target	percent
			TDLDA for ODPD			
1	3.05	B_2	0.725	HOMO	LUMO	86
2	3.14	A_2	0.000	HOMO−2	LUMO	94
3	3.34	A_1	0.058	HOMO−1	LUMO	72
4	3.94	A_2	0.000	HOMO−3	LUMO	98
12	4.42	B_2	0.385	HOMO−1	LUMO+1	54
			TDB3LYP(VWN5) for ODPD			
1	3.65	B_2	0.953	HOMO	LUMO	90
2	3.71	A_2	0.000	HOMO−2	LUMO	90
3	4.08	A_1	0.725	HOMO−1	LUMO	85
4	4.46	A_2	0.000	HOMO−5	LUMO	92
10	5.18	A_1	0.199	HOMO	LUMO+3	43
11	5.19	B_2	0.308	HOMO−1	LUMO+1	83
			TDB3LYP(VWN5) for ODPDt			
1	3.65	B_2	0.855	HOMO	LUMO	91
2	3.71	A_2	0.000	HOMO−2	LUMO	90
3	4.08	A_1	0.181	HOMO−1	LUMO	85
4	4.46	A_2	0.000	HOMO−5	LUMO	92
8	5.11	A_1	0.215	HOMO	LUMO+1	61
11	5.19	B_2	0.156	HOMO−1	LUMO+1	83
			TDB3LYP(VWN1) in MeCN (PCM) for ODPD			
1	3.34	B_2	1.077	HOMO	LUMO	46
2	3.80	A_1	0.176	HOMO−1	LUMO	44
3	3.93	A_2	0.000	HOMO−4	LUMO	44
6	4.52	A_2	0.000	HOMO−5	LUMO	44
10	5.12	A_1	0.229			
11	5.17	B_2	0.307	HOMO−1	LUMO+1	33
			exp in MeCN [54]			
	3.51		24.7 [a]			
	5.18		17.7 [a]			
			exp [52]			
	≈ 3.1		≈ 0.1 [a]			
	3.63			n-hexane		
	3.50		32.0 [a]	MeCN		

osc. str. = oscillator strength; [a] max. extinction coefficient $\times 10^{-3}$ M^{-1} cm^{-1}.

LUMO+3
$\epsilon = -0.75$ eV

LUMO+4
$\epsilon = -0.50$ eV

LUMO+5
$\epsilon = 0.25$ eV

LUMO
$\epsilon = -2.94$ eV

LUMO+1
$\epsilon = -1.74$ eV

LUMO+2
$\epsilon = -1.65$ eV

HOMO−2
$\epsilon = -5.92$ eV

HOMO−1
$\epsilon = -5.83$ eV

HOMO
$\epsilon = -5.66$ eV

HOMO−5
$\epsilon = -6.91$ eV

HOMO−4
$\epsilon = -6.91$ eV

HOMO−3
$\epsilon = -6.83$ eV

Figure 3.24: LDA KS orbitals for ODPD from GAMESS. Underneath the orbital specification ϵ refers to the KS eigenvalue, the contour value for the plot was 0.05.

LUMO+1   LUMO+2   LUMO+3

HOMO−1   HOMO   LUMO

HOMO−4   HOMO−3   HOMO−2

HOMO−7
$\epsilon = -8.11$ eV
A_2

HOMO−6
$\epsilon = -8.08$ eV
B_1

HOMO−5
$\epsilon = -7.67$ eV
B_2

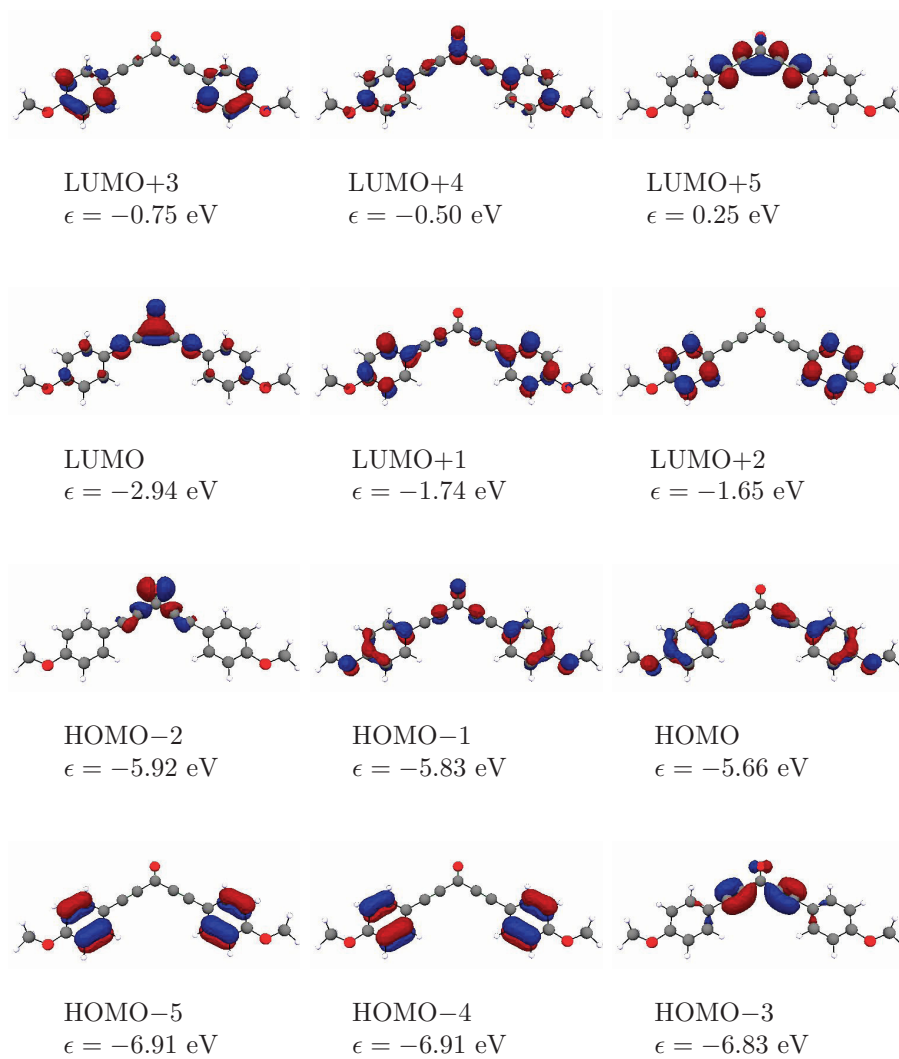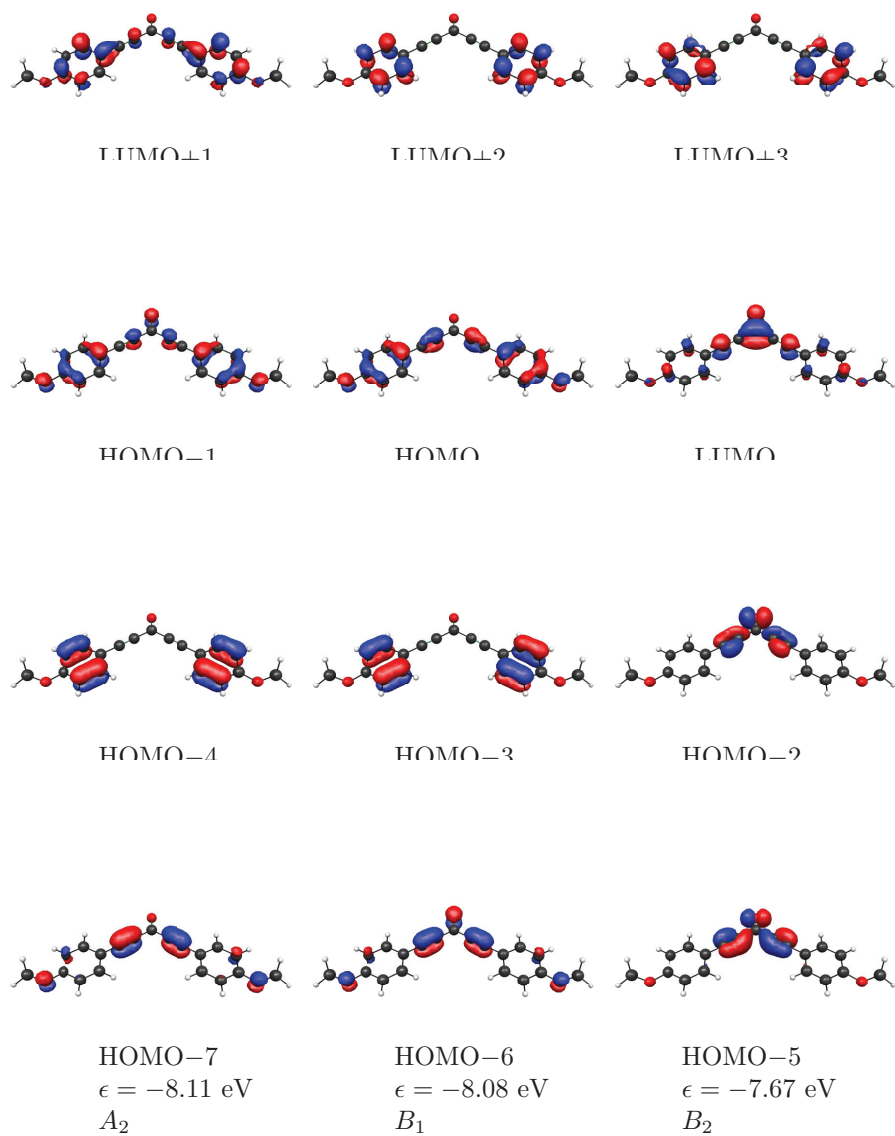Figure 3.25: B3LYP/cc-pVTZ KS orbitals for ODPD from GAMESS. Underneath the orbital specification ϵ refers to the KS eigenvalue, the contour value for the plot was 0.05.
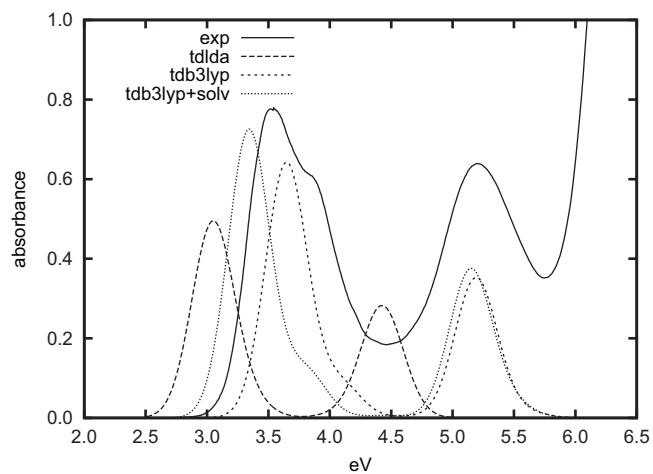
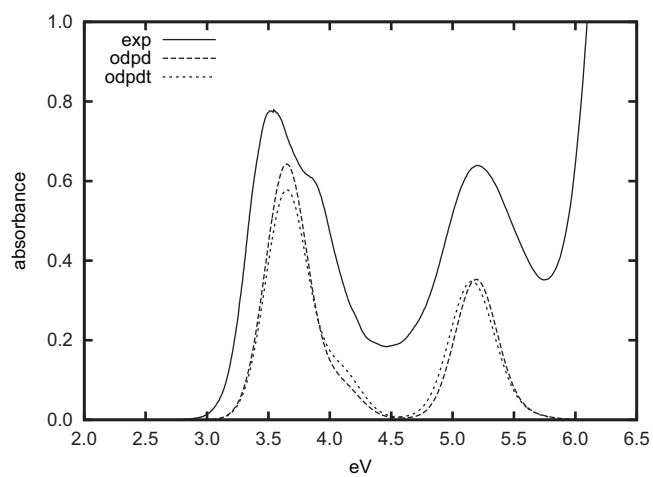Figure 3.26: Experimental [51] and theoretical spectra of ODPD.

Figure 3.27: TDB3LYP(VWN5) spectra of ODPD and twisted ODPD*t* along with experimental spectrum (red, solid) [51].

Table 3.14: Lowest important TDDFT excitations from GAMESS for SDPD along with their major assignments to KS orbital transitions.

state	energy (eV)	sym	osc. str.	major contributions		
				origin	target	percent
TDLDA						
1	2.60	B_2	0.725	HOMO	LUMO	87
2	2.79	A_1	0.051	HOMO−1	LUMO	77
3	3.07	A_2	0.000	HOMO−2	LUMO	94
4	3.81	B_2	0.355	HOMO−1	LUMO+1	68
8	3.88	A_2	0.000	HOMO−4	LUMO	98
12	4.04	B_2	0.201	HOMO−3	LUMO	71
TDB3LYP(VWN5)						
1	3.32	B_2	0.946	HOMO	LUMO	92
2	3.63	A_1	0.118	HOMO−1	LUMO	88
3	3.67	A_2	0.000	HOMO−2	LUMO	89
4	4.41	A_2	0.000	HOMO−7	LUMO	92
7	4.61	A_1	0.110	HOMO	LUMO+1	82
8	4.64	B_2	0.440	HOMO−1	LUMO+1	80
10	4.90	A_1	0.101	HOMO−4	LUMO	63
TDB3LYP(VWN1) in MeCN (PCM)						
1	3.04	B_2	1.056	HOMO	LUMO	46
2	3.36	A_1	0.163	HOMO−1	LUMO	45
3	3.88	A_2	0.000	HOMO−4	LUMO	44
6	4.47	A_2	0.000	HOMO−7	LUMO	44
7	4.53	A_1	0.112	HOMO	LUMO+1	44
8	4.57	B_2	0.483	HOMO−5	LUMO	25
				HOMO−1	LUMO+1	22
10	4.75	A_1	0.118			
exp in MeCN [54]						
	3.31		35.8 [a]			
	4.94		20.6 [a]			

osc. str. = oscillator strength; [a] max. extinction coefficient $\times 10^{-3}$ M^{-1} cm^{-1}.

LUMO
$\epsilon = -2.23$ eV
B_1

LUMO+1
$\epsilon = -1.06$ eV
A_2

HOMO−1
$\epsilon = -6.04$ eV
B_1

HOMO
$\epsilon = -5.93$ eV
A_2

HOMO−3
$\epsilon = -7.81$ eV
A_2

HOMO−2
$\epsilon = -7.18$ eV
B_2

HOMO−7
$\epsilon = -0.71$ eV
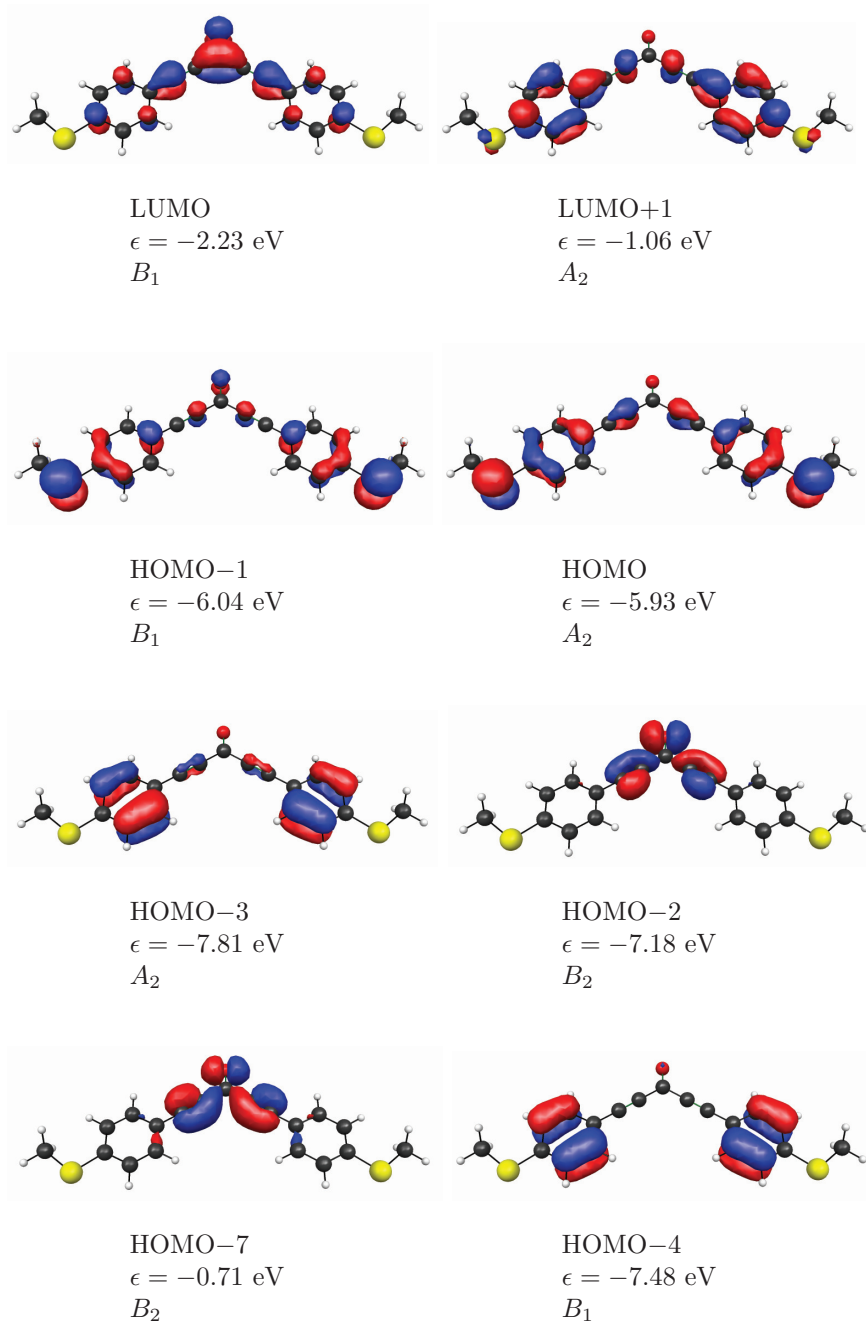B_2

HOMO−4
$\epsilon = -7.48$ eV
B_1

Figure 3.28: B3LYP/cc-pVTZ KS orbitals for SDPD. Underneath the orbital specification ϵ refers to the KS eigenvalue, the contour value for the plot was 0.04.
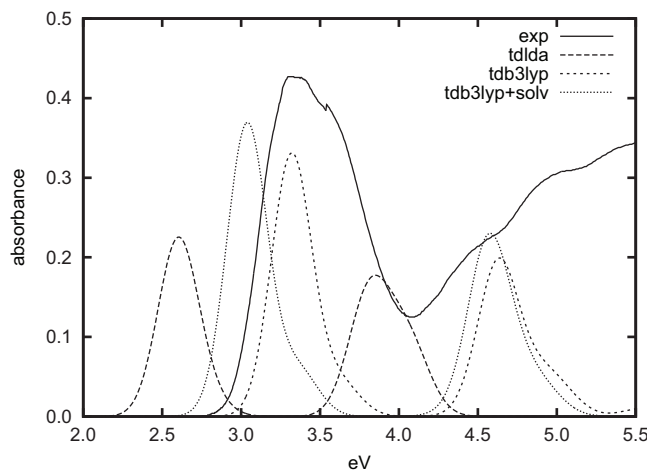
Figure 3.29: Experimental and TDDFT spectra of SDPD. The theoretical lines are broadened by 0.3 eV, experimental spectrum was taken at 1.25×10^{-5} M in acetonitrile [51].

1,5-Bis(4-(dimethylamino)phenyl)penta-1,4-diyn-3-one (NDPD)

The structure of NDPD, whose schematic sketch is depicted in Figure 3.30, was optimized on the HF/cc-pVTZ hypersurface to a threshold of 10^{-5} H bohr^{-1}. A C_2 symmetry was imposed in the search, what allowed the –N(CH$_3$)$_2$ groups to twist against the phenyl ring plane. The final structure, which is shown in Figure 3.31, posesses only weakly pyramidalized amino groups (4°, while e.g. ammonia has about 40°) which lie approximately in the ring planes. This position enables conjugation of the N lone pair with the π systems of phenyl ring and triple bond. A C_{2v} structure with methyl groups sticking out of the molecular plane was 24.99 kJ mol^{-1} higher in HF/cc-pVTZ electronic energy. The typical orbitals of the close-to-planar geometry with eigenfuntions extended over N, phenyl ring and triple bond (see Figure 3.32) are not found in the C_{2v} symmetry. Details of the C_2 geometry are presented in Table 3.15, ^{1}H and ^{13}C NMR chemical shifts from GIAO B3LYP/IGLO-II are compared to experimental values in Table 3.16. The C_{2v} geometry was not studied further.

Excitation properties were obtained from TDLDA and TDB3LYP on a well converged wave function (SCF criterion density change of 10^{-7}) with GAMESS and from TDB3LYP in combination with a PCM modelled MeCN solvent with Gaussian03. The most important excitations are compiled in Table 3.17, involved B3LYP orbitals are shown in Figure 3.32 and a simulated spectrum[14] is presented in Figure 3.33. For the latter a line width of 0.3 eV was again assumed. The TDPBE data referring to the line in the spectrum are omitted

---

[14]Covering the lowest 15 excitations. Highest included excitation energies are 4.2 eV (TDLDA), 5.3 eV(TDB3LYP) and 5.1 eV (TDB3LYP/PCM).
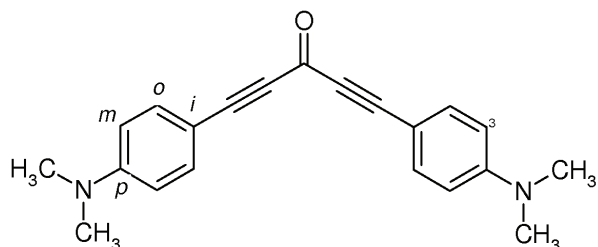
Figure 3.30: Schematic sketch of NDPD. The number and labels are used for geometric specifications below.
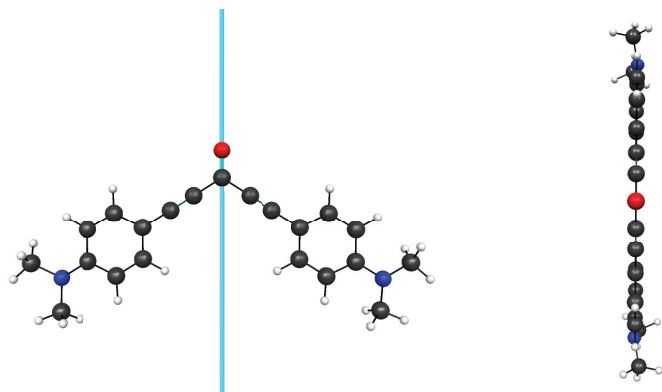
Figure 3.31: Front and top views of the HF/cc-pVTZ optimized structure of NDPD. The blue lines marks the rotation axes of the C_2 symmetry.

Table 3.15: Geometric data of the HF/cc-pVTZ-optimized structure of NDPD.

internal coord	value	internal coord	value
O=C	1.187 Å	C^o–C^m	1.374 Å^{a,b}
C≡C	1.187 Å	C^m–C^p	1.402 Å^{a,b}
C^{carb}–C≡	1.451 Å	C^p–N	1.374 Å
≡C–C^{ar}	1.430 Å	N–CH_3	1.445 Å^{a,b}
O=C – phenyl ring	0.2° ^{a}; 0.5° ^{b}	pyr ^{c}	4.0°
C^i–C^o	1.389^a; 1.388^b Å	C^m–C^p–N–CH_3	11.9° ^{a,b}

^{a} data for the "upper side" of the phenyl rings (including C^m = C^3, $C^{3'}$ in Figure 3.30); ^{b} data for the "lower side" of the phenyl ring (*not* including C^3, $C^{3'}$); ^{c} pyramidalization: $360° - \sum \angle(\text{C–N–C})$.

Table 3.16: ^{1}H and ^{13}C NMR chemical shifts for NDPD, measured values in d-chloroform taken from [54].

	exp	calc		exp	calc
aryl H^o	7.53	7.38 / 7.39	C=O	160.7	156.31
aryl H^m	6.64	6.35 / 6.37	aryl C^p	151.8	154.16
–NMe$_2$ H	3.04	2.35 / 2.37	aryl C^m	135.3	113.88 / 113.46
		2.56 / 2.57	aryl C^o	111.5	140.36 / 139.21
		3.06 / 3.07	aryl C^i	105.3	112.58
			phen–C≡	95.1	90.56
			≡C–carb	91.1	94.45
			–NMe$_2$ C	39.9	40.76 / 40.91

from Table 3.17 because they closely resemble TDLDA. The general picture developed in the previous cases is once more valid. TDLDA excitation are shifted through the hybrid functional by 0.5–0.7 eV. While TDLDA was potentially underestimating, TDB3LYP might overestimate the energies—where the cautious phrasing takes into account that no directly comparable experimental data are at hand[15]. What can be compared is the value from TDB3LYP with PCM solvent model, and a good agreement with the experiment is obtained. Note that there is a considerable bathochromic shift of the lowest $\pi \rightarrow \pi^*$ transition (see legend of Tabel 3.17), which is corresponding to the large impact PCM does on the excitation energies.

---

[15]If at all then the energy in n-hexane of 3.14 eV should be compared to gas phase results.

Table 3.17: Lowest important TDDFT excitations for NDPD along with their major contributions of KS orbital transitions.

state	energy (eV)	sym	osc. str.	major contributions		
				origin	target	percent
			TDLDA			
1	2.64	B	0.735	HOMO	LUMO	86
2	2.90	A	0.071	HOMO−1	LUMO	74
3	3.15	A	0.000	HOMO−2	LUMO	94
6	3.96	A	0.000	HOMO−3	LUMO	95
9	3.97	B	0.396	HOMO−1	LUMO+1	77
10	4.05	A	0.136	HOMO	LUMO+2	61
			TDB3LYP(VWN5)			
1	3.28	B	1.004	HOMO	LUMO	91
2	3.66	A	0.157	HOMO−1	LUMO	86
3	3.73	A	0.000	HOMO−2	LUMO	90
6	4.48	A	0.000	HOMO−7	LUMO	92
7	4.74	A	0.209	HOMO	LUMO+1	86
8	4.77	B	0.412	HOMO−1	LUMO+1	84
			TDB3LYP(VWN1) in PCM acetonitrile			
1	2.86	B	1.123	HOMO	LUMO	92
2	3.26	A	0.207	HOMO−1	LUMO	88
3	3.98	A	0.000	HOMO−4	LUMO	88
6	4.56	A	0.003	HOMO−7	LUMO	88
7	4.57	A	0.246	HOMO	LUMO+1	88
10	4.63	B	0.449	HOMO−1	LUMO+1	68
			exp in MeCN [54] [b]			
	2.85		60.8 [a]			
	4.56		26.8 [a]			

osc. str. = oscillator strength; [a] max. extinction coefficient $\times 10^{-3}$ M^{-1} cm^{-1}; [b] Pucher et al. [52] found 2.84 eV and 53000 M^{-1} cm^{-1} in MeCN and 3.14 eV in n-hexane.

HOMO−7
$\epsilon = -7.37$ eV
B

HOMO−6
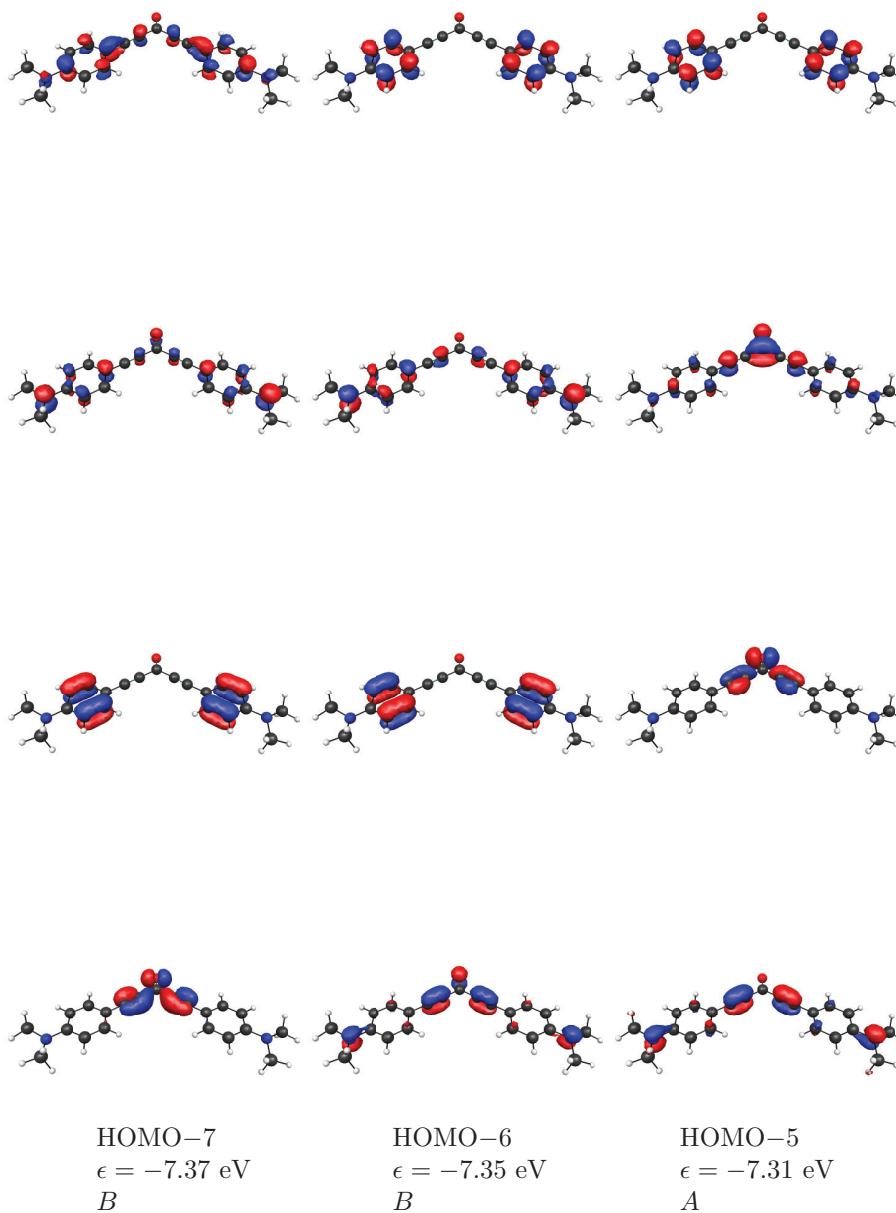$\epsilon = -7.35$ eV
B

HOMO−5
$\epsilon = -7.31$ eV
A

Figure 3.32: B3LYP/cc-pVTZ KS orbitals for NDPD from GAMESS. Underneath the orbital specification ϵ refers to the KS eigenvalue and its symmetry, the contour value for the plot was 0.05.
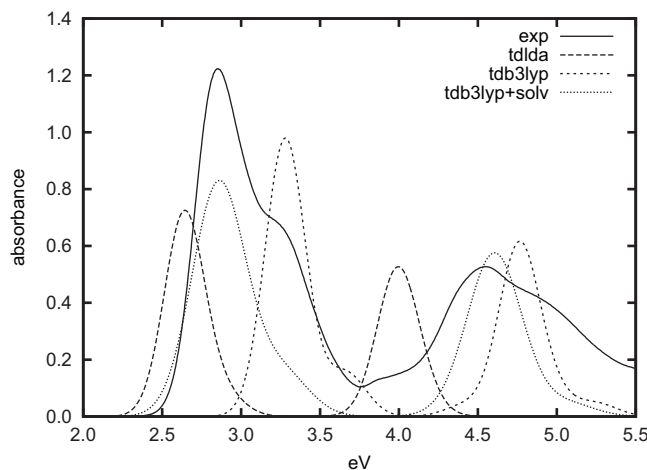
Figure 3.33: Experimental and theoretical spectra of NDPD, the latter broadened by 0.3 eV. The experimental line was measured at a concentration of 2.5×10^{-5} M in acetonitrile [51].

3.3 Conclusions

A group of aromatic ketones, which are in use or proposed as photoinitiators in photopolymerizations, were studied by means of electronic structure theories. In particular neutral electronic excitations were computed on TDDFT and GW-BSE levels of theory. In TDDFT several common functionals, refering to the LDA (PZ81 functional) and GGA (PBE functional) approximations, and a hybrid functional (B3LYP) were employed and their performance compared.

The ground state geometries were obtained as optimized minima with the highest symmetry that yielded valid results. NMR shifts for these structures were in good agreement with experimental data.

While the HF HOMO eigenvalue disagrees by 0.4 eV with the photoelectron spectrum and the DFT HOMO KS eigenvalues are by far lower, the GW quasiparticle energies agree excellently with not only the lowest but also higher PES bands.

All compounds studied here exhibit excitations that stem from a transition from the carbonyl O lone pairs n_O to antibonding π^* orbitals. These transitions are known to cause photoinitiator activity due to succeeding H abstraction from the monomer by the carbonyl O. To summarize the above tables (and add two

TDPBE values), these excitations were obtained as follows

method	BPH	DPD	ODPD	SDPD	NDPD
TDLDA	3.25	3.05	3.14	3.07	3.15
TDGGA	3.30	3.11	3.20	3.13	3.21
TDHybrid	3.76	3.64	3.71	3.67	3.73
GW-BSE	3.07	2.78	—	—	—
exp, gas	3.30	—	—	—	—

From there I conclude that TDLDA and TDGGA are yielding this type of excitation in good agreement with the experiment and *GW*-BSE and that GGA functionals do not introduce large changes on LDA. The hybrid functional shifts the excitations energies considerably and overestimates them. The cause of this much poorer performance of the hybrid compared to the LDA functional remains somewhat obscure. Apparently these excitation energies are particularly sensitive to geometry changes (compare values for HF- and B3LYP-optimized structures in the results section). *GW*-BSE seems not to improve on TDLDA with respect to the sparse experimental data. From a general point of view, all these excitations are weak (symmetry forbidden in C_{2v}) and occur at an almost constant wave length, in agreement with experimental findings. The compounds should thus have a comparable photoinitiator activity, provided that no other mechanisms are present.

The strongest absorption bands are in all cases $\pi \rightarrow \pi^*$ transitions, and the contributing KS orbital transitions hint at considerable charge transfers between phenyl/alkyne moieties and the carbonyl group. To reiterate the above and summarize

method	BPH	DPD	ODPD	SDPD	NDPD
TDLDA	4.42	3.45	3.05	2.60	2.64
TDHybrid	4.94	3.96	3.65	3.32	3.28
TDHyb+PCM	4.79	3.79	3.34	3.04	2.86
GW-BSE	4.39	3.59	—	—	—
exp, solv	4.96	3.85	3.50	3.31	2.85

Hybrid functionals again shift the TDLDA (and TDGGA) excitation energies by an almost constant quantity. In contrast to the $n_O \rightarrow \pi^*$ transitions above the present underestimation of TDLDA (and TDGGA) is thereby corrected to better agreement with experiment. This is a rather general observation [23] and may also be explained by the large dipole moment changes found with CASSCF. They suggest a considerable charge transfer character of these excitations which is not well described by TDLDA. Admixture of non-local exchange cures this shortcoming to some extent. The relatively crude solvent model PCM introduces changes in agreement with experiments and mostly improves over the vacuum results. *GW*-BSE improves somewhat on TDLDA, but still deviates from experiments. The method should in general cover charge transfer type excitations. But the changes introduced by B3LYP are in large parts removed in the *GW*-BSE approximation (as in the former case). In general, the red shift of excitations introduced in DPD derivatives by the auxochromic groups is in good agreement with experiments and empirical rules.

It is hoped by the author that the various excitation properties of the compounds studied could be successfully clarified by computational methods. The

theoretical observations may lead to deeper understanding of experiments and more sophisticated applications.

Concerning the computational cost of the calculations TDDFT is clearly much less expensive than GW-BSE, as the following table shows[16]

	TDLDA (G)	TDB3LYP (G)	TDLDA (P)	GW_f-BSE
BPH C_2	29.7 h (2)	53.3 h (2)	1.8 h (12)	121.2 h (12)
DPD C_{2v}	19.2 h (2)	27.5 h (2)	10.0 h (6)	927.6 h (16)

It is seen that a higher symmetry reduces the computational cost drastically. The longer CPU times for DPD with Parsec/RGWBS stem from the much larger number of states that was used (800, instead of 400 for BPH). B3LYP needs significantly more CPU time than LDA. The real space computations for TDLDA are potentially less ressource intensive than with Gaussian bases, depending on the number of states which are used for the linear response. GW-BSE is in general an expensive method, again depending on the number of states. This refers not only to CPU time, but also to memory use (2 Gb per process in the DPD example, increasing with decreasing number of nodes). The GW_f parts without solving the BSE for the above examples are 54.8 h (12) for BPH and 297.7 h (16) for DPD. Note that the real space codes are partitioning well into several processes. The limited number of nodes in the above examples stems from hardware limits rather than methodical feasibility. One can draw the conclusion from the above that real space techniques are in general a handy realization of quantum chemical methods. GW and GW-BSE are both methods that involve considerable computational cost and are difficult to apply as the method is rather complicated and elaborated codes with a long history of development and community feedback lack.

Suggestions for Further Work

Although expensive, GW and GW-BSE are both promising methods that are expected to gain broader popularity amongst computational chemists. In this spirit more work should be done on examples for which more reference data are available, in particular carefully obtained gas phase spectra. GW proofed to be an accurate method to calculate photoelectron spectra, but also here more experience should be acquired.

An interesting idea would be to compare the obtained results with excitation spectra computed by Fourier transformation of real time TDDFT calculations. This could also be done for two-photon processes.

---

[16]Wall clock time in hours on AMD Opteron 180s, the number of processes is specified in parentheses. (G)AMESS was compiled with gfortran linked to the ACML library; (P)arsec: gfortran and ACML library; RGWBS: gfortran and Lapack/Blas routines. Processor communication took place via a Gigabit-Switch on the basis of MPICH2.

Bibliography

[1] T. Helgaker, P. Jørgensen and J. Olsen, *Molecular Electronic-Structure Theory*, John Wiley & Sons, 2000

[2] F. Jensen, *Introduction to Computational Chemistry*, John Wiley & Sons, 1999

[3] C. J. Cramer, *Essentials of Computational Chemistry*, John Wiley & Sons, 2002

[4] R. Parr and W. Yang, *Density Functional Theory of Atoms and Molecules*, Oxford University Press, 1989

[5] C. Fiolhais, F. Nogeira and M. Marques (eds.), *A Primer in Density Functional Theory*, Springer, 2003

[6] W. Koch and M. C. Holthausen, *A Chemist's Guide to Density Functional Theory*, Wiley-VCH, 2000

[7] K. Burke *et al.*, *The ABC of DFT*, a raw version of the book is available online at `http://dft.uci.edu/`

[8] A. Szabo and N. S. Ostlund, *Modern Quantum Chemistry, Introduction to Advanced Electronic Structure Theory*, Dover, 1996 (reprint of McGraw–Hill, 1989)

[9] P. Hohenberg and W. Kohn, *Phys. Rev.* **136**, B 864 (1964)

[10] W. Kohn and L. J. Sham, *Phys. Rev.* **140**, A 1133 (1965)

[11] J. C. Slater, *Phys. Rev.* **81**, 385 (1951)

[12] J. P. Perdew and A. Zunger, *Phys. Rev. B* **23**, 5048 (1981)

[13] S. H. Vosko, L. Wilk and M. Nusair, *Can. J. Phys.* **58**, 1200 (1980)

[14] A. D. Becke, *Phys. Rev. A* **38**, 3098 (1988)

[15] J. P. Perdew and Y. Wang, *hys. Rev. B* **45**, 13244 (1992)

[16] C. Lee, W. Yang and R. G. Parr, *Phys. Rev. B* **37**, 785 (1988)

[17] J. P. Perdew, K. Burke and M. Ernzerhof, *Phys. Rev. Lett.* **77**, 3875 (1996)

[18] J. P. Perdew, L. A. Constantin, E. Sagvolden and K. Burke, *Phys. Re. Lett.* **97**, 223002 (2006)

[19] M. E. Casida, Time-Dependent Density Functional Response Theory for Molecules, in D. P. Chong (ed.), *Recent Advances in Density Functional Theory, Part I*, World Scientific, Singapore, 1995, p. 155

[20] R. Bauernschmitt and R. Ahlrichs, *Chem. Phys. Lett.* **256**, 454 (1996)

[21] I. Vasiliev, S. Öğüt, J. R. Chelikowsky, *Phys. Rev. B* **65**, 115416 (2002)

[22] M. A. L. Marques, C. U. Ullrich, F. Nogueira, A. Rubio, K. Burke and E. K. U. Gross (eds.), *Time-Dependent Density Functional Theory*, Lect. Notes Phys. 706, Springer, 2006

[23] P. Elliott, K. Burke and F. Furche, `arXiv:cond-mat/0703590`

[24] G. Onida, L. Reining and A. Rubio, *Rev. Mod. Phys.* **74**, 601 (2002)

[25] R. D. Mattuck, *A Guide to Feynman Diagrams in the Many-Body Problem*, Dover, 1992 (reprint of 2nd ed., McGraw–Hill, 1976)

[26] J. Linderberg and Y. Öhrn, *Propagators in Quantum Chemistry*, John Wiley & Sons, 2004

[27] E. Runge and E. K. U. Gross, *Phys. Rev. Lett.* **52**, 997 (1984)

[28] F. W. Byron Jr. and R. W. Fuller, *Mathematics of Classical and Quantum Physics*, Dover, 1992 (reprint of Addison–Wesley, 1969, 1970)

[29] L. Hedin, *Phys. Rev.* **139**, A 796 (1965)

[30] M. L. Tiago and J. R. Chelikowksy, *Phys. Rev. B* **73**, 205334 (2006)

[31] D. C. Harris and M. D. Bertolucci, *Symmetry and Spectroscopy*, Dover, 1989 (reprint of Oxford University Press, 1978)

[32] GAMESS version 11 April 2008 (R1):
M. W. Schmidt, K. K. Baldridge, J. A. Boatz, S. T. Elbert, M. S. Gordon, J. H. Jensen, S. Koseki, N. Matsunaga, K. A. Nguyen, S. J. Su, T. L. Windus, M. Dupuis and J. A. Montgomery, *J. Comput. Chem.* **14**, 1347 (1993)

[33] MacMolPlt graphics: B. M. Bode and M. S. Gordon, *J. Mol. Graphics Mod.* **16**, 133 (1998)

[34] K. M. Gough and T. A. Wildman, *J. Am. Chem. Soc.* **112**, 9141 (1990)

[35] S. Urahata and S. Canuto, *Int. J. Quantum Chem.* **80**, 1062 (2000)

[36] E. B. Fleischer, N. Sung and S. Hawkinson, *J. Phys. Chem.* **72**, 4311 (1968)

[37] V. Volovsek, G. Baranovic and L. Colombo, *Spectrochim. Acta* **49A**, 2071 (1993)

[38] Spectral Database of Organic Compounds SDBS, published electronically at `http://riodb01.ibase.aist.go.jp/sdbs/`, National Institute of Advanced Industrial Science and Technology (AIST), Japan, January 2009.

[39] Gaussian 03, Revision C.02
M. J. Frisch, G. W. Trucks, H. B. Schlegel, G. E. Scuseria, M. A. Robb, J. R. Cheeseman, J. A. Montgomery Jr., T. Vreven, K. N. Kudin, J. C. Burant, J. M. Millam, S. S. Iyengar, J. Tomasi, V. Barone, B. Mennucci, M. Cossi, G. Scalmani, N. Rega, G. A. Petersson, H. Nakatsuji, M. Hada, M. Ehara, K. Toyota, R. Fukuda, J. Hasegawa, M. Ishida, T. Nakajima, Y. Honda, O. Kitao, H. Nakai, M. Klene, X. Li, J. E. Knox, H. P. Hratchian, J. B. Cross, C. Adamo, J. Jaramillo, R. Gomperts, R. E. Stratmann, O. Yazyev, A. J. Austin, R. Cammi, C. Pomelli, J. W. Ochterski, P. Y. Ayala, K. Morokuma, G. A. Voth, P. Salvador, J. J. Dannenberg, V. G. Zakrzewski, S. Dapprich, A. D. Daniels, M. C. Strain, O. Farkas, D. K. Malick, A. D. Rabuck, K. Raghavachari, J. B. Foresman, J. V. Ortiz, Q. Cui, A. G. Baboul, S. Clifford, J. Cioslowski, B. B. Stefanov, G. Liu, A. Liashenko, P. Piskorz, I. Komaromi, R. L. Martin, D. J. Fox, T. Keith, M. A. Al-Laham, C. Y. Peng, A. Nanayakkara, M. Challacombe, P. M. W. Gill, B. Johnson, W. Chen, M. W. Wong, C. Gonzalez and J. A. Pople, Gaussian Inc., Wallingford CT, 2004

[40] L. Klasinc, I. Novak, A. Sabljić and S. P. McGlynn, *Int. J. Quantum Chem.* **S15**, 259 (1988)

[41] K. W. Holtzclaw and D. W. Pratt, *J. Chem. Phys.* **84**, 4713 (1986)

[42] W. L. Dilling, *J. Org. Chem.* **31**, 1045 (1966)

[43] R. Liska and B. Seidl, *J. Polym. Sci. A: Polym. Chem.* **43**, 101 (2005)

[44] C. Reichardt, *Solvents and Solvent Effects in Organic Chemistry*, 3rd ed., Wiley-VCH, 2003

[45] R. Stowasser and R. Hoffmann, *J. Am. Chem. Soc.* **121**, 3414 (1999)

[46] E. J. Baerends and O. v. Gritsenko, *J. Phys. Chem. A* **101**, 5383 (1997)

[47] J. R. Chelikowsky, N. Troullier and Y. Saad, *Phys. Rev. Lett.* **72**, 1240 (1994)

[48] J. R. Chelikowsky, *J. Phys. D* **33**, R33 (2000)

[49] Pseudopotential generation code ver. 5.695 (2004) of J. L. Martins, available from http://bohr.inesc-mn.pt/~jlm

[50] N. Troullier and J. L. Martins, *Phys. Rev. B* **43**, 1993 (1991)

[51] Experimental spectra were provided by N. Pucher and R. Liska, Institute of Applied Synthetic Chemistry, Vienna University of Technology.

[52] N. Pucher, A. Rosspeintner, V. Satzinger, V. Schmidt, G. Gescheidt, J. Stampfl and R. Liska, *Macromolecules* **42**, 6519 (2009)

[53] G. Herzberg, *Molecular Spectra and Molecular Stucture III – Electronic Spectra and Electronic Stucture of Polyatomic Molecules*, Krieger, 1991 (corr. reprint of 2nd ed., Van Nostrand, 1966)

[54] C. Heller, N. Pucher, B. Seidl, K. Kalinyaprak-Icten, G. Ullrich, L. Kuna, V. Satzinger, V. Schmidt, H. Lichtenegger, J. Stampfl and R. Liska, *J. Polym. Sci. A: Polym. Chem.* **45**, 3280 (2007)